HAW HAMBURG

Master Thesis

Software Testing: VSPAERO

Author: Floris Mariën

Supervisor: Prof. Dr.-Ing. Dieter Scholz, MSME
Submitted: 2021-07-16

Faculty of Engineering and Computer Science
Department of Automotive and Aeronautical Engineering

This work is part of:
Digital Library - Projects & Theses - Prof. Dr. Scholz
http://library.ProfScholz.de

This report is deposited and archived:
- Deutsche Nationalbiliothek (https://www.dnb.de)
- Repository of Leibniz University Hannover (https://www.repo.uni-hannover.de)
- Internet Archive (https://archive.org)
  Item: https://archive.org/details/TextMarien.pdf

This report has associated published data in Harvard Dataverse:
https://doi.org/10.7910/DVN/0S1R14

Abstract

Purpose – Test the aerodynamic analysis code VSPAERO, which is part of OpenVSP from NASA. Apply VSPAERO to calculate the lift curve slope and the span efficiency factor of straight wings (for various aspect and taper ratios) as well as the induced drag of box wings (for various h/b-ratios) relative to their reference wing.

Methodology – VSPAERO results are compared with results from analytical equations, wind tunnel measurements, and results produced with other aerodynamic codes.

Findings – VSPAERO offers correct and reliable results, if the simulation is set up with care. The user must always keep an eye on model discretization and refinement, flow conditions, and number of iterations. The Vortex Lattice Method (VLM) and the panel method are best used for different purposes. The VLM shows shorter simulation time and produces reliable results. The panel method is more complicated to use. Numerical results are also good. In addition, the panel method can be used better to visualize flow phenomena. Hoerner's simple approach to induced drag estimation can be used to approximate results of the VLM and the panel method, if a simple correction factor is applied.

Research Limitations – Most of the tests of VSPAERO have been done with a simple wing geometry, as such much simpler than a full aircraft geometry.

Practical Implications – VSPAERO can be used with relative ease. It can also be used to show flow phenomena on full aircraft geometry.

Originality – Repeating simple calculations done many times before does not sound original, but doing this with the relatively new software VSPAERO offering the VLM as well as the panel method seems to be original after all.

DEPARTMENT OF AUTOMOTIVE AND AERONAUTICAL ENGINEERING

Software Testing: VSPAERO

Task for a *Master* Thesis

Background

Conceptual aircraft design provides around 50 core parameters of the aircraft. OpenVSP (http://openvsp.org) can be used to get a 3D representation of the geometry. OpenVSP-Connect (http://openVSP.Profscholz.de) can help considerably to set up an OpenVSP model. Subsequently, it is desirable to get an impression of the flow over this aircraft geometry or even to get some aerodynamic parameters like the lift curve slope. VSPAERO is the aerodynamic tool, which comes with OpenVSP. VSPAERO provides quick aerodynamic analysis options using the Vortex Lattice Method (VLM) or the Panel Method. It integrates actuator disks that can be used for aero-propulsive analysis. VSPAERO also comes with a viewer to display wakes and pressure coefficient changes. The idea of this thesis is simply to get familiar with VSPAERO, to comment on its handling, and to determine whether the software provides reliable and correct simulation results. A start from the vary basics will be necessary to get familiar and to produce useful results.

Task

Task is simply the evaluation of OpenVSP's VSPAERO software by a sequence of experiments. The detailed tasks are:

- Literature review of the VLM and Panel Method.
- Description of OpenVSP and its aerodynamic code VSPAERO.
- Discretization studies to determine the sweet spot between correct and reliable results and a short simulation time.
- Literature review of analytical equations for the lift curve slope of a wing.
- Comparison of the lift curve slope of a wing calculated with VSPAERO (VLM and Panel Method) with the analytical equations.
- Literature review of analytical equations for the Oswald factor (span efficiency factor) of a wing.
- Comparison of the Oswald factor (span efficiency factor) calculated with VSPAERO for a straight wing, described by its aspect ratio, A and taper ratio λ with Hoerner's approach (https://n2t.net/ark:/13960/t57f0bk2j, page 7-4).
- Literature review of equations for the estimation of the induced drag of box wings (related to the reference wing).

- Comparison of the induced drag of box wings calculated with VSPAERO (as a function of the h/b-ratio) with equations from literature as well as previously obtained simulation results and wind tunnel measurements.
- Literature review related to the numerical visualization of the flow and the pressure distribution.
- Comparison of flow visualization options with the VLM and Panel Method of VSPAERO.

The report has to be written in English based on German or international standards on report writing.

Table of Contents

List of Figures

List of Tables

List of Symbols

A	Aspect Ratio
AoA	Angle of Attack
b	Wing span length
c	Chordlength of an airfoil
$Calc\ CG$	Calculate center of gravity in VSPAERO
C_{D0}	Zero lift drag coefficient
C_{Di}	Induced drag coefficient
C_L	Lift coefficient
C_{L0}	Zero angle of attack lift coefficient
$C_{L\alpha}$	Lif curve slope
c_r	Root chord of a wing
c_t	Tip chord of a wing
D	Total drag force acting on a body
D_i	Total induced drag force acting on a body
e	Oswald efficiency factor
e_{theo}	Theoretical Oswald efficiency factor
F	Force
$f(\lambda)$	Function of taper ratio, also used as a symbol for Hoerner's Curve
h	Vertical distance between horizontal wings of a box wing
h/b	Vertical distance between horizontal wings of a box wing over the span of the box wing
i_w	Incidence angle of a wing
k	Induced drag factor
$k_{e,D0}$	Oswald efficiency correction factor due to viscous drag
$k_{e,F}$	Oswald efficiency correction factor due to fuselage effects
$k_{e,M}$	Oswald efficiency correction factor due to compressibility effects
L	Total lift force acting on a body
l	Length of the panel in the flow direction in VLM
L/D	Glide ratio
M	Mach number
n	Vector perpendicular on a surface
p	Pressure
PD	Percentage deviation
p_d	Dynamic pressure
p_s	Static pressure
p_t	Total pressure
r	Radius
R	Universal gas constant
Re	Reynolds number

S	Surface
T	Temperature
t/c	Thickness-to-chord ratio of an airfoil
V_∞	Free stream velocity
w_b	Normal velocity component induced by the wing's bound vortices
w_i	Normal velocity component induced by the wake

Greek Symbols

α	Angle of attack
α_{ZL}	Angle of attack for zero lift
β	Reciprocal of the Mach number correction factor
γ	Ratio of specific heats at constant pressure and at constant volume
Γ_n	Strength of a horseshoe vortex (circulation)
ε_t	Wing twist angle
κ	The ratio oft he two-dimensional lift-curve slope (per radian) at the appropriate Mach number to $2\pi/\beta$.
λ	Taper ratio of a wing
λ_{opt}	Optimal taper ratio of a wing according to Hoerner
v	Kinematic viscosity of a streaming fluid
v_w	Dihedral angle of a wing
ξ	Vorticity of a streaming
π	Mathematical constant pi
ρ	(Air) Density
φ	Sweep angle of a wing
ϕ	Velocity potential
ϕ_{TE}	Angle of the trailing edge of an airfoil

List of Abbreviations

AFRL	Air Force Research Laboratory
AVL	Athena Vortex Lattice, which is a program to simulate the aerodynamic and flight dynamic analysis of arbitraty configuration, created by Mark Drela from MIT (Budziak 2015) (Drela 2013).
CFD	Computational Fluid Dynamics
FEA	Finite Element Analysis
ISA	International Standard Atmosphere
LE	Leading Edge of an airfoil
NACA	National Advisory Committee for Aeronautics
NASA	National Aeronautics and Space Administration
OML	Outer Mold Line
OpenVSP	Open Vehicle Sketchpad
SSL	Standard Sea Level
TE	Trailing Edge of an airfoil
VLM	Vortex Lattice Method

1   Introduction

1.1   Motivation

In present high tech days, engineers have access to a wide variety of programs which could be used to define aircraft geometry. These software, has to be sufficient to the task and the user's knowledge. A choice has to be made between advanced programs, which are based on expanded equations and will consequently be more time-consuming, or simple ones, which are adequate for a limited number of cases or use rough numbers to get commonly accepted approximate values.

Even though advanced programs provide results of better quality (more precise and detail), those are more difficult to learn and use. Therefore, it can be beneficial to start analysing a case with a less complex program, which still provides reasonable results. This thesis will evaluate one of these less complex programs, namely OpenVSP VSPAERO.

1.2   Title Terminology

"Software Testing: VSPAERO"

Software
The Cambridge Dictionary defines the word *software* as:

> *The instrucrions that control what a computer does; computer programs.*

This thesis aims to determine if the presented software does what is has to. Namely, provide the user with reasonable and reliable simulation results.

Testing
The word *testing* is defined by the Cambridge Dictionary as:

> *The process of using or trying something to see if it works, is suitable, obeys the rules, etc.*

The software is tested and compared to other software and experiments to examinate it's usability, results, reliability etc.

VSPAERO
This is the software used to do the aerodynamic analysis. By doing so, the software is tested how well the results reproduce the theory, experiment results or expectations.

1.3   Objectives

This thesis aims to learn how to operate the OpenVSP VSPAERO program, describe it's user's experience and decide if the program is reliable enough to use in aerodynamic analysis.

In the beginning, the number of elements in the model will be optimized to guarantee satisfying results.

Afterwards the lift curve slope is obtained and compared to theoretical calculations. This is done for three cases: a rectangular wing, a swept wing and a swept, tapered wing.

Later on, the Oswald efficiency factor obtained by VSPAERO and theoretical calculations are compared for different wing geometries and aspect ratio's. To compare these results, the Hoerner Curve $f(\lambda)$ is created for both points of view.

A next step is to take a look at box wing configurations. Again, the Oswald efficiency factor is obtained by VSPAERO for a range of h/b ratio. These results are converted into a factor k and will be compared with results from theoretical calculations and wind tunnel experiments done before.

As a last experiment, the pressure distribution on a full aircraft model will be examined for simulations done with VLM and also with the Panel Method. This is done by using the Viewer in the Results Manager.

Furthermore, a User Guide will be written with some tips and tricks as a help for readers who want to start modelling simple configurations.

1.4   Previous Research

This thesis is not based on previous research. All experiments are, to our knowledge, not done before with VSPAERO. From searching the World Wide Web, two works have been found, both from Linköping University.

The first work is called *Simulation Model Development of a Subscale Fighter Demonstrator: Aerodynamic Database Generation and Propulsion Modeling* by Carry Prameswari (Prameswari 2017). This work concludes that VSPAERO VLM produces more optimistic results compared to the same simulation done with Panel Method. Also, this works states that doing simulations with the Panel Method generally takes more time than doing the same simulation withVLM.

The other work is called *Aircraft Modeling Though BeX & OpenVSP* by Marius Fuentes Galan (Fuentes Galan 2018). This work focused more on aircraft design through OpenVSP than simulating with VSPAERO. It states that OpenVSP is a very complete program regarding aircraft design.

There was no study found where research was done how VSPAERO does simulations, and if those results are correct. This thesis will try to provide this.

1.5   Structure of the Work

This work consists of 8 main chapters. The structure of the thesis is as follows:

Chapter 2   An overview of OpenVSP and it's possibilities is given in this chapter.

Chapter 3   This chapter explains the theoretical background of which theories VSPAERO uses to do the simulations.

Chapter 4   The refinement study to get to reliable results is clarified in this chapter.

Chapter 5   The first experiment is discussed. The theoretical lift curve slope of consecutively a rectangular, swept and swept, tapered wing will be compared with the results given by VSPAERO.

Chapter 6   In this chapter, theoretical background on the Oswald efficiency factor will be given. The results from VSPAERO will be converted in a $f(\lambda)$-curve. This cuve is compared with Hoerner's curve. This is done for seven cases. Each case has a constant aspect ratio, with changing taper ratio form zero to one.

Chapter 7   This chapter gives theoretical background on box wing configurations, shows and discusses the results gained by VSPAERO. Throughout the Oswald efficiency factor, a new curve k is made and compared to the ones obtained by simulations with other softwares or wind tunnel experiments done before.

Chapter 8   This chapter examinates the pressure distribution and flow visualization options given by VSPAERO.

Chapter 9   Provides the reader a User Guide to start modelling simple configurations in OpenVSP and how to do aerodynamic analysis with VSPAERO.

Data related to this thesis (VSPAERO files and files from post processing with Excel) can be found at "Harvard Dataverse" (https://dataverse.harvard.edu) in the "Digital Library - Projects & Theses - Prof. Dr. Scholz" (https://dataverse.harvard.edu/dataverse/LibraryProfScholz). The DOI is given at the bottom of page 2.

2 OpenVSP and VSPAERO

2.1 OpenVSP

OpenVSP is the abbreviaton of Open Vehicle Sketchpad. It's an open source parametric aircraft geometry, developed originally by NASA. OpenVSP gives the user the possibility to create three-dimensional models of aircraft and to do engineering and aerodynamic analysis on those models (OpenVSP). The logo of OpenVSP is visible in Figure 2.1.

OpenVSP is the successor of VSP and Rapid Aircraft Modeler (RAM), developed by J.R. Gloudemans and others for NASA in the beginning of 1990s. On January 10, 2012, OpenVSP was released as an open source project under the NASA Open Source Agreement (NOSA) version 1.3 (OpenVSP). Later development is lead by Rob McDonald since around 2012 and is supported by NASA and AFRL among others (Wikipedia 2021b).

As said, OpenVSP quickly allows the user to generate models from ideas, which later can be analyzed. Therefore, OpenVSP is very suited to generate and evaluate conceptual aircraft (Wikipedia 2021b).
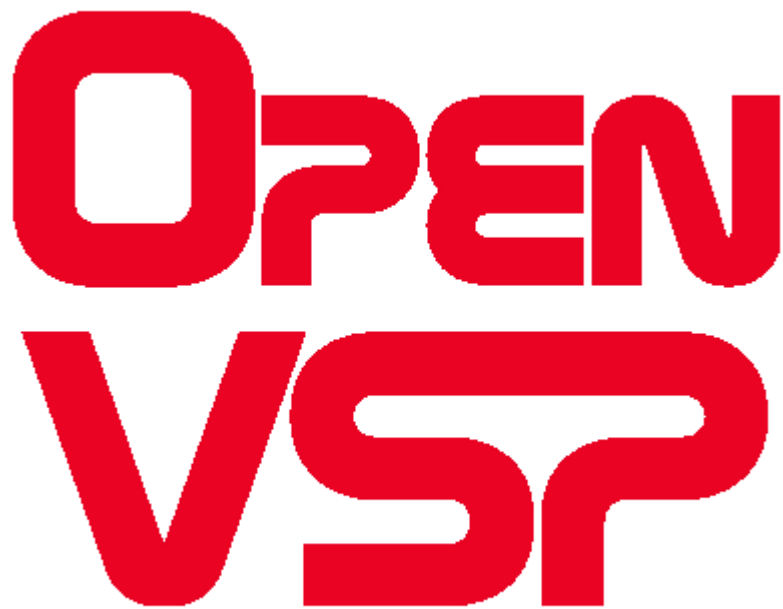
Figure 2.1   OpenVSP Logo (OpenVSP 2014).

2.2 Features of OpenVSP

2.2.1 Graphical User Interface

After launching, OpenVSP shows a workspace window and a 'Geometry Browser'. The Geometry Browser lists all individual components (fuselage, wing,…) of the user's model, while the workspace is where the model is displayed. When a component is selected, a component geometry window opens. This window is used to modify the parameters of the selected component (Wikipedia 2021b). This setup is shown in Figure 2.2.
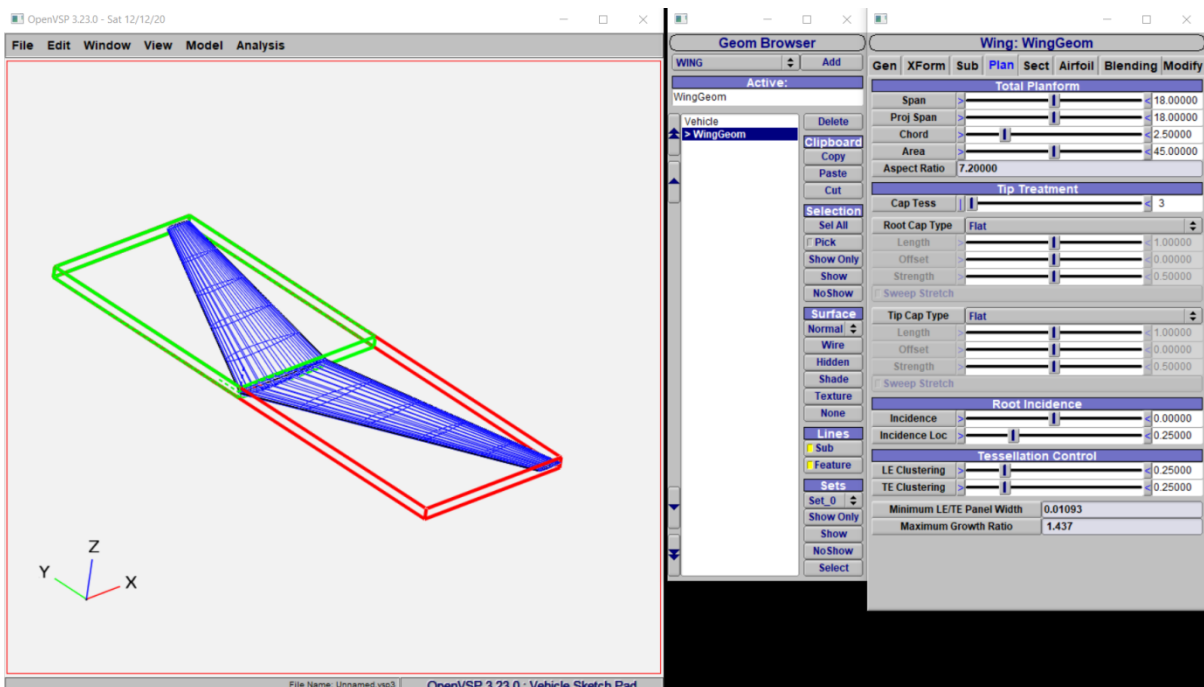
Figure 2.2   OpenVSP setup: Left window = Workspace, Middle window = Geometry browser, Right window = Geometry window.

2.2.2 Geometry Modelling

OpenVSP provides multiple, common to aircraft modelling, geometries which can by modified and asambled to an aircraft model, e.g. wing, pod, fuselage, propeller, … Furthermore, more advanced components like body of revolution, duct,… are available (Wikipedia 2021b).

2.2.3   Analysis Tools

As mentioned before, OpenVSP provides multiple tools to do structural or aerodynamic analysis. A summary of the possible tools with a short explanation is given below.

- CompGeom – Mesh generating tool that can handle model intersection and trimming. Therefore calculation of wetted area, as a basis to estimate zero-lift drag (Scholz 2021b).
- Mass Properties Analysis – Computes properties like centre of gravity and moment of inertia.
- Projected Area Analysis – To compute projected area.
- CFD Mesh – To generate meshes that may be used in CFD analysis.
- FEA Mesh – To generate meshes that may be used in FEA analysis.
- DegenGeom – To generate various simplified representations of geometry models like point, beam and camber surface models.
- VSPAERO – For vortex lattice or panel method based aerodynamic and flight dynamic analysis.
- Wave Drag Analysis – For estimating wave drag geometries.
- Parasite Drag Analysis – For estimating parasite drag of geometries based on parameters like wetted area and skin friction coefficient.
- Surface fitting – For fitting a parametric surface to a point cloud.
- Texture Manager – For applying image textures to geometry for aiding visualization. (Wikipedia 2021b)

2.3   Compatibility with Other Software

OpenVSP allows the user to import geometry files from other formats listed below.
- Cart3D (.tri),
- Stereolith (.stl),
- NASCART (.dat),
- Xsec as Tri mesh or Wireframe (.hrm),
- Point Cloud (.pts),
- OpenVSP v2 (.vsp),
- Blade Element (.bem),
- Plot3D as Wireframe (.p3d).

The other way around, the user can export his file to other formats too. The different options are summed up below.
- XSec (.hrm),

- PLOT3D (.p3d),
- Stereolith (.stl),
- NASCART (.dat),
- Cart3D (.tri),
- VSPGeom (.vspgeom),
- Gmsh (.msh),
- POVRAY (.pov),
- X3D (.x3d),
- Untimmed STEP (.stp),
- Untrimmed STEP Struct (.stp),
- Untrimmed IGES (.igs),
- Untrimmed IGES Struct (.igs),
- Blade Element (.bem),
- AutoCAD (.dxf),
- SVG (.svg),
- Xpatch (.facet),
- PMARC 12 (.pmin),
- OBJ (.obj),
- Airfoil Points (.dat),
- Airfoil Curves (.bz),
- Custom Script (.vsppart).
  (Wikipedia 2021b)

2.4   Hangar

OpenVSP provides a virtual hangar, where users can upload and download models. In fact, it promotes sharing of geometries made in OpenVSP. Each model allows revision with extra details on source quality and gets a quality score (Wikipedia 2021b). This score is a quick and objective way to measure the level of the overall quality of the model and the used information to create this. When uploading, the user is asked to rate their model based on the descriptions listed below.

1. Defenitive – The model is the definition of the vehicle or part.
2. Essentially Exact – Detailed dimensions and drawings were used to create the model.
3. Good Representation – Good three-view drawings were used to create the model.
4. Inaccurate – Photos and drawings were used to create the model but few dimensions were available.
5. Completely Inaccurate – The creator thougt of the vehicle or part as he or she made it, but did not use pictures, drawings, or dimensions.
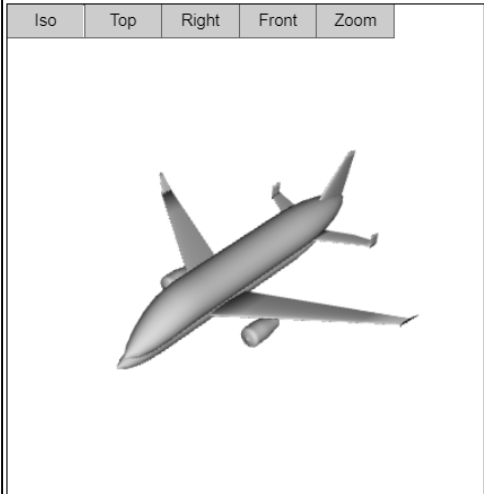
Other than that, a model gets a suitability score too. This indicates how suitable a model is for a given purpose, so the user can quickly find a model best suited for their needs. Again, the creator gets five options to rate his or her model in case of suitability considering following purposes (1 is excellent, 5 is poor):

- Cartoon or to look pretty,
- Buld a display model,
- Check internal layout/volume,
- OML for wetted areas/drag buildup,
- Accurate OML for detailed aerodynamic analysis or CFD,
- Weight and balance,
- Structural analysis.
  (OpenVSP 2021)

An example of a model available at OpenVSP Hangar is shown in Figure 2.3.

Figure 2.3   Example of a model available at OpenVSP Hangar. The model is the definition of the Airbus Beluga XL (Ram 2020). Note the model suitability score too.

2.5 OpenVSP Ground School

This tutorial program is designed to guide users of all experience levels of the OpenVSP tool. The program provides video demonstrations of multiple concepts and features of OpenVSP and is intended to serve as a library of material for users to reference. Example files are also provided so the user can follow along using the same models as in the demonstrations (Litherland 2021a).

This program is still in development, more and more detailed material is expected in the future. The following list shows what is or will be available at OpenVSP Ground School.

- Chapter 1: OpenVSP Fundamentals;
- Chapter 2: Modeling and Designing Intent;
- Chapter 3: Model Analysis in OpenVSP;
- Chapter 4: Working with Other Programs;
- Chapter 5: Advanced OpenVSP Techniques.
  (Litherland 2021a)

2.6 OpenVSP Google Group

Another way to find help with possible difficulties while using OpenVSP can be the Google discussion group. It's an online place where users can ask questions, report problems, meke requests, or just discuss OpenVSP. The group can be found at https://groups.google.com/g/openvsp.

From personal experience, this is found very helpful. Not only the development team, but also other users help one another to solve problems or answer questions.

2.7 VSPAERO

VSPAERO is released in 2015, developed to as a part of OpenVSP. It's a thin-surface code for inviscid subsonic and supersonic aerodynamics, It is multithreaded to make the most of common, multi-core computers and uses a mesh agglomeration scheme to improve scaling with large meshes. The matrix is solved with an iterative GMRES solver. VSPAERO includes a simple actuator disk model to represent propulsion-airframe interaction and also the ability to calculate common stability derivatives (OpenVSP 2015).

3 Theoretical Background

This chapter covers the theoretical background which OpenVSP VSPAERO uses to do aerodynamic analysis. In VSPAERO, the user has two options to do so, the first is the Vortex Lattice Method (VLM) and the second one is a Panel Method.

Computational aerodynamics has the ability to provide insight in complex problems by solving the governing equarions of fluid dynamics. Looking at Figure 3.1, the typical functions flowchart in a computational aerodynamics system consists of three parts: Geometry setup, Flow solver, and Post-processing. This figure lists four solver options, from most simplified (Linear Potential) to the most complete (Navier-Stokes Equations) flow model. Which flow model to choose is determined by the practical research problem (Liu 2007).

Considering inviscid, incompressible flow, the potential flow provides sufficient results over a wide range of conditions. The Laplace Equation is essentially an exect representation of this flow.
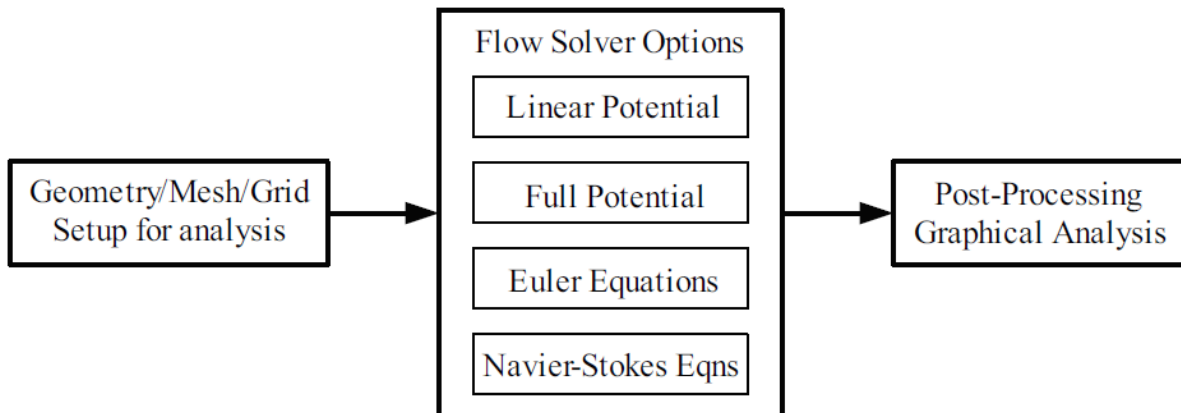
Figure 3.1   Representation of the typical functions flowchart in a Computational Aerodynamics system (Liu 2007).

3.1 Aerodynamic Fundamentals

3.1.1 Potential Flow

Starting with irrotational flow, which is defined as a flow where the vorticity is zero at every point.

$$\xi = \nabla \times V = 0 \tag{3.1}$$

If ϕ is a scalar function, following the vector identity, we get

$$\nabla \times (\nabla \phi) = 0 \quad . \tag{3.2}$$

Which means that the curl of the gradient of a scalar function is equal to zero. combining (3.1) and (3.2), gives

$$V = \nabla \phi \quad . \tag{3.3}$$

Equation (3.3) states that for irrotational flow, there exists a scalar function ϕ such that the velocity is given by the gradient of ϕ. From now on, ϕ is denoted as the velocity potential.

From the principle of mass conservation for an incompressible flow, Equation (3.4) is obtained.

$$\nabla \cdot V = 0 \tag{3.4}$$

With the definition of velocity potential ϕ, for a flow that is both incompressible and irrotational, (3.3) and (3.4) can be combined to

$$\nabla \cdot (\nabla \phi) = 0 \quad , \tag{3.5}$$

or

$$\nabla^2 \phi = 0 \quad .$$

Equation (3.5) is the well known Prandtl-Glauert Equation (similar to Laplace's Equation), which governs irrotational, incompressible flow. Because the Laplace's Equation is linear, (Anderson 2011) states that:

> *A complicated flow pattern for an irrotational, incompressible flow can be synthesized by adding together a number of elementary flows which are also irrotational and incompressible.*

These different elementary flows include point/line source, point/line sink, point/line doublet and point/line vortex. The VLM is based on these line vortices (Liu 2007).

3.1.2 Boundary Conditions

VLM linearizes and transfers the boundary condition (shown in Figure 3.2) and makes a linear approximaton between velocity and pressure by using the so-called "thin airfoil boundary condition". After the linear approximation on the lower and upper surfaces of the airfoil, (Mason 2015) states:

For cases where the linearized pressure coefficients relation is valid, thickness does not contribute to lift to first order in the velocity disturbance!

This means that the cambered surface boundary conditions can be applied on a flat coordinate surface and result in a much more easy way to apply the boundary conditions (Liu 2007).
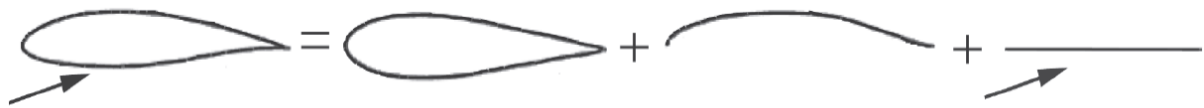
Considering a symmetrical airfoil/wing, the camber effect can also be neglected, after applying this boundary condition to Laplace's Equation, the problem can easily be solved by including the effect of angle of attack on a flat surface. This is what VLM uses (Liu 2007).

Consider a wing, placed on the x-y plane. The boundary condition states that normal flow across the thin wing's solid surface is zero (Liu 2007).

$$\nabla(\phi + \phi_\infty) = 0 \tag{3.6}$$

Which means that the sum of the normal velocity component induced by the wing's bound vortices wb, by the wake wi and by the free-stream velocity V_∞ will be zero (Liu 2007).

$$w_b + w_i + V_\infty \cdot \alpha = 0 \tag{3.7}$$

General airfoil at α Thickness at $\alpha = 0$ Camber at $\alpha = 0$ Flat plate at α

Figure 3.2   Decomposition of a general airfoil at a certain incidence (Mason 2015).

3.1.3 Biot-Savart Law

As stated, the point vortex singularity is one of the possible solutions for Laplace's Equation. The vortex flow is shown in Figure 3.3. This vortex induces a tangential velocity defined by

$$V_\theta = \frac{\Gamma}{2 \cdot \pi \cdot r} \ . \tag{3.8}$$

Where Γ is the vortex circulation strength. Note that this is constant around the circle of radius to the flow center r. The circulation has the same sign as it's vorticity, so it's positive in the clockwise direction (Liu 2007).

The idea of a point vortex can be extended to a general three-dimensional vortex filament. The flowfield induced by this vortex filament can be seen in Figure 3.4.

The mathematical description of the flow induced by this filament is given by the Biot-Savart law. It states that the increment of the velocity dV at a point P due to a segment of a vortex filament dl at a point q is (Liu 2007).

$$dV_P = \frac{\Gamma}{4\pi} \cdot \frac{dl \times r_{Pq}}{|r_{Pq}|^3}$$ (3.9)

This can then be integrated over the entire length of the vortex filament to obtain the induced velocity in point P (Liu 2007).

$$V_P = \frac{\Gamma}{4\pi} \int \frac{dl \cdot r_{Pq}}{|r_{Pq}|^3}$$ (3.10)

a) streamlines   b) velocity distribution
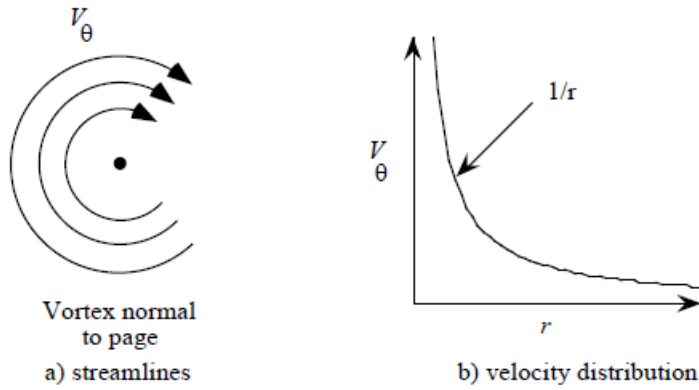
Figure 3.3   Representation of the point vortex (Mason 2015).
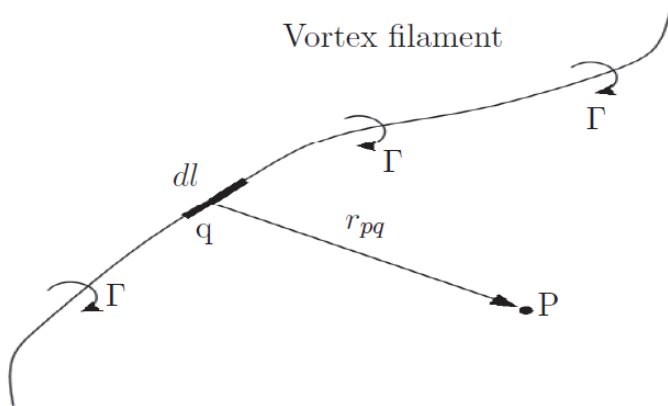
Figure 3.4   Three-dimensional vortex filament (Liu 2007).

3.1.4 Horseshoe Vortex

In VLM, a special form of vortex is used. This is the horeshoe vortex, shown in Figure 3.5, where the vortex line is assumed to be placed in the x-y plane, making the horseshoe vortex a simplified case of the vortex ring. It consist of four vortex filaments. Two trailing segments *ab* and *cd* of the vortex are placed parallel to the direction of the free-stream velocity and start at infinity. The other two segments *bc* and *ad* are finite. Normally, the effect of ad can be neglected because of the infinite distance. So, in practice, the horseshoe vortex only contains three parts. The straight bound vortex segment *bc* models the lifting properties and the two semi-infinite trailing vortex lines model the wake. In general, the expression of the induced velocity at a point by one horseshoe vortex is (Liu 2007)

$$V = V_{bc} + V_{b\infty} + V_{c\infty} \quad . \tag{3.8}$$
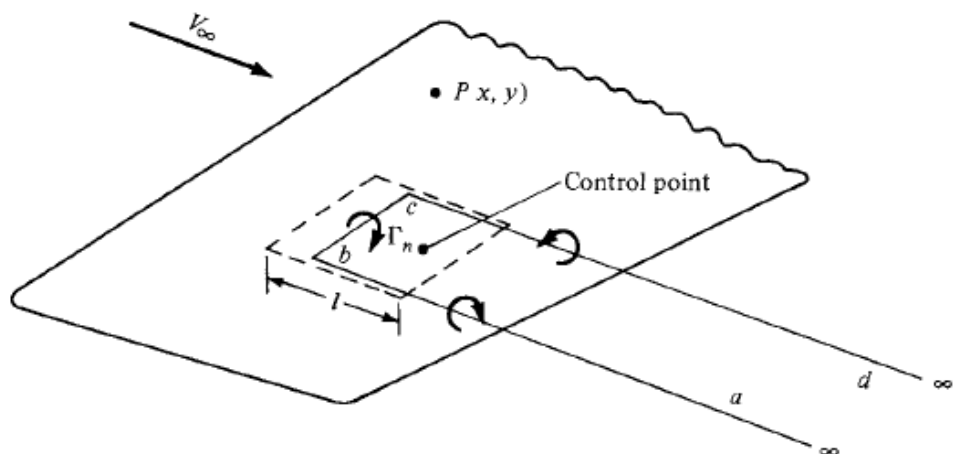
Figure 3.5 Schematic of one single horseshoe vortex, which is part of a vortex system on a wing (Anderson 2011).

For the finite length vortex segment *bc* in the horseshoe vortex, the induced velocity at a certain point can be calculated using (3.13), where r_1 and r_2 are the distances from this certain point to the two end points of the segment and r_0 is the length of the segment (Liu 2007).

$$V_P = \frac{\Gamma}{4\pi} \cdot \frac{|r_1 \times r_2|}{|r_1 \times r_2|^2} \cdot \left[r_0 \cdot \left(\frac{r_1}{|r_1|} - \frac{r_2}{|r_2|} \right) \right] \tag{3.12}$$

As mentioned, the horseshoe vortex is going to represent a lifting surface. Important here, is the location of the vortex and where the location of a control point has to be, to satisfy the surface boundary condition. The answer to this problem is called the "¼ − ¾ rule". The vortex is located at the ¼ chord point, and the control point is located at the ¾ chord point. The rule was discovered by Pistolesi, has proven to be sufficiently accurate in practice, and has

become a rule of thumb (Mason 2015). Mathemetical derivations of more precise vortex/control point locations are available in (Lan 1974).

Note that the lift is on the bound vortices. This is because of the Kutta – Joukowsky theorem (eq. 3.13) (Mason 2015), which states that a vortex of certain circulation Γ moving with free-stream velocity Q_∞ creates lift L (Budziak 2015).

$$\boldsymbol{L} = \rho \cdot \boldsymbol{V}_\infty \cdot \Gamma \tag{3.9}$$

As said, the surface of the model is divided into a finite number of panels (chordwise and spanwise). On each of these panels there is a horseshoe vortex, as shown in Figure 3.6. Each vortex has his own circulation and thus, to get the total aerodynamic force, the contribution of all panels have to be summarized (Anderson 2011).
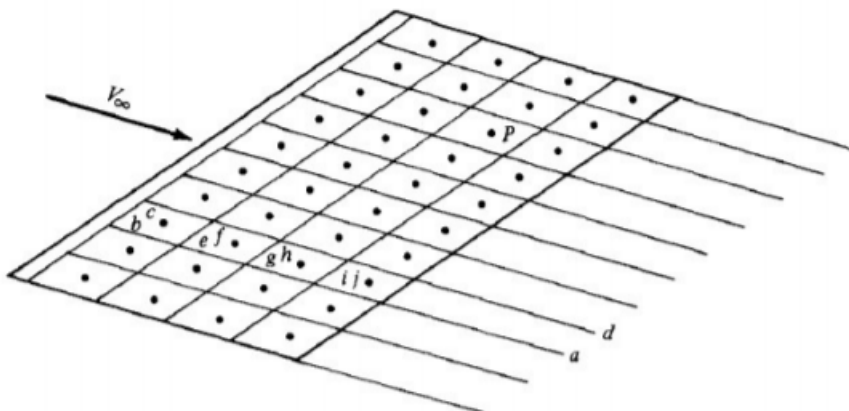
Figure 3.6   Vortex Lattice System on a finite wing (Anderson 2011).

3.2   Vortex Lattice Method

VLM, first called "Vortex Lattice" in 1943 by Faulkner, is extremely simple, but because of a purely numerical approach, practical solutions had to wait for sufficient computer power (Liu 2007). Where Prandtl's classic lifting-line theory only gives satisfying results for straight wings at moderate to high aspect ratio, VLM has the ability to also treat low-aspect-ratio straight wings, swept wings, and delta wings, shown in Figure 3.7 (Anderson 2011). The Vortex Lattice Method, is a numerical method, used in aerodynamic analysis, mainly in the early stages of aircraft design. The VLM models the lifting surfaces as a infinitely thin sheet of discrete vortices to compete lift L, induced drag D_i, lift curve slope, and lift distribution. Note that the influence of the thickness of the model and the viscosity of the fluid is neglected, so the VLM cannot compute viscous drag. In case of the VLM, the force distribution can be extracted to compute the aerodynamic coefficients and their derivatives important for aircraft's conceptual design (Wikipedia 2021c).

As the VLM represents the wing (or complete model) as a surface (or set of surfaces) on which a grid of horseshoe vortices are superimposed. The velocities induced by each hoseshoe vortex at a specified control point are calculated using the law of Biot-Savart. A summation is performed for all control points on the wing, to produce a set of linear algebraic equations for the strength of each horseshoe vortex that satisfies the boundary condition of no flow through the wing (or model). The vortex strengths Γ_n are related to the wing circulation and the pressure differential between the upper and lower wing surfaces. The pressure differentials are integrated to yield the total foces and moments (Bertin 2009).
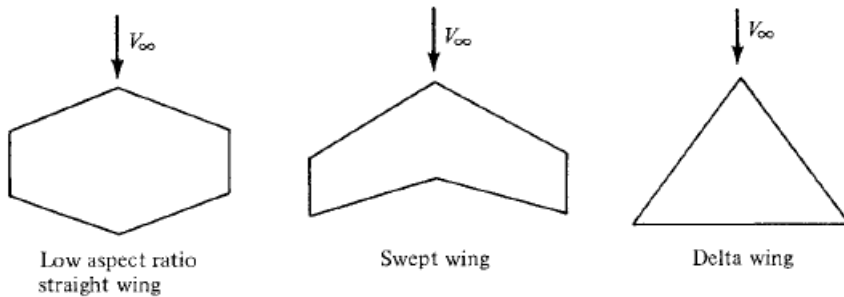
Figure 3.7   Types of wing planforms for which the classical lifing-line theory is not sufficient (Anderson 2011).

3.3   Panel Method

The panel method is a numerical scheme for solving linear, inviscid, irrotational flow (Prandtl-Glauert Equation) around aircraft, flying at subsonic or supersonic speeds. Fundamental analytic solutions to this equation are known as source, doublet, and vorticity singularities. Just as VLM, panel methods are based on the principle of superimposing surface distributions of these solutions over small quadrilateral portions (panels) of the aircraft surface (Erickson 1990).

Panel methods were originally developed as lower-order methods for incompressible and subsonic flows. The first successful panel method became available in the mid 1960s. Later, panel methods for three-dimensional subsonic flow was developed. This allowed the actual vehicle surface to be paneled, whereas previous methods where more restricted in the placement of the panels (Erickson 1990).

Aircraft models can be aerodynamically analyzed by panel-method-based computer programs. Note that these programs ignore much fluid physics, using the Prandltl-Glauert Equation, (3.5). This is the simplest form of the fluid-flow equations that contain compressibility effects, obtained from the general Navier-Stokes Equations by neglecting all the viscous and heat transfer terms; assuming that the flow is irrotational and thereby admitting the introduction of a velocity potential; and discarding all non linear terms. Phisically, these

assumptions mean that behaviour like separation, skinfriction drag, transonic shocks won't be predicted when using panel methods (Erickson 1990).

It is possible to compare VLM with panel methods, because they are both subject to the same basic theoretical restrictions, due to Laplace's Equation. Both methods can be seen as similar because:

- In both methods, singularities are placed on the surface;
- They bot use a number of control points to satisfy the non-penetration condition;
- A system of linear algebraic equations is solved to determine singularity strengths in both cases.

Despite these similarities, there are differences between the methods too. They differ from each other because:

- VLM is oriented towards lifting effects, and ignores thickness, explained in 0;
- In VLM, boundary conditions are applied on a mean surface, not on the actual surface. Panel methods do this on the actual surface;
- Singularities are not distributed over the entire surface, while using VLM;
- VLM is oriented toward combinations of thin lifting surfaces, where panel methods have no limitations on thickness.

(Liu 2007).

The flexibility and relative economy of the panel methods is very important in practice. This is why the methods will continue to be widely used, despite the availability of more exact models (Liu 2007).

4　Refinement and Clustering Study

To find the sweet spot between good and reliable results and a short computational time, a refinement study is done. OpenVSP allows the user to vary the number of panels in a spanwise and chordwise direction. First, there was a look taken at refinement in the chordwise direction and afterwards in spanwise direction. It's expected that for more panels, the simulation examinated results will asymptotically go to a final value.

Another tool to change refinement is clustering. Clustering regulates the dimensions of consecutive slices. Clustering is explained more and made visual in Section 4.4.

4.1　Background

For starters, the basic wing geometry parameters are defined in Table 4.1.

Table 4.1　　　　Overview of basic wing parameters (Scholz 2017).[1]

Parameter	Symbol	Definition	Unit
Span	b	Distance from tip to tip	[m]
Chord	c	Length between leading and trailing edge of the airfoil	[m]
Area	S	Wing area, multiplication of span and chord. Thus, the wing area does not just include de visible part of the wing. It also includes the area in the fuselage.	[m²]
Aspect Ratio	A	Ratio between the square of the span and area (Equation (5.7))	[/]
Taper ratio	λ	Ratio between tip cord and root chord (Equation (4.1))	[/]
Incidence angle	i_w	Angle between the chord line of the wing rood and a reference line on the fuselage (e.g. cabin floor).	[°]
Sweep angle	φ	Angle a wing makes backward, or occasionally forward, from its root rather than straight sideways.	[°]
Dihedral angle	v_w	Angle a wing makes with the horizontal plane	[°]
Wing twist	ε_t	*Geometric twist*: change in angle between the chord lines *Aerodynamic twist*: change in zero lift line along the span of an airfoil.	[°]

---

[1]　　Further comprehensive information can be found in "Jane's All The World's Aircraft" (Lambert 1992).

The taper ratio of a wing is defined by the ratio between the tip chord an the root chord. The graphical representation of the incidence angle, dihedral angle and wing twist are represented by Figure 4.1, Figure 4.2 and Figure 4.3 respectively.

$$\lambda = \frac{c_t}{c_r} \tag{4.1}$$
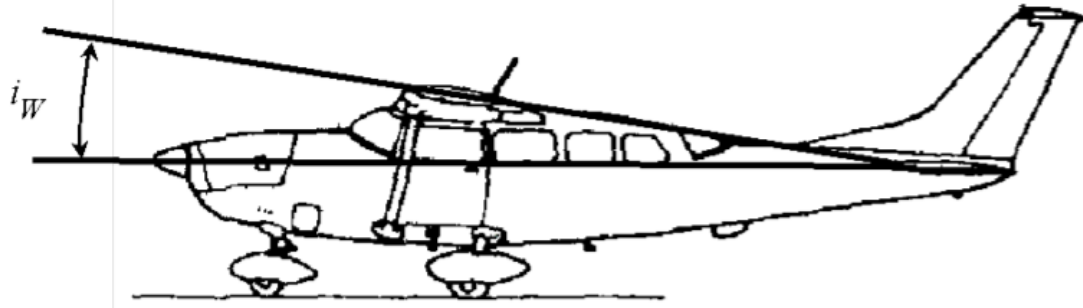
Figure 4.1 (Positive) Incidence angle i_w (Scholz 2017).
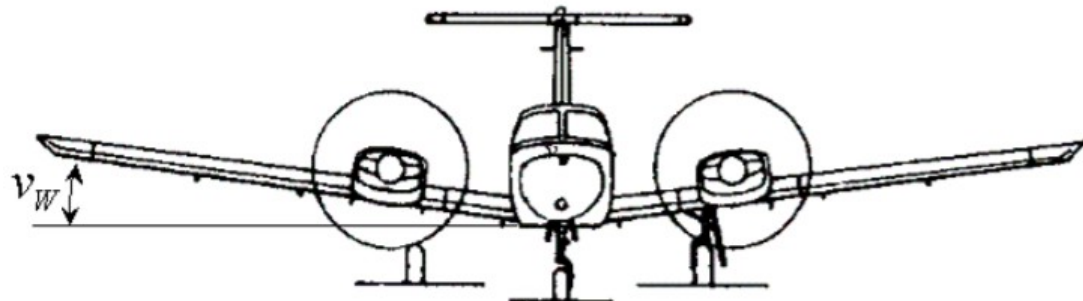
Figure 4.2 (Positive) dihedral angle of the wing v_w (Scholz 2017).
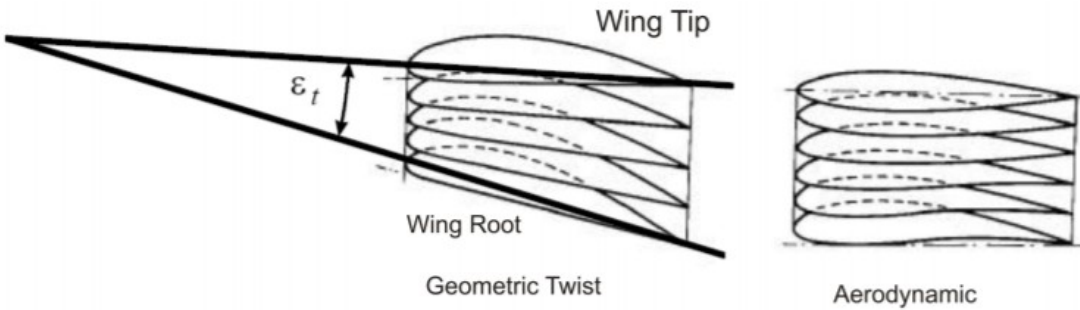
Figure 4.3 Both types of twist ε_t. The twist shown is negative (Scholz 2017).

4.2   Simulation Set-up

The base model exist of a single, rectangular wing (Figure 4.4). As explained, during the experiment the number of panels and clustering will be adapted. The wing geometry is shown in Table 4.2.

Table 4.2   Base wing geometry used in the refinement study.

Airfoil		NACA 0010
Span	B	18.0 m
Chord	C	2.0 m
Area	S	36.0 m²
Aspect Ratio	A	9.0
Taper Ratio	Λ	1.0
Incidence angle	i_w	0.0°
Sweep angle	Φ	0.0°
Wing twist	ε_t	0.0°
Dihedral angle	v_w	0.0°

Further, the center of gravity is calculated by clicking the button and the simulation is done at *AoA* equal to 10°, at $M = 0.2$, as shown in Figure 4.5. For results, there will be looked at the lift coefficient, induced drag coefficient and the Oswald efficiency factor.
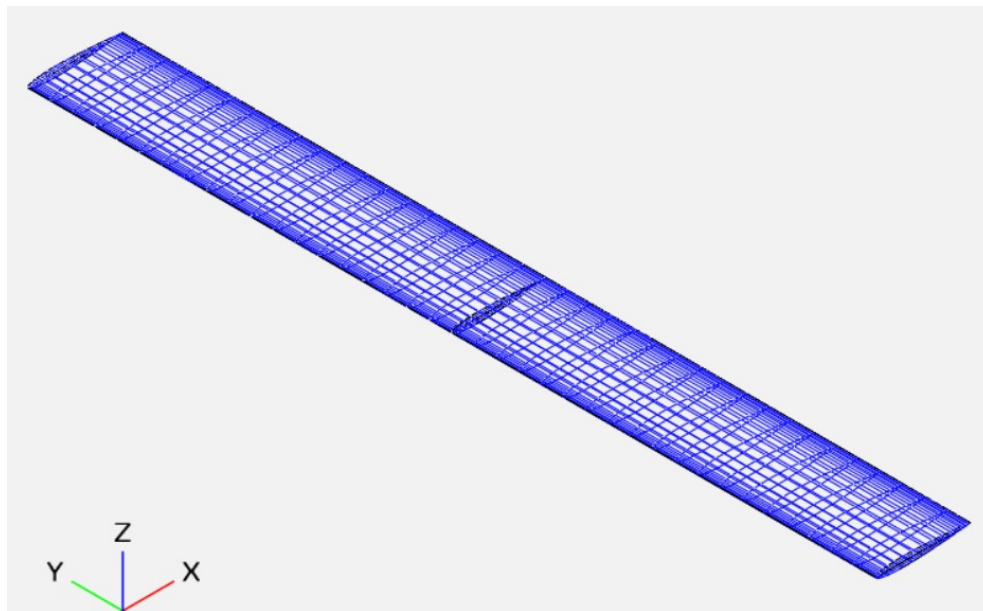
Figure 4.4   Base model used to do refinement study, viewed from the left iso view. For this case, number of panels chordwise equals 33, and spanwise, 40.
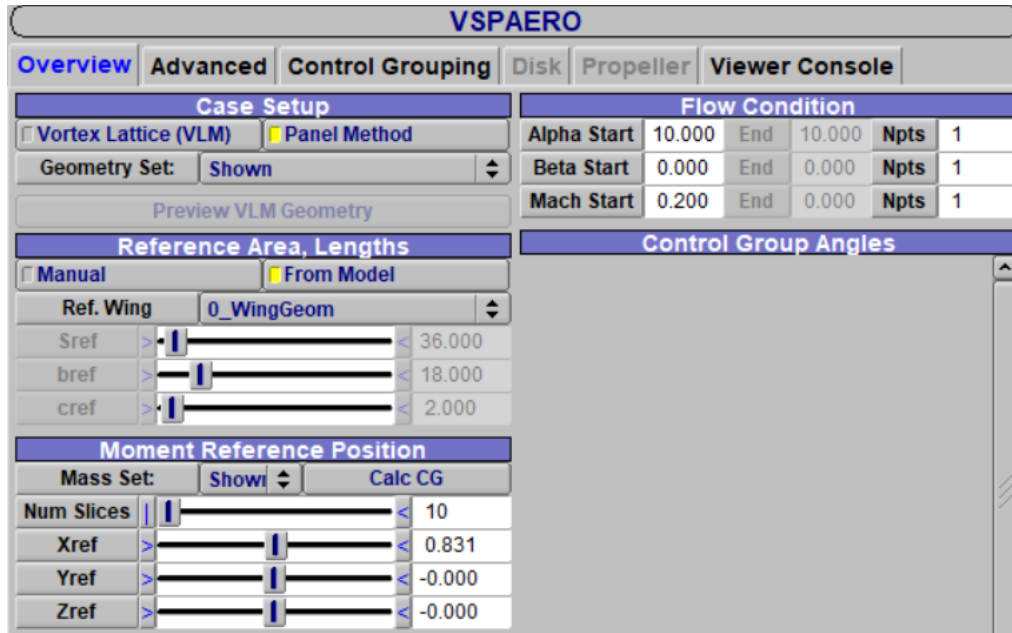
Figure 4.5   Simulation set-up for refinement study.

4.3   Refinement

4.3.1   Chordwise Refinement

Chordwise, the model can be refined by changing the *Num_W* parameter on the *Gen* tab of the *Wing Geometry* window. This is is easily made visual by Figure 4.6 and Figure 4.7. The number of spanwise slices *Num_U* is kept on the default setting equal to 6. Note that chordwise clustering is possible. This will further be discussed in Section 4.4.
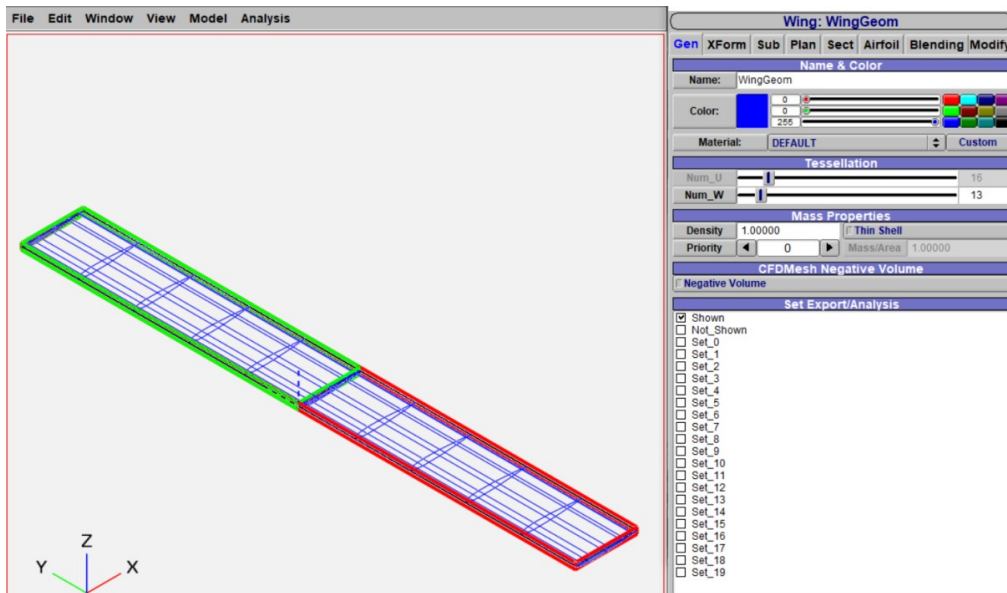
Figure 4.6   Visualization of the possible chordwise refinement. Here, Num_W is set to 13.
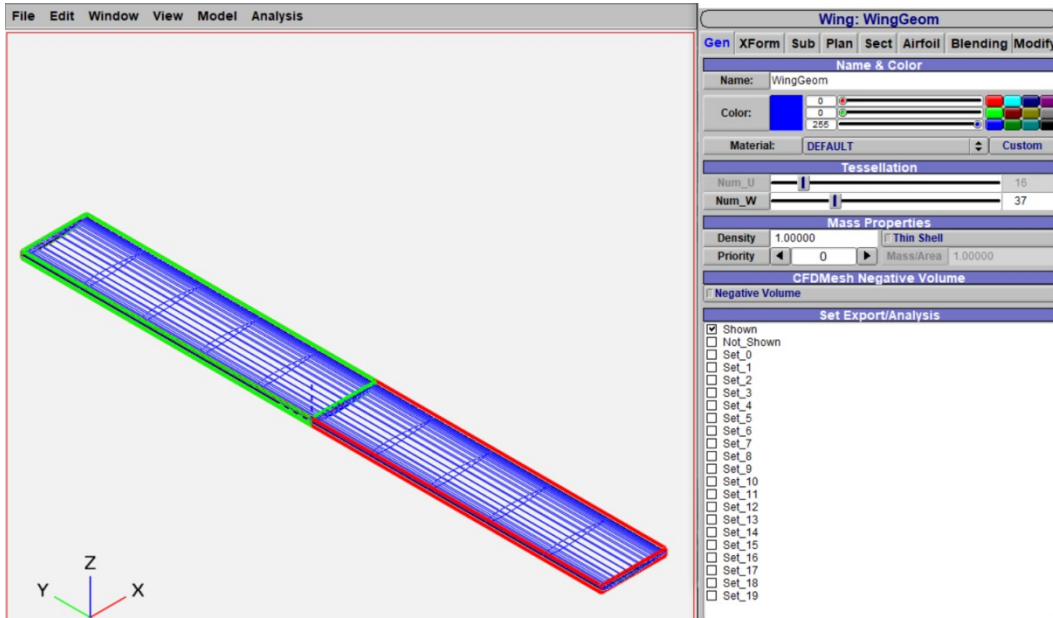
Figure 4.7   Visualization of the possible chordwise refinement. Here, Num_W is set to 37.

Table 4.3   Simulation results for chordwise refinement study.

Num_W	5	13	21	41	69	105	113	121	133
C_L	0.6520	0.7822	0.8133	0.8507	0.8595	0.8678	0.8642	0.8697	0.8686
C_{Di}	0.0257	0.0263	0.0269	0.0254	0.0265	0.0263	0.0261	0.0261	0.0257
e	0.5844	0.8224	0.8712	1.0071	0.9861	1.0128	1.0122	1.0233	1.0359

As Table 4.3 shows, from a certain number of chordwise slices, there is little change in results for C_L and e when this is further increased. On the other hand, C_{Di} is relatively constant with changing Num_U. Also, increasing or decreasing this number had a negligible influence on the solution time. The results are made visual by Figure 4.8, Figure 4.9 and Figure 4.10. It is clear to see that when looking at C_L and e, the expected asymptotical behaviour occurs. The plot for C_{Di} shows less predictable behaviour.

Also in Table 4.3, it can be concluded that mostly the values of e are not correct. For a single rectangular wing, the Oswald efficiency can never be bigger than 1.
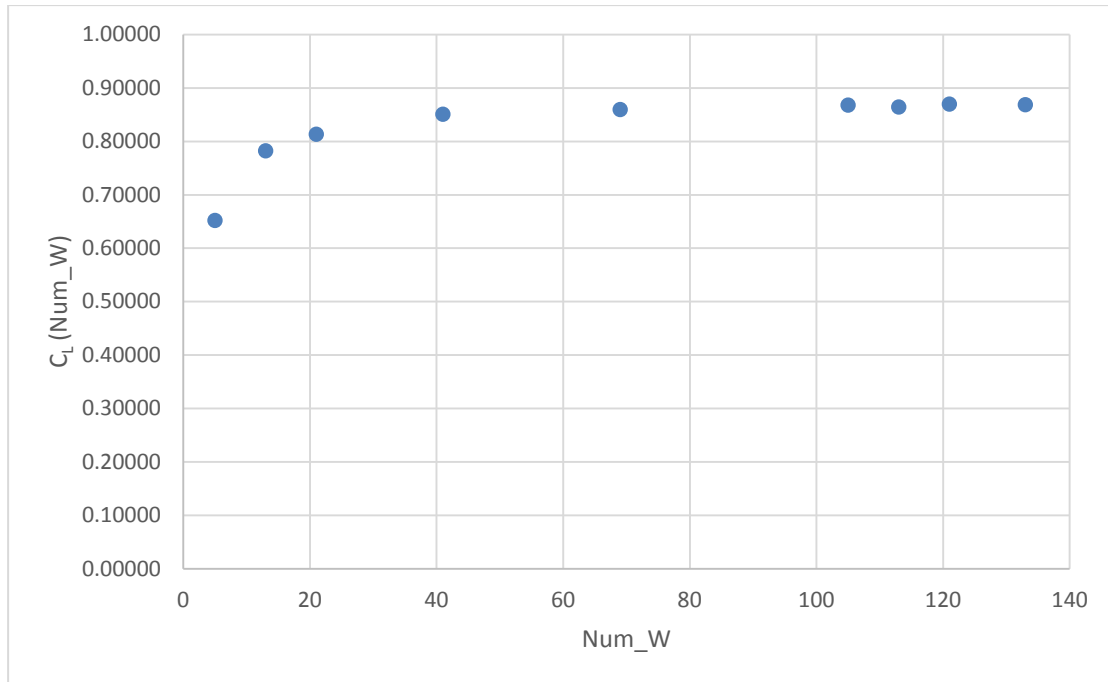
Figure 4.8   Plot showing the results looking at lift coefficient as a function of chordwise panels for refinement experiment.

Figure 4.9   Plot showing the results looking at induced drag coefficient as a function of chordwise panels for refinement experiment.

Figure 4.10   Plot showing the results looking at induced Oswald efficiency factor as a function of number of chordwise panels for refinement experiment.

It can therefore be concluded that the default number for *Num_U* (= 33) will be sufficient for the following experiments. It is very likely that for different, more complicated models, changing *Num_U* will have a bigger influence than found here.

4.3.2   Spanwise Refinement

The results of this case are shown in Table 4.4 and Figure 4.13, Figure 4.14 and Figure 4.15.

After chordwise refinement was done, spanwise refinement was investigated too. This can be done by adjusting the *Num_U* parameter in the Sect tab of the *Wing Geometry window*. This is shown in Figure 4.11 and Figure 4.12.

The big difference between chordwise and spanwise refinement is the following: Where chordwise refinement goes for the whole wing, the spanwise refinement only goes for one half of the wing. By setting *Num_U* to e.g. 20, there will be a total of 40 slices trough the wing.
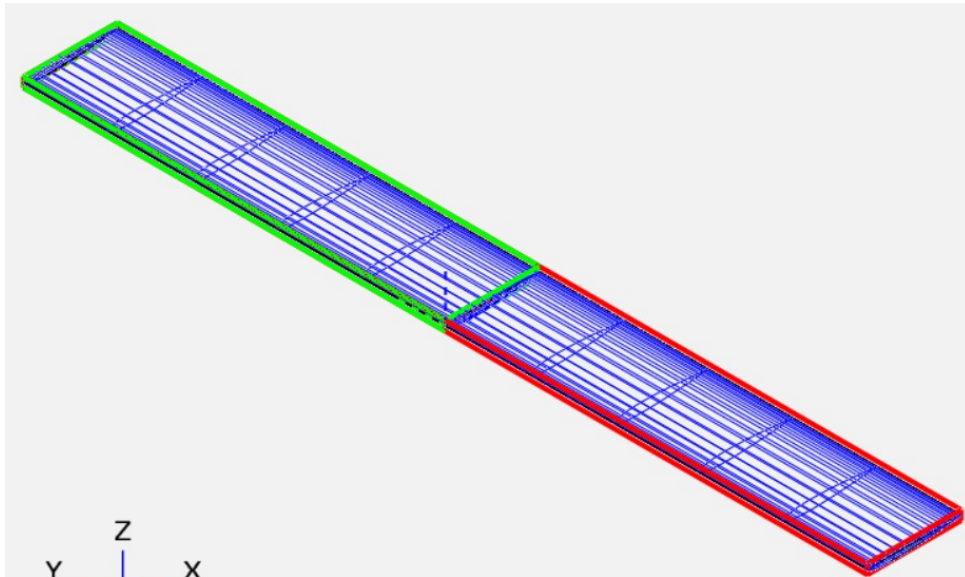
Figure 4.11   Visualization of the possible spanwise refinement. Here, Num_U is set to 6.
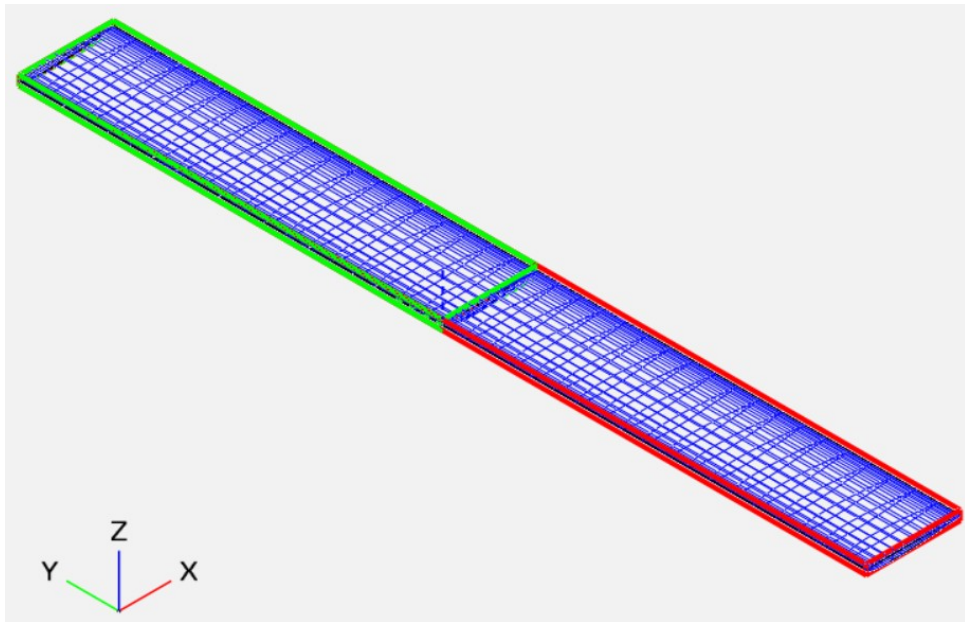
Figure 4.12   Visualization of the possible spanwise refinement. Here, Num_U is set to 20.

Table 4.4   Simulation results for spanwise refinement study.

Num_U	2	4	8	12	16	20	24	28	32	40	48	60	72	84	96
C_L	1.05	0.83	0.81	0.80	0.8	0.80	0.79	0.79	0.79	0.79	0.79	0.79	0.793	0.794	0.794
C_{Di}	0.00	0.03	0.03	0.03	0.03	0.03	0.03	0.03	0.03	0.03	0.028	0.028	0.028	0.028	0.028
e	/	0.91	0.85	0.83	0.82	0.81	0.81	0.81	0.8	0.80	0.80	0.797	0.795	0.793	0.792
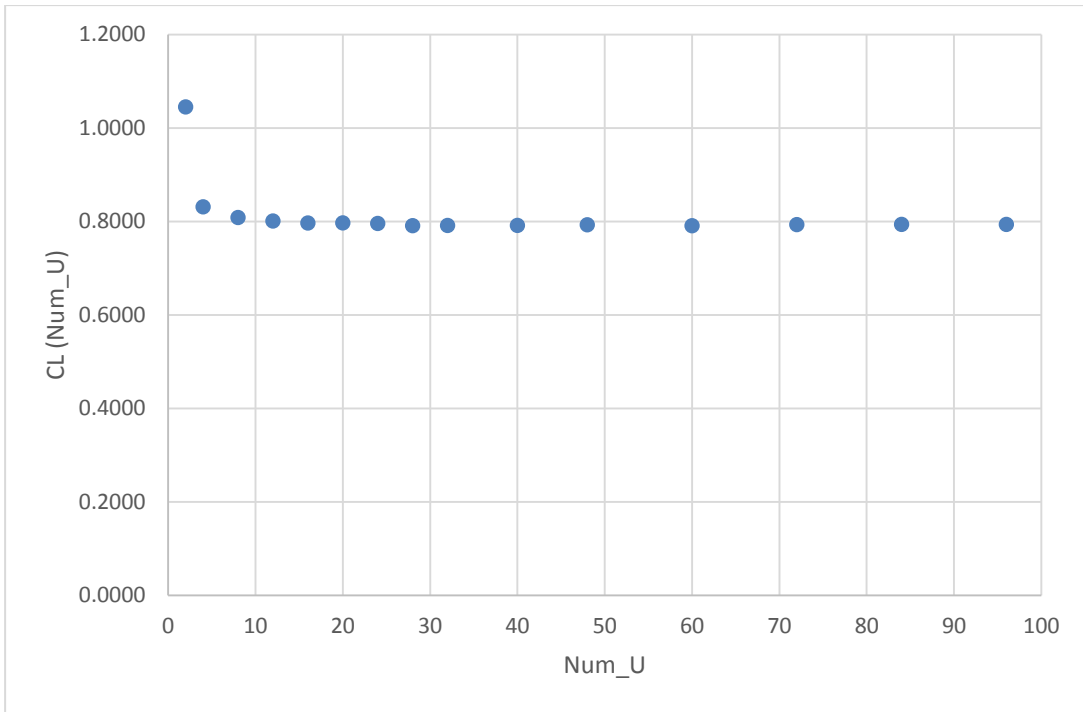
Figure 4.13   Plot showing the results looking at lift coefficient as a function of number of spanwise panels for refinement experiment.
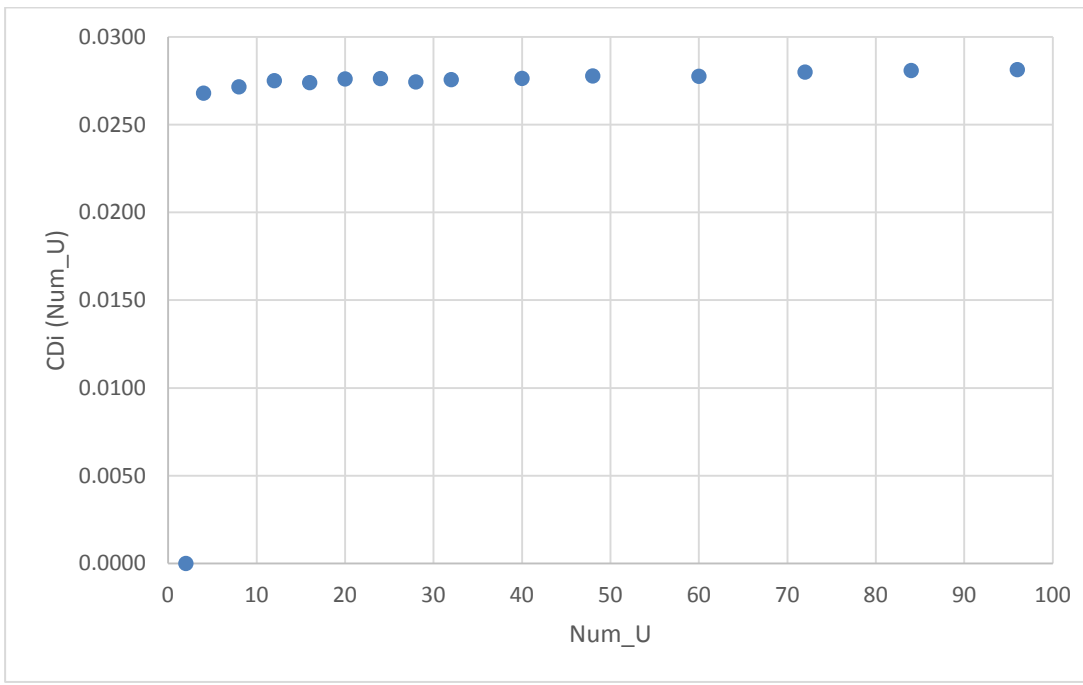
Figure 4.14   Plot showing the results looking at induced drag coefficient as a function of number of spanwise panels for refinement experiment.
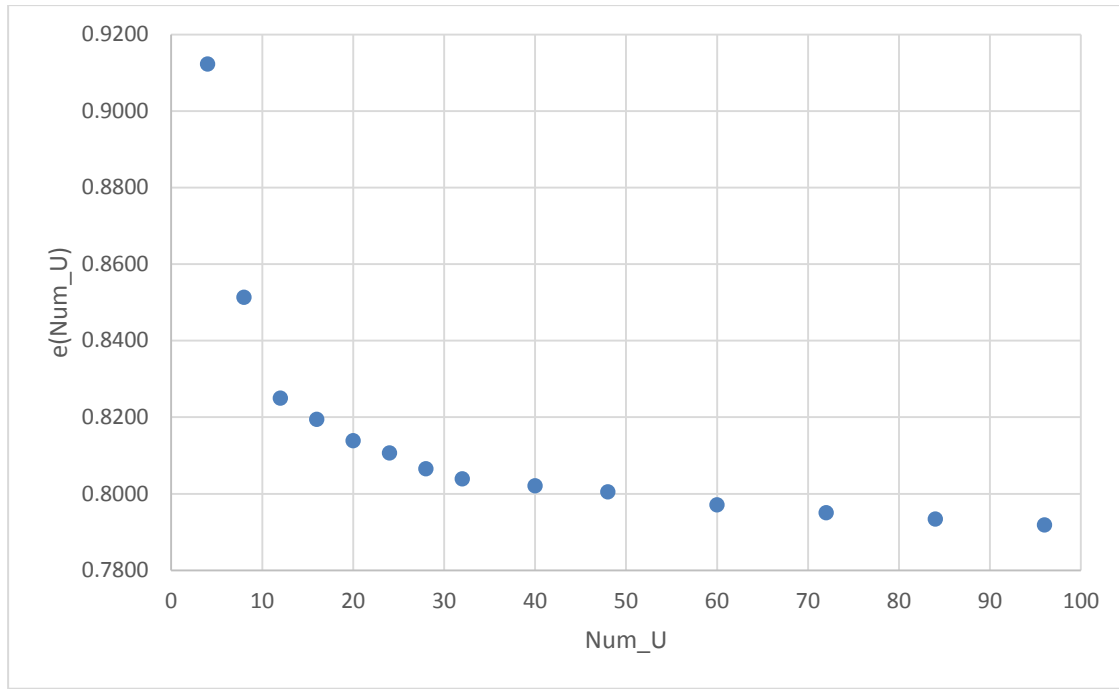
Figure 4.15   Plot showing the results looking at induced Oswald efficiency factor as a function of number of spanwise panels for refinement experiment.

Doing spanwise refinement, the expected asymptotic behaviour is strongly visible looking at the Oswald efficiency factor. Increasing the number of spanwise panels, clearly has a big influence on the simulation results. For the lift and induced drag coefficient, the result seems to be relatively stable if *Num_U* is set on anything else than the absolute minimum of 2.

The reader has to know that increasing *Num_U* has a very strong influence on the solution time. At *Num_U* = 12, the solution time was 1.528 seconds, for *Num_U* = 24, this was 4.142 seconds, and for the maximum *Num_U* = 96, the solution time was 39.864 seconds.

Out of the results and recommendations given in the Google Discussion Group, all following experiments are done with a panel to span ratio close to one.

$$\frac{Num\_U}{Span} \approx 1 \qquad\qquad (4.2)$$

4.4 Clustering

Clustering arranges the distance between two slices. This only affects the wireframe and the analysis related to it (VSPAERO, CompGeom, DegenGeom, etc.). Clustering does not affect the underlying shape or surface parameterization. Setting the clustering parameters to 1.0 (default for spanwise clustering) provides a uniform spacing. Values smaller than 1.0 will cluster and larger numbers will spread things out.

4.4.1 Chordwise Clustering

Chordwise, this is controlled by leading edge and trailing edge clustering. Figure 4.16 gives multiple examples of chordwise clustering. Here, the spanwise clustering is set to 1.00 for both tip and root cluster.

The figure on the right shows te default chordwise clustering setting, where the LE and TE are both equal to 0.25. As this has had very little influence on the simulation results, this is kept that way troughout all following experiments.
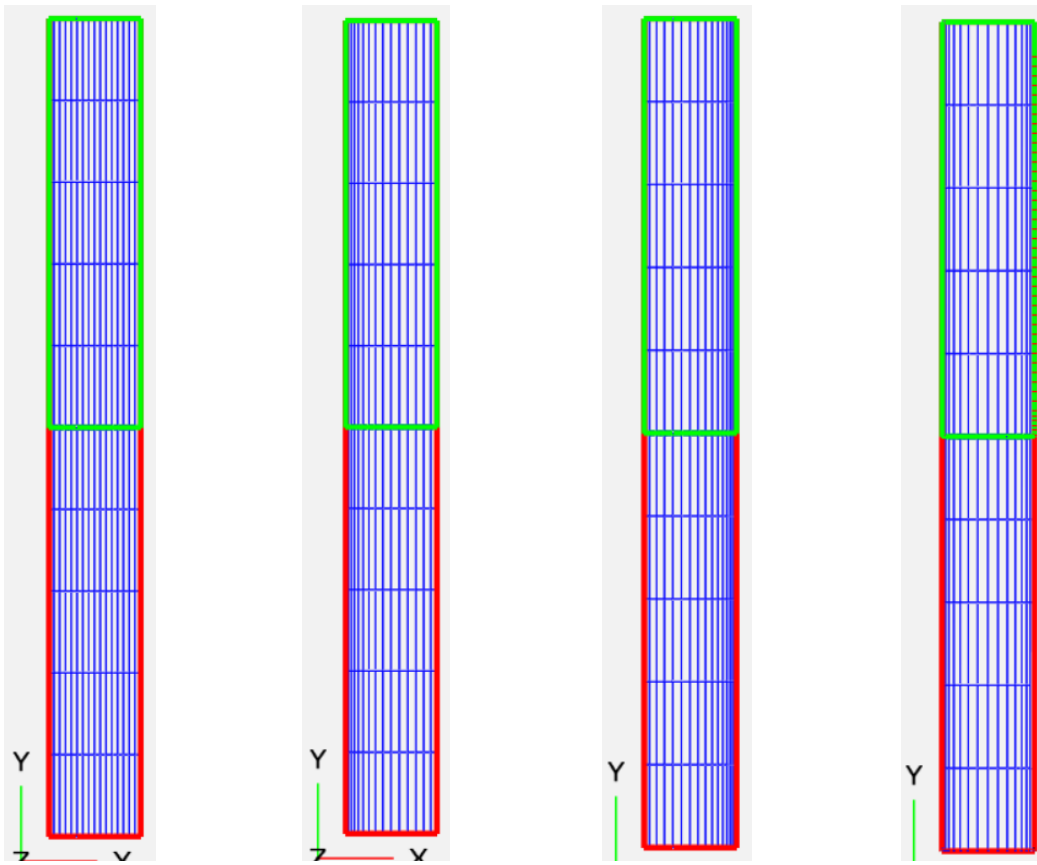
Figure 4.16   Different chordwise cluster examples at constant Num_W. From left to right: LE = 1.00, TE = 1.00; LE = 0.25, TE = 1.0; LE = 1.00, TE = 0.25; LE = 0.25, TE = 0.25.

4.4.2 Spanwise Clustering

Spanwise this is managed by root and tip clustering. This is made visual by Figure 4.17, where the chordwise clustering is set to 1.00 for LE and TE clustering on the left. Usually, the tip cluster is set to a smaller value than one. Hereby, the tip vortices will be simulated with more detail.
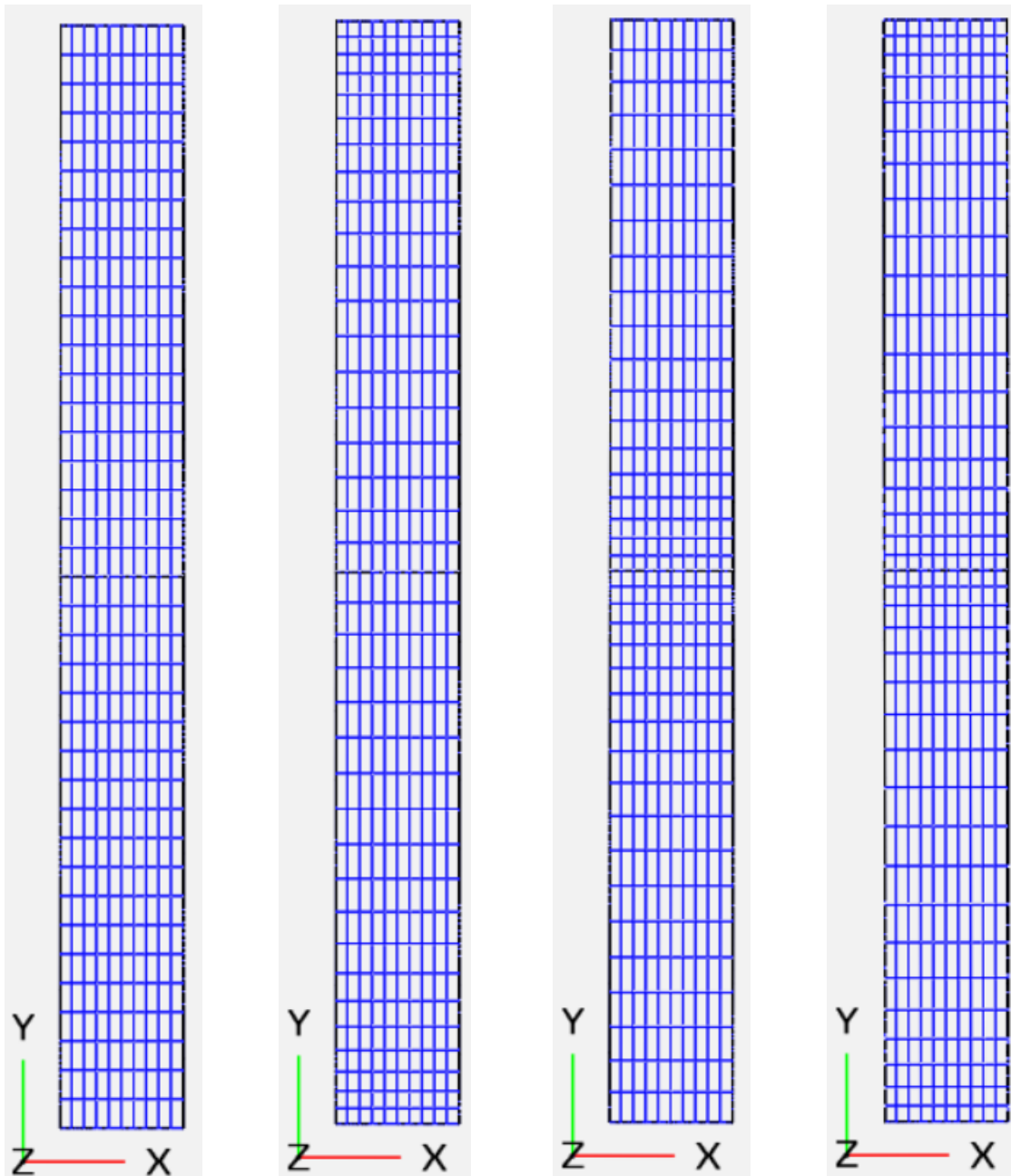
Figure 4.17   Different spanwise cluster examples at constant Num_W and Num_U. From left to right: Root = 1.00, Tip = 1.00; Root = 1.0, Tip = 0.50; Root = 0.50, Tip = 1.00; Root = 0.50, Tip = 0.50.

From personal advice by Rob McDonald (OpenVSP Core Team) all experiments are done with Root Cluster equal to 1.00 and Tip Cluster set to 0.50.

5   Lift Curve Slope

Chapter 5 discusses the lift curve slope obtained by simulations done with VSPAERO, using VLM as well as the panel method. First, there is a brief theoretical background about what the lift curve is. After that, a reference textbook calculation is done. This is compared with the results gained by VSPAERO. The textbook calculation and simulations are done for three cases. First, a rectangular wing is considered. After that, a swept, untapered wing is studied. The last case is the examination of a swept, tapered wing.

The lift curve will first be calculated and afterwards simulated for a range of angle of attack *AoA* going from -10° to +10°, for eleven points. This makes that there's a sample point at every round number in this range.

5.1   Theoretical Background

Lift, drag, and pitching moment are mostly converted into a dimensionless coefficient form as this allows transferability. The lift, drag, and pitching moment coefficients are defined as shown Figure 5.1(Gudmundsson 2014). In Equation (5.3) *M* stands for moment around the aerodynamic centre instead of Mach number as stated on page 16.

$$L = \frac{1}{2} \cdot \rho \cdot V^2 \cdot S \cdot C_L \tag{5.1}$$

$$D = \frac{1}{2} \cdot \rho \cdot V^2 \cdot S \cdot C_D \tag{5.2}$$

$$M = \frac{1}{2} \cdot \rho \cdot V^2 \cdot S \cdot C_M \tag{5.3}$$
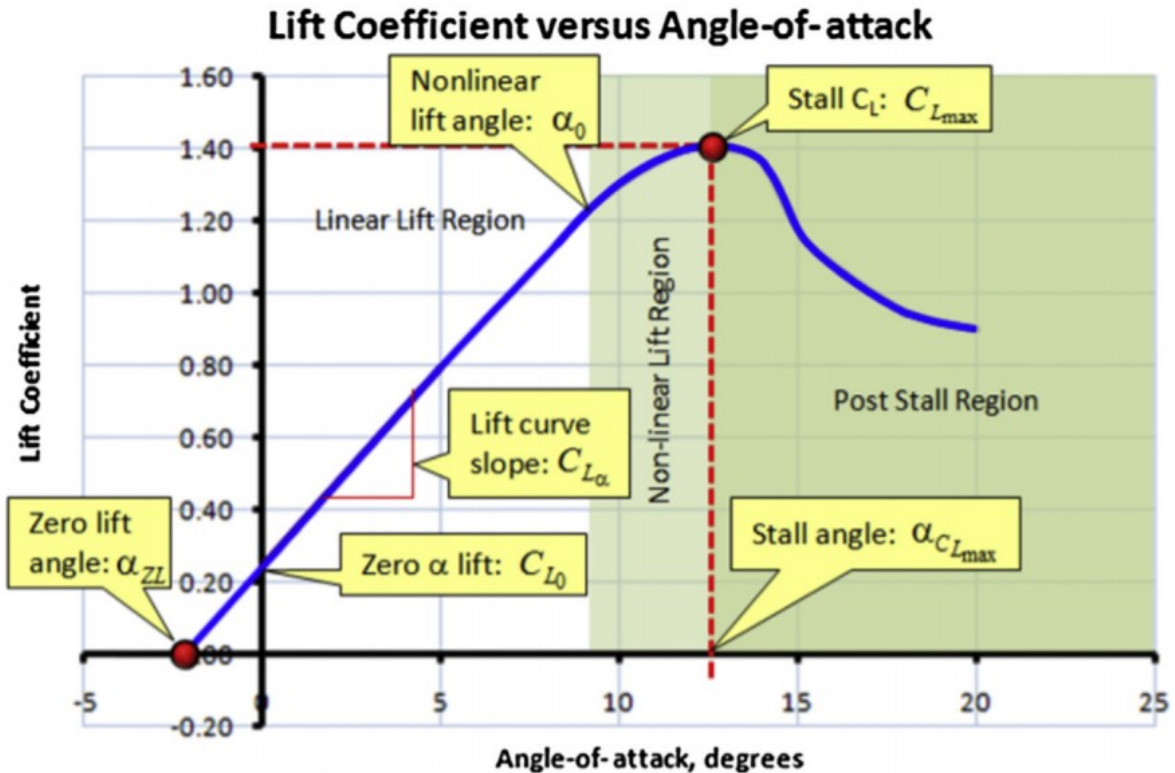
Figure 5.1   Important properties of the lift curve (Gudmundsson 2014).

The lift curve, as shown in Figure 5.1, indicates how lift developed by an airfoil changes with angle-of-attack. In this curve, there is always a linear range, wherein one can estimate the lift coefficient for any *AOA* using a simple linear expression, as in (5.4). The extend of this linear region depends on the geometry and operational speeds. The slope of this region is known as the lift curve slope, $C_{L\alpha}$ (Gudmundsson 2014).

$$C_L = C_{L0} + C_{L\alpha} \cdot \alpha \tag{5.4}$$

The lift curve slope can then be described as the first derivative of the lift coefficient to angle of attack (DATCOM 1978).

$$C_{L\alpha} = \frac{dC_L}{d\alpha} \tag{5.5}$$

The other parameter in (5.4) is known as the lift coefficient at zero *AOA, C_{L0}*. This is important in the selection of the airfoil as it will affect the angle-of-incidence at which the wing must be mounted. For the three common airfoils, the following accounts (Hull 2007).

- Positive cambered airfoil $C_{L0} > 0$
- Symmetrical airfoil $C_{L0} = 0$
- Negative cambered airfoil $C_{L0} < 0$

Because of camber, also the angle of zero lift α_{ZL} will vary. Again, for positive cambered, symmetrical or negative cambered airfoils, the following counts.

- Positive cambered airfoil $\alpha_{ZL} < 0$
- Symmetrical airfoil $\alpha_{ZL} = 0$
- Negative cambered airfoil $\alpha_{ZL} > 0$

(Gudmundsson 2014)

The influence of the camber of an airfoil on its lift cuve is made visual in Figure 5.2.
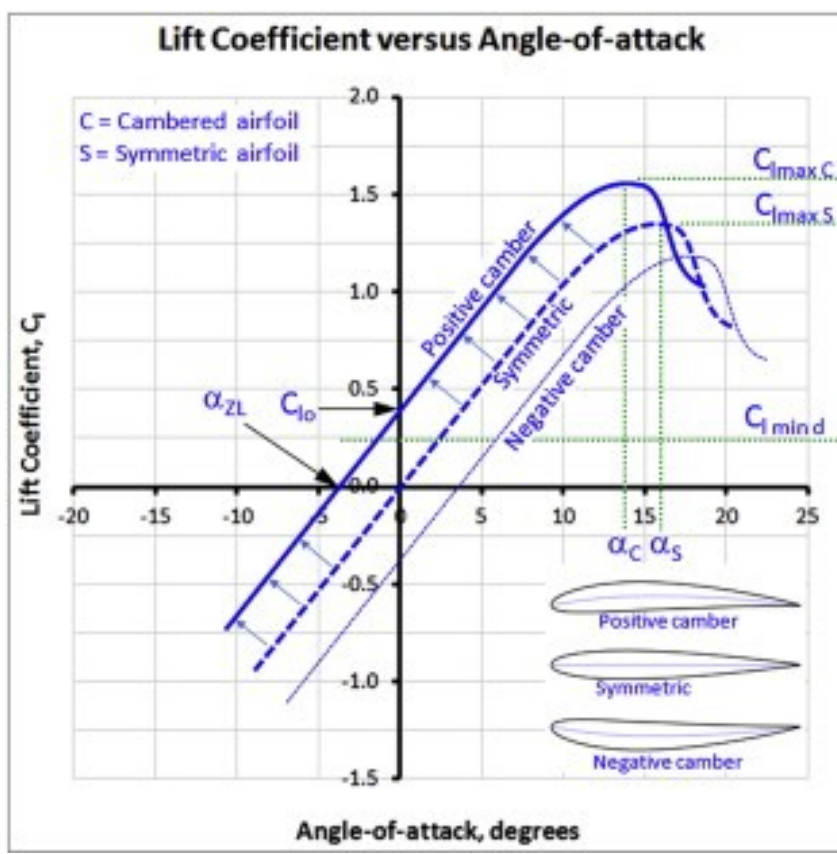
Figure 5.2   The effect of camber on the lift curve (Gudmundsson 2014).

5.2 Calculation

This calculation supposes air in ISA environment, taken at SSL, which is defined as given in Table 5.1 (Wikipedia 2021a).

Table 5.1   ISA environment, taken at SSL (Wikipedia 2021a).

Temperature	T	15 °C
Temperature	T	288.15 K
Pressure	P	101325 Pa
Density	ρ	1.2250 kg/m³
Specific gas constant of dry air	R	287.058 J/kgK
Adiabatic factor of air	γ	1.4
Kinematic viscosity coefficient of air	v	$1.4607 \cdot 10^{-5}$ m²/s

The lift curve slope is calculated according to (DATCOM 1978), Section 4.1.3.2. Note that this is for a wing on it's own and does not count for wing-fuselage or wing-fuselage-empannage combinations.

$$C_{L\alpha} = \frac{2\pi \cdot A}{2 + \sqrt{\frac{A^2 \cdot \beta^2}{\kappa^2}\left(1 + \frac{\tan^2(\varphi_{50})}{\beta^2}\right) + 4}} \tag{5.6}$$

$C_{L\alpha}$	lift curve slope of the wing,
A	aspect ratio,
β	reciprocal of the Mach Number correction factor,
φ_{50}	sweep angle at 50% line (line formed by the geometric locations of the 50% points of the chords),
κ	ratio of the two-dimensional lift-curve slope (per radian) at the appropriate Mach number to $2\pi/\beta$.

The aspect ratio of a wing is defined as the square of the wing span b to the projected wing area S (Hull 2007).

$$A = \frac{b^2}{S} \tag{5.7}$$

β can be calculated as

$$\beta = \sqrt{1 - M^2} \quad , \tag{5.8}$$

and

$$\kappa = \frac{C_{L,\alpha}}{2\pi/\beta} \quad .$$

(5.9)

In (5.9), $C_{L,\alpha}$ is the lift curve slope of the airfoil section, which can be estimated from

$$C_{L,\alpha} = \frac{1.05}{\beta} \cdot \left[\frac{C_{L,\alpha}}{\left(C_{L,\alpha} \right)_{theory}} \right] \cdot \left(C_{L,\alpha} \right)_{theory} \quad .$$

(5.10)

Data necessary for (5.10) can be obtained from Figure 5.3 and the theoretical lift curve slope of the airfoil can be calculated as

$$\left(C_{L,\alpha} \right)_{theory} = 2 \cdot \pi + 4.7 \cdot \left(t/c \right) \cdot \left[1 + 0.00375 \cdot \phi_{TE} \right]$$

(5.11)

In Equation (5.11), ϕ_{TE} is the trailing edge angle, according to Figure 5.4, in degrees. (5.11) gives the result of $\left(C_{L,\alpha} \right)_{theory}$ in 1/radian [1/rad].
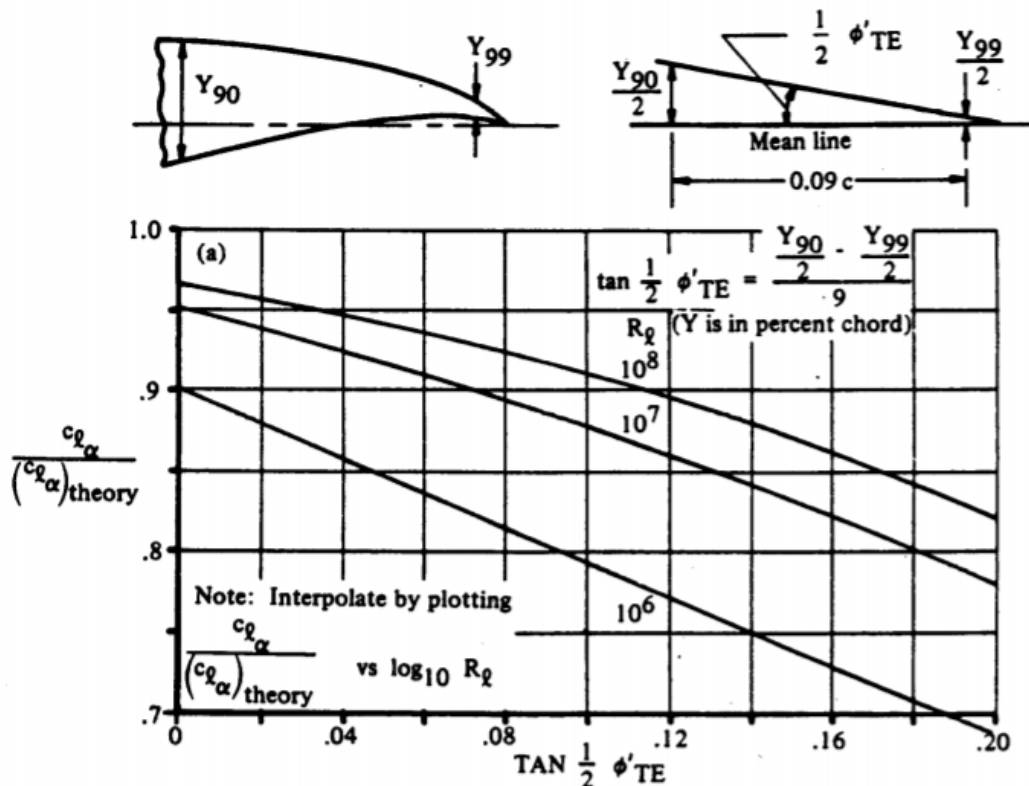
Figure 5.3   Calculating the lift curve slope of an airfoil section according to (DATCOM 1978).
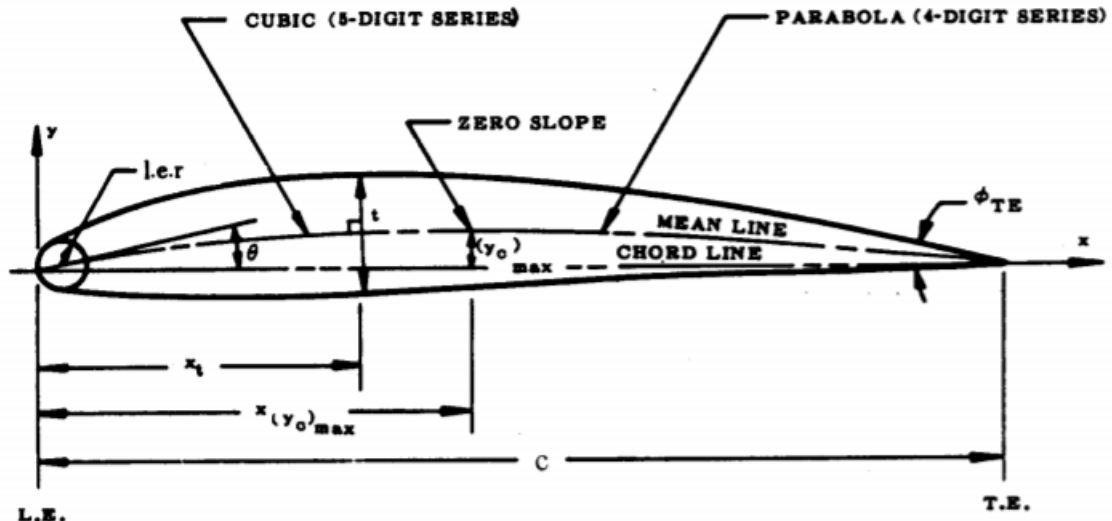
Figure 5.4   General representation of an airfoil geometry (DATCOM 1978).

5.2.1   NACA 0010

For this experiment, the default airfoil of OpenVSP is used. This is the NACA 0010 airfoil. Data for this airfoil is gathered from (Abbott 1959).

The model used for these simulations has these parameters:
- Chord c 2 m,
- Span b 18 m,
- Mach number M 0.2.

Therefore, the projected area S is equal to 36 m², which gives an aspect ratio A of 9.

To start calculating the lift cure slope of the airfoil section, see (5.10), (5.11) has to be solved first. Herefore, $\frac{Y_{99}}{2}$ and $\frac{Y_{90}}{2}$ is needed, as well as the thickness over chord ratio t/c. (Abbott 1959) gives

$$\frac{Y_{99}}{2} = 0.00105 \quad,$$

$$\frac{Y_{90}}{2} = 0.01207 \quad,$$

$$t/c = 0.1000 \quad.$$

With this, the tangent of half of the angle of the trailing edge is calculated with

$$\tan\left(\frac{1}{2}\phi'_{TE}\right) = \frac{\frac{Y_{90}}{2} - \frac{Y_{99}}{2}}{9\%} \tag{5.12}$$

$$\tan\left(\frac{1}{2}\phi'_{TE}\right) = \frac{0.01207 - 0.00105}{9\%} \quad,$$

$$\tan\left(\frac{1}{2}\phi'_{TE}\right) = 0.1224 \quad.$$

And therefore it is

$$\phi_{TE} = 2 \cdot \tan^{-1}\left(\frac{\frac{Y_{90}}{2} - \frac{Y_{99}}{2}}{9\%}\right) \quad, \tag{5.13}$$

$$\phi_{TE} = 2 \cdot \tan^{-1}(0.1224) \quad,$$

$$\phi_{TE} = 13.9616° \quad.$$

Taking this into (5.11) gives

$$\left(C_{L,\alpha}\right)_{theory} = 2 \cdot \pi + 4.7 \cdot (0.1000) \cdot [1 + 0.00375 \cdot 0.1224] = 6.78 \left[\frac{1}{\text{rad}}\right] \quad. \tag{5.14}$$

The next parameter needed to solve (5.10) is $\frac{C_{L,\alpha}}{(C_{L,\alpha})_{theory}}$, which can be readed from Figure 5.3. For this, the Reynolds number Re is needed, calculated by (5.15). This is where the assumption if the ISA circumstances comes in.

$$\text{Re} = \frac{V \cdot L}{\nu} \tag{5.15}$$

According to (5.15) that the free stream velocity V is needed. The reference length L for an airfoil is equal to its chord. The Mach number M is defined as the ratio of the free stream velocity V to the speed of sound c. The speed of sound can be calculated as stated in (5.17).

$$M = \frac{V}{c} \tag{5.16}$$

With

$$c = \sqrt{\gamma \cdot R \cdot T} \quad . \tag{5.17}$$

Filled in considering ISA at SSL gives

$$c = \sqrt{1.4 \cdot 287.058 \left[\text{J} \big/ \text{kgK} \right] \cdot 288.15 [\text{K}]} = 340.297 \text{ m/s} \quad .$$

Calculating the free stream velocity using (5.16) gives

$$V = M \cdot c = 0.2 \cdot 340.297 \text{ [m/s]} = 68.059 \text{ m/s} \quad .$$

Having this, allows the calculation of the Reynolds number as stated in (5.15)

$$\text{Re} = \frac{68.059 \left[\frac{\text{m}}{\text{s}} \right] \cdot 2 \text{ m}}{1{,}4607 \text{ [m}^2/\text{s]}}$$

$$= 93.1874 \cdot 10^5 \quad .$$

The next step is to read $\dfrac{C_{L,\alpha}}{(C_{L,\alpha})_{theory}}$ from Figure 5.3. To do so, interpolation with $\log_{10}(\text{Re})$ is needed. Doing so gives

$$\log_{10}(93.1631 \cdot 10^5) = 6.969 \approx 7 \quad .$$

Reading from Figure 5.3, for a $\tan\left(\frac{1}{2}\phi'_{TE}\right)$ equal to 0.1224 and the curve noted with 10^7, makes that $\dfrac{C_{L,\alpha}}{(C_{L,\alpha})_{theory}}$ is estimated at $\dfrac{C_{L,\alpha}}{(C_{L,\alpha})_{theory}} = 0.86$, see Figure 5.5.
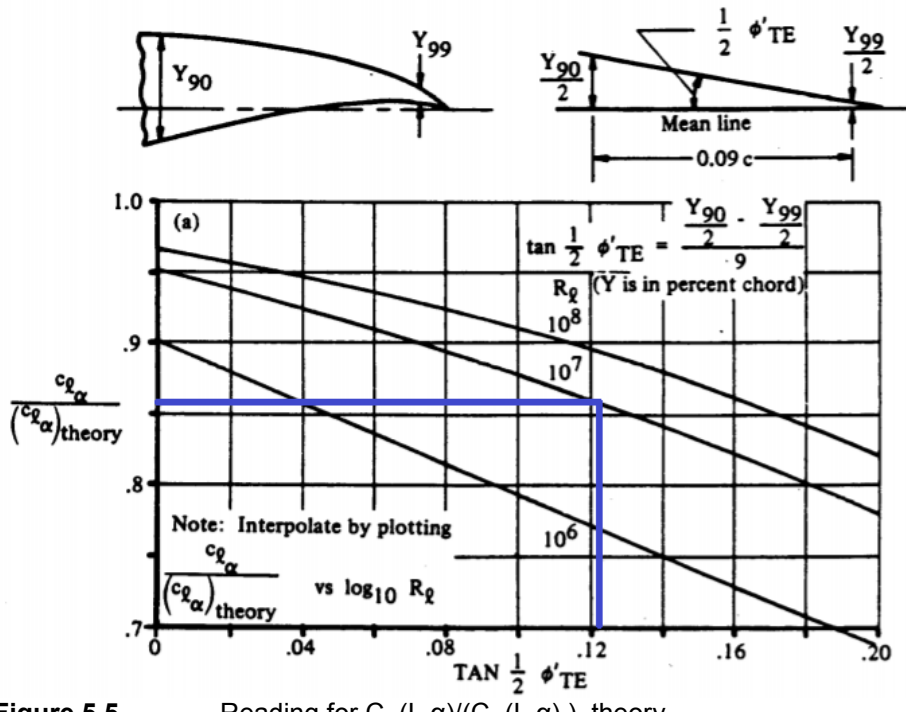
Figure 5.5   Reading for C_(L,α)/(C_(L,α))_theory.

This can then all be brought together in (5.10), to calculate the lift curve slope of the airfoil section

$$C_{L,\alpha} = \frac{1.05}{\sqrt{1 - 0.2^2}} \cdot [0.86] \cdot 6.78 = 6.24859 \quad .$$

Using this, κ is calculated from (5.9).

$$\kappa = \frac{6.24859}{2\pi \Big/ \sqrt{1 - 0.2^2}}$$

$$= 0.974401$$

As according to Scholz (2017) κ is close to the unity.

Now, everything to calculate the theoretical lift curve slope for the three cases is available. These calculations will be done in the next section.

5.2.2   Rectangular Wing

Obviously, the half chord sweep φ_{50} of a rectangular wing is equal to 0°. Knowing this, the theoretical lift curve slope of the wing is calculated using Equation (5.6).

$$C_{L\alpha} = \frac{2\pi \cdot 9}{2 + \sqrt{\frac{9^2 \cdot (1 - 0.2)}{0.974401^2}\left(1 + \frac{\tan^2(0)}{(1 - 0.2)}\right) + 4}}$$

$$= 5.01843/\text{rad}$$

$$= 0.087588/°$$

The linear part of this lift curve slope can be described as (with α in degrees)

$$C_L = 0.087588 \cdot \alpha + 0 \quad .$$

The explicit lift coefficient at every *AoA* can then be calculated with (5.4). Because the NACA 0010 is a symmetrical airfoil, C_{L0} will be equal to zero.

Table 5.2   Explicit lift coefficient for the rectangular wing calculated with (5.4).

AoA [°]	-10	-8	-6	-4	-2	0	2	4	6	8	10
CL [/]	-0.876	-0.701	-0.526	-0.350	-0.175	0	0.175	0.350	0.526	0.701	0.876

5.2.3   Untapered Swept Wing

The second case is an untapered swept wing. The sweep is constant for the whole span, set at 20°. Thus the half chord sweep is 20° (as well as the quarter chord sweep φ_{25}):

$$C_{L\alpha} = \frac{2\pi \cdot 9}{2 + \sqrt{\frac{9^2 \cdot (1 - 0.2)}{0.974401^2}\left(1 + \frac{\tan^2(20°)}{(1 - 0.2)}\right) + 4}}$$

$$= 4.76839/\text{rad}$$

$$= 0.083224/°$$

The linear part of this lift curve slope can be described as (with α in degrees)

$$C_L = 0.083224 \cdot \alpha + 0 \quad .$$

Again, the explicit lift coefficient at every *AoA* can be calculated with (5.4). Because the NACA 0010 is a symmetrical airfoil, it's C_{L0} will be equal to zero.

Table 5.3   Explicit lift coefficient for the untapered swept wing calculated with (5.4).

AoA [°]	-10	-8	-6	-4	-2	0	2	4	6	8	10
CL [/]	-0.832	-0.666	-0.499	-0.333	-0.167	0	0.167	0.3329	0.499	0.666	0.832

5.2.4   Tapered Swept Wing

According to Torenbeek (1982) every wing with a sweep has an optimum taper ratio for sthe smallest induced drag, to get closer to the elliptical lift distribution. This optimum taper ratio according to Torenbeek (1982) can be estimated by

$$\lambda_{opt} = 0.45 \cdot e^{-0.036 \cdot \varphi_{25}} \quad . \tag{5.18}$$

In (5.18), the quarter chord sweep angle is entered in degrees and *e* is the Euler number.

Filling this in for a sweep of 20° gives

$$\lambda_{opt} = 0.45 \cdot e^{-0.036 \cdot 20°}$$

$$= 0.219 \quad .$$

For the simulations of the tapered swept wing, the taper ratio will be set at 0.219. Theoretically, this will not be of any influence on the theoretical lift curve slope. $C_{L\alpha}$ will therefore stay the same as the untapered swept wing (0.083224/°), what makes that also the specific lift coefficient at every point will be the same (see Table 5.3).

5.3   Simulation

5.3.1   Rectangular Wing

Here, the first case will be discussed. The model consists of a simple, rectangular wing with, as said, a span of 18 m and a chord of 2 m, shown in Figure 5.6.

After creating the model, VSPAERO is set up for simulation. The reference area and lengths are taken from the model, and the center of gravity is calculated by clicking the button. For these simulations, the number of iterations *Num It* was set on 50, with 64 wake nodes. Those can be changed on the "*Advanced*"-tab. Other properties of the set-up are visible in Figure **5.7**. Changing between VLM and Panel Method is possible by just the click of a button.
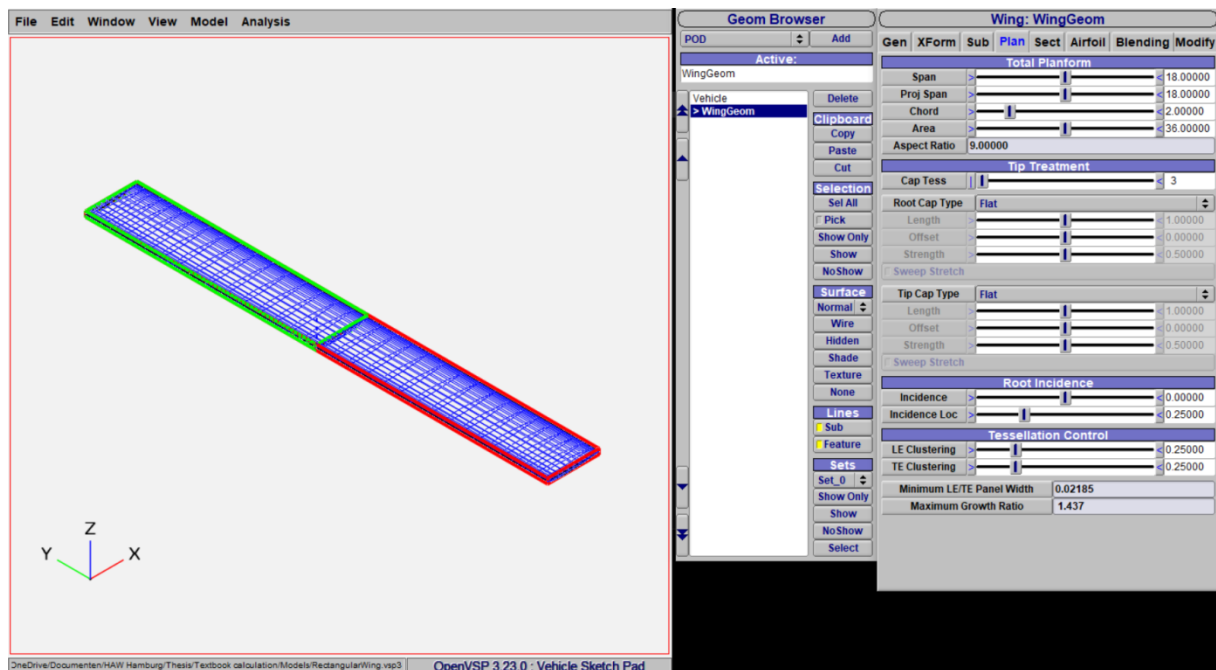
Figure 5.6   Model for the lift curve slope simulation of the rectangular wing.
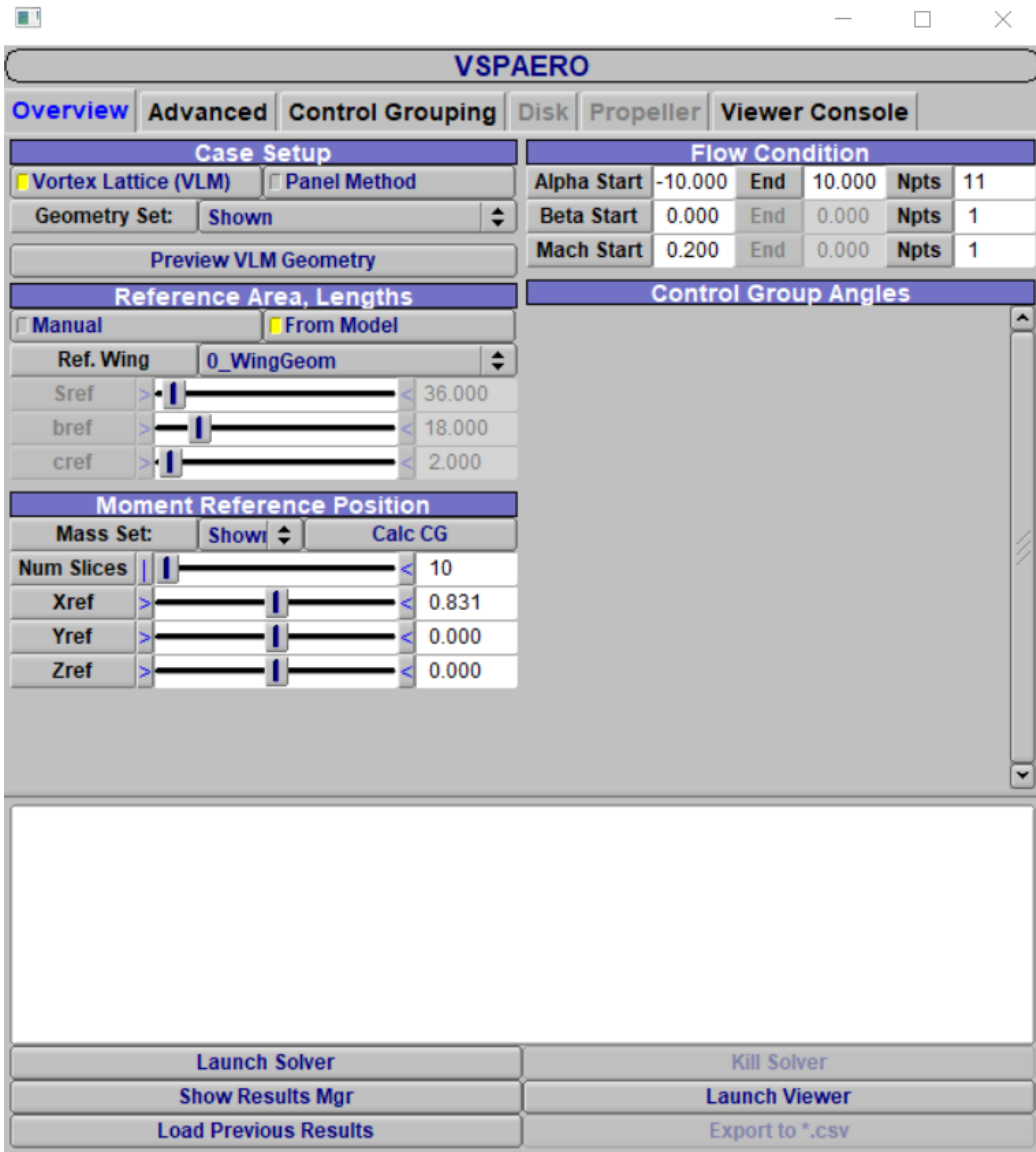
Figure 5.7   Simulation set-up for the lift curve slope simulation of the rectangular wing.

Now, the simulation results will be discussed, first for VLM and afterwards for the Panel method.

VLM

The results for the VLM simulation is shown in Table 5.4 and made visual by Figure 5.8. Also, the percentage deviation PD is calculated, as stated in (5.19).

$$PD = \left(\frac{Simulated-Calculated}{Calculated}\right) \cdot 100\% \qquad (5.19)$$
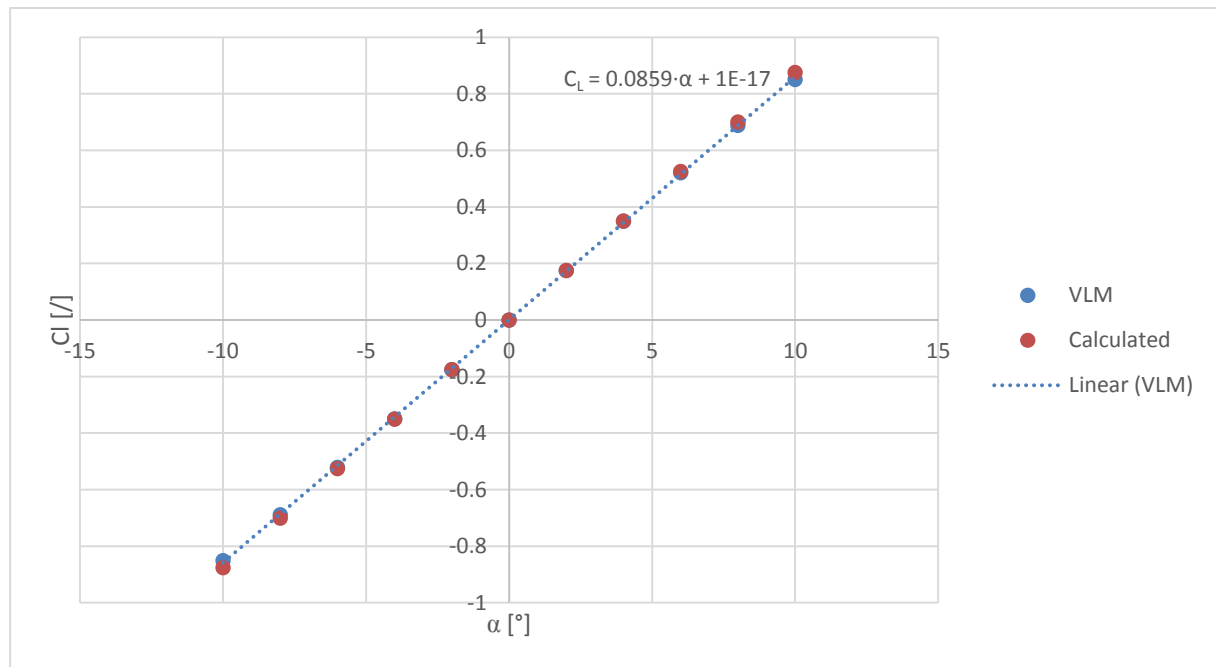
Wherein *Simulated* stands for the lift coefficient gathered by the simulation, and *Calculated* for the theoretical calculation (Table 5.2).

Table 5.4   Results for VLM simulation of the rectangular wing.

Alpha (°)		-10	-8	-6	-4	-2	0	2	4	6	8	10
C_L	Simulated	-0.851	-0.689	-0.521	-0.350	-0.175	0	0.175	0.350	0.521	-0.689	0.851
	Calculated	-0.876	-0.701	-0.526	-0.350	-0.175	0	0.175	0.350	0.526	0.701	0.876
PD [%]		-2.853	-1.739	-0.866	-0.241	0.139	/	0.139	-0.241	-0.866	-1.739	-2.853

Clearly, the simulated and calculated are very close to each other. The biggest deviation is to be found at the outer bounds of the tested range. But with a maximum deviation lower than 3%, it can be concluded that for this simulation, VSPAERO, using VLM, provides very satisfying results.

This is enforced by Figure 5.8. The graph shows the calculated values as well as the simulation results. Also, the linear trendline for the simulation results, with the corresponding equation, is shown. Comparing it's slope with the theoretical value (0.087588 /°), it can be concluded that also these values are very close to each other and therefore VLM provides correct results. The factor $1 \cdot 10^{-17}$ can be neglected because this is practically zero.
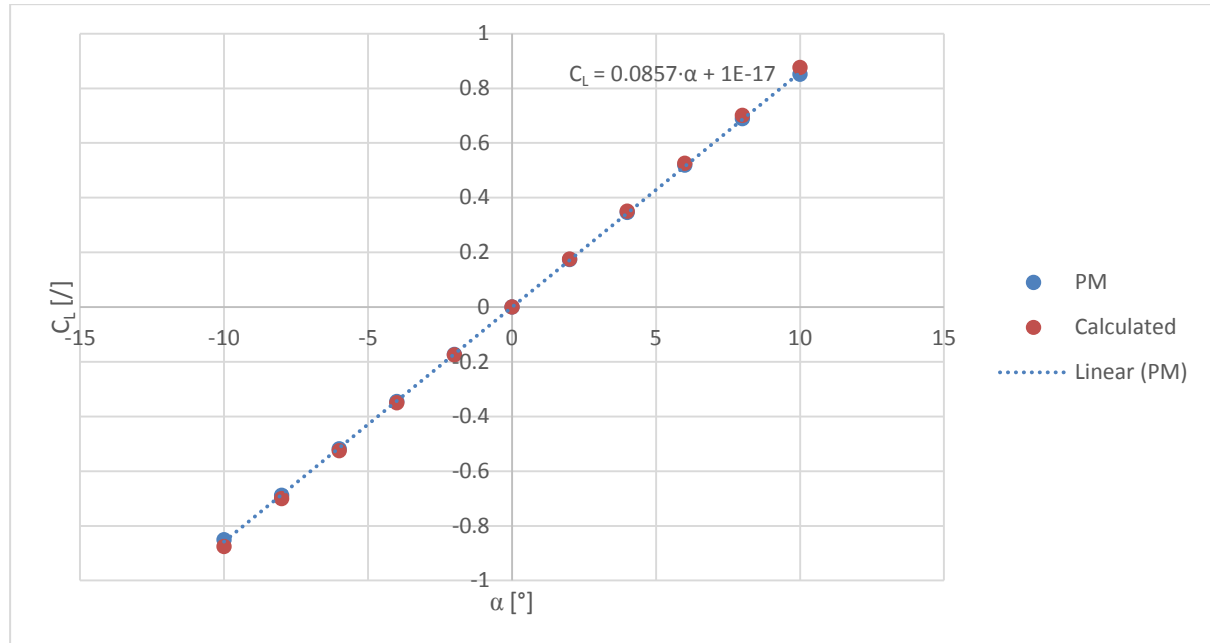
Figure 5.8   Graphical representation of the results for VLM simulation of the rectangular wing.

Panel Method

In this case, the panel method provided results, shown in Table 5.5 and made visual in Figure **5.9**, very similar to those when using VLM. Therefore the same conclusions can be made as when using VLM.

Table 5.5 Results for the panel method simulation of the rectangular wing.

Alpha (°)		-10	-8	-6	-4	-2	0	2	4	6	8	10
Cl	Simulated	-0.851	-0.689	-0.519	-0.346	-0.174	0	0.174	0.346	0.519	0.689	0.851
	Calculated	-0.876	-0.701	-0.526	-0.350	-0.175	0	0.175	0.350	0.526	0.701	0.876
PD [%]		-2.825	-1.717	-1.293	-1.322	-0.945	/	-0.945	-1.322	-1.293	-1.717	-2.825

Figure 5.9 Graphical representation of the results for the panel method simulation of the rectangular wing.

Because the results of this simulation are so similar to those when using VLM, the same conclusions can be made. For this case, using the panel method provides very satisfying results which is again confirmed by the equation of the trendline trough the results.

5.3.2 Untapered Swept Wing

After the rectangular wing, an untapered swept wing was examinated. The way of working is exactly the same as for the rectangular wing.

The only difference between the model from before and now, is that the sweep angle is set to 20° instead of 0° for the first case. The model for this simulation can be seen in Figure 5.10.

Again, the center of gravity is calculated by the click of the button. And also now, there are 50 iterations done for each point, for 64 wake nodes (Figure 5.11).
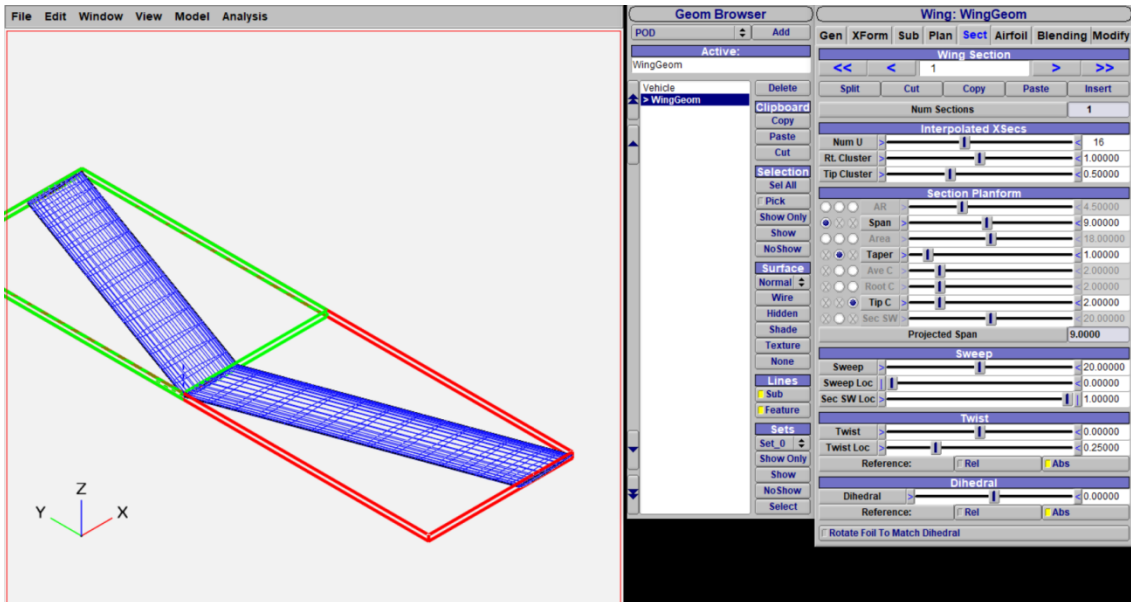
Figure 5.10   Model for the lift curve slope simulation of the 64ntampered swept wing.
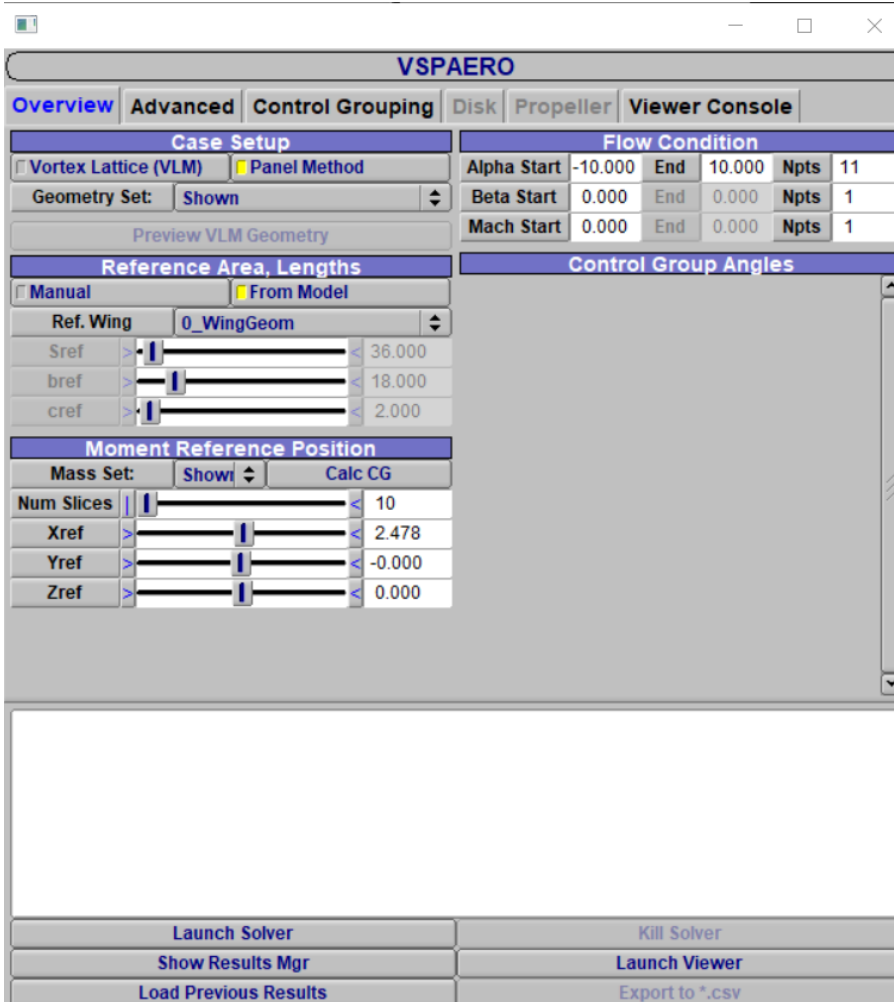
Figure 5.11   Simulation set-up for the lift curve slope simulation of the untampered swept wing.

Now, the simulation results will be discussed, first for VLM and afterwards for the Panel method.

VLM

Table 5.6   Results for VLM simulation of the untapered swept wing.

Alpha (°)		-10	-8	-6	-4	-2	0	2	4	6	8	10
CL	Simulated	-0.801	-0.648	-0.491	-0.329	-0.165	0	0.165	0.329	0.491	0.648	0.801
	Calculated	-0.832	-0.666	-0.499	-0.333	-0.167	0	0.167	0.333	0.499	0.666	0.832
PD [%]		-3.783	-2.635	-1.735	-1.087	-0.696	/	-0.696	-1.087	-1.735	-2.635	-3.787

Table 5.6 shows the results gathered by using VLM for the untapered swept wing with a constant sweep equal to 20°. Just as with the rectangular wing, the percentage deviation is the biggest at the extreme point of the tested range (AoA = -10° or +10°).

The maximum *PD* stays relatively small. It's maximum absolute value is smaller than 4%, which is still considered as good results. Those results are made visual by Figure 5.12. The slope of this results linear trendline, 0.0808 /°, is again very close to the theoretical value of 0.083224 /°. This gives a percentage deviation of about -3%, which is indeed small.
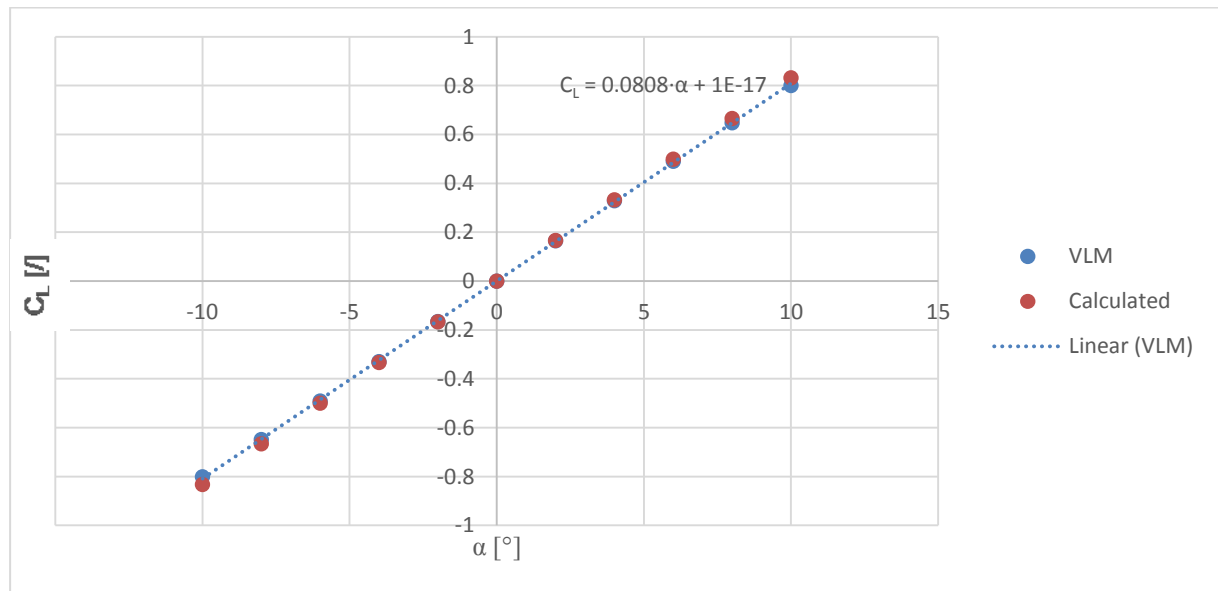
Figure 5.12   Graphical representation of the results for VLM simulation of the untapered swept wing.

Panel Method

When redoing the simulation, the results shown in Table 5.7 and Figure 5.13 are gained. The maximum percentage deviation now occur at the smallest absolute angles of attack (-2° and +2°), and at the extreme values, the percentage deviation is the smallest. This is in big contrast to the previous results, where it was the other way around, and therefore not really expected. Still, the maximum percentage deviation is lower than 5%, which is still very close to the theoretical value.

The slope of the linear trendline is for the first time greater than the theoretical value, namely 0.085 /° opposite to 0.083224 /°. With a percentage deviation smaller than 2%, this is nothing to be concerned about, on the contrary.

Table 5.7   Results for the panel method simulation of the untapered swept wing.

Alpha (°)		-10	-8	-6	-4	-2	0	2	4	6	8	10
CL	Simulated	-0.842	-0.682	-0.516	-0.346	-0.174	0	0.174	0.346	0.516	0.682	0.842
	Calculated	-0.832	-0.666	-0.499	-0.333	-0.167	0	0.167	0.333	0.499	0.666	0.832
PD [%]		1.196	2.358	3.269	3.924	4.315	/	4.315	3.924	3.269	2.358	1.196
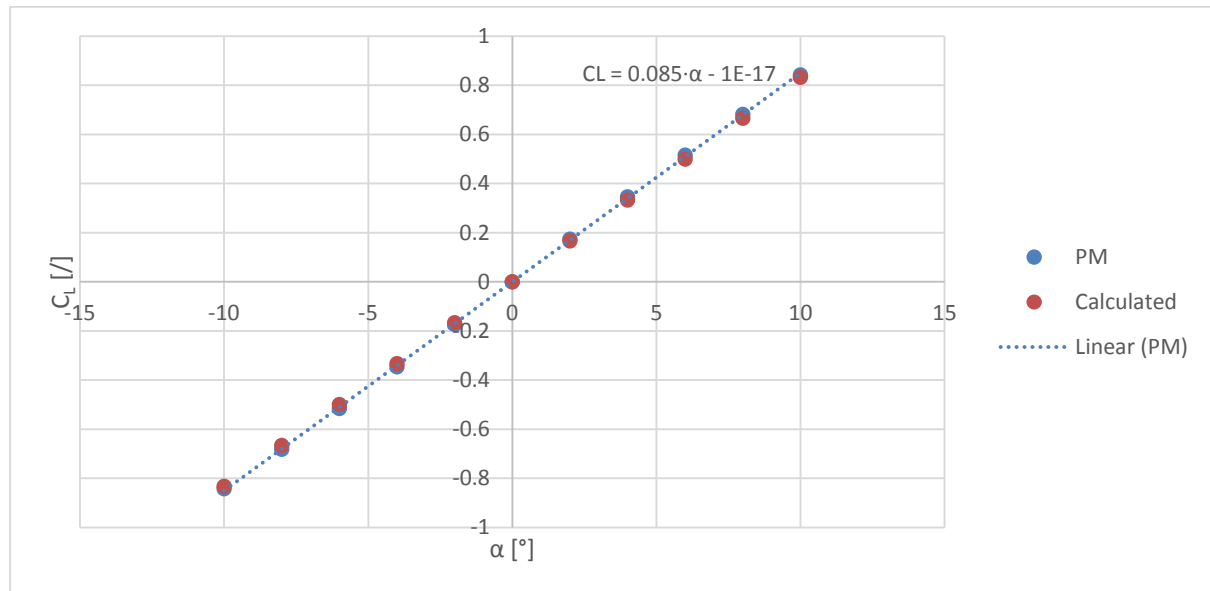
Figure 5.13   Graphical representation of the results for the panel method simulation of the untapered swept wing.

5.3.3 Tapered Swept Wing

The third and last case of this experiment, is, as said, the tapered swept wing, with a taper ratio (calculated according to (Torenbeek 1982), see (5.18)) equal to 0.219. As said before, it is expected to not have an influence on the lift generated by the wing.
The model used for this case is shown in Figure 5.14.

The only difference with previous simulations, is again that the location of the center of gravity changes. The set-up is shown in Figure 5.15. The number of iterations and wake nodes is kept the same as for the rectangular and untapered, swept wing.
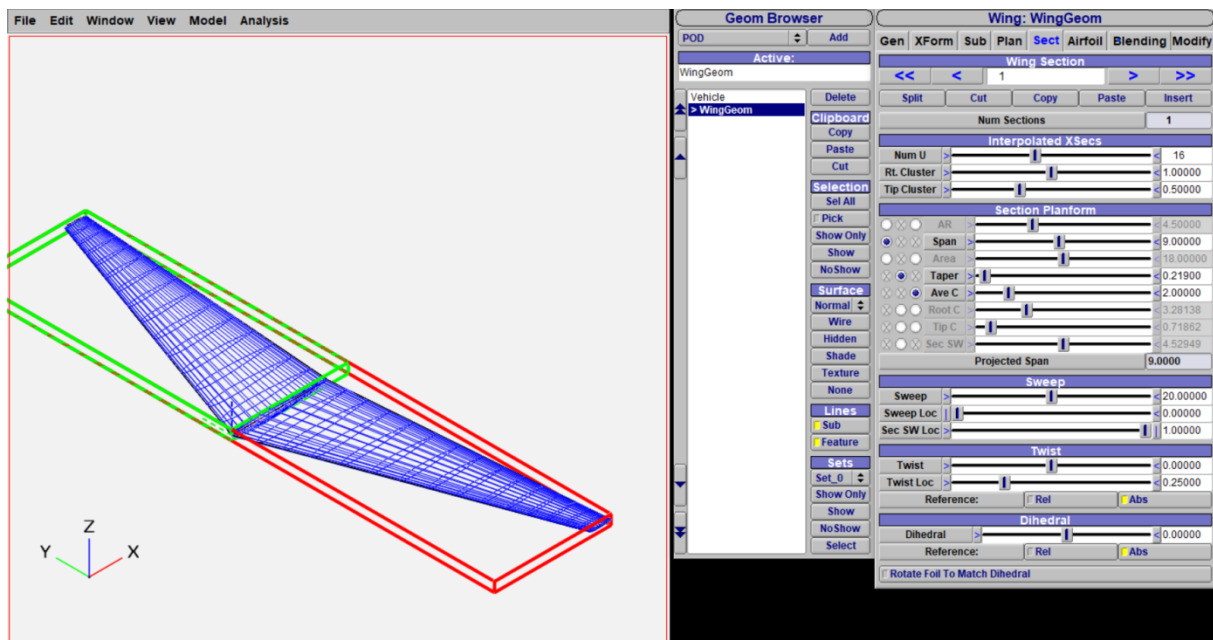
Figure 5.14   Model for the lift curve slope simulation of the tapered swept wing.
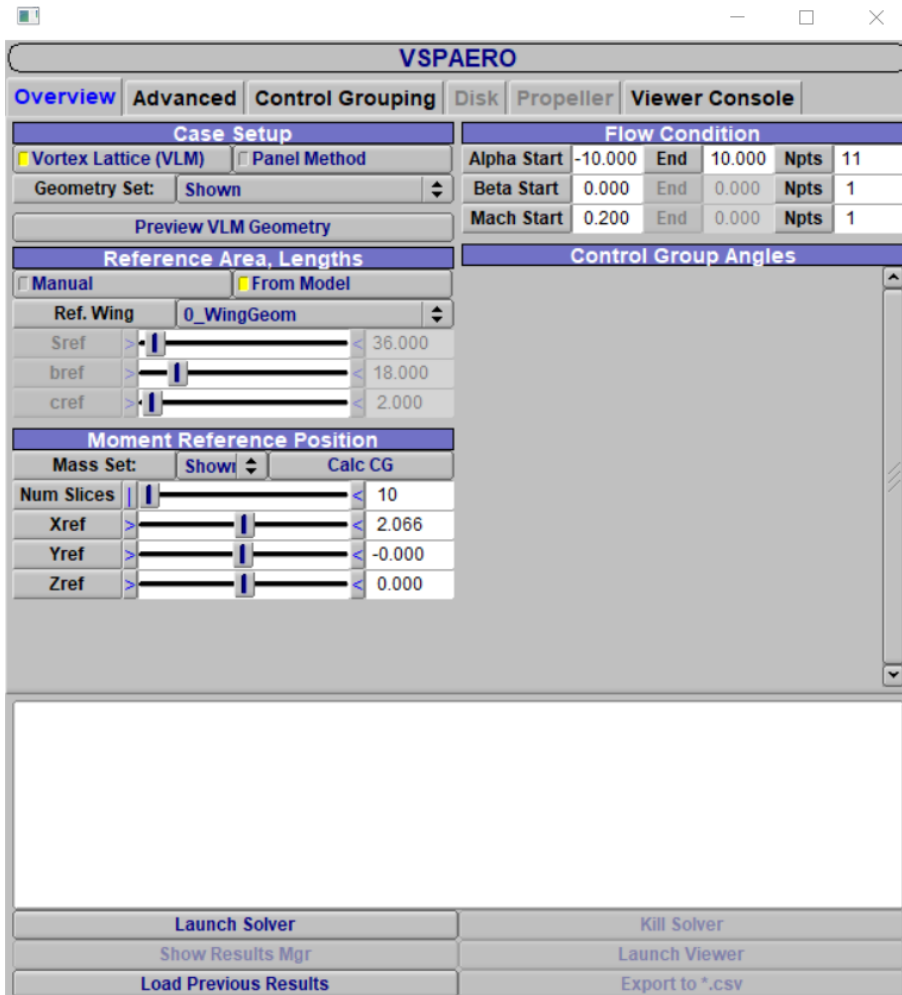
Figure 5.15   Simulation set-up for the lift curve slope simulation of the tapered swept wing.

Now, the simulation results will be discussed, first for VLM and afterwards for the Panel method.
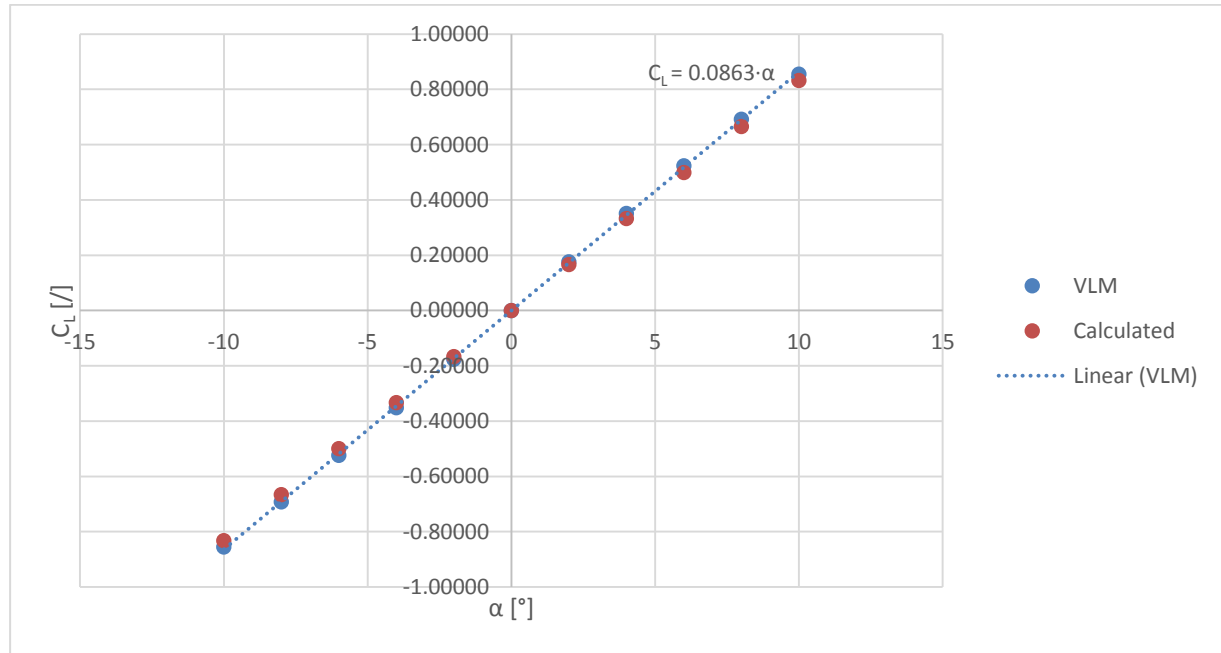
VLM

The results of the VLM suimulation of the tapered swept wing are shown in Table 5.8 and Figure 5.16. Here, the same trend as the panel method simulation of the untapered swept wing is seen. The biggest percentage deviation occurs at the angles of attack closest to zero. Again, this maximum deviation grew in comparison to previous simulations, which is something to keep an eye on in the future experiments. With a maximum percentage deviation smaller than 6%, the results are still considered as correct. The slope of 0.0863 /° confirms that the simulation results are still close to the theoretical values.

The results are still symmetrical. This means that the absolute value of the simulation result for an angle of attack of e.g. -6° is the same as for +6°. This counts for the whole simulation range.

Table 5.8   Results for VLM simulation of the tapered swept wing.

Alpha (°)		-10	-8	-6	-4	-2	0	2	4	6	8	10
CL	Simulated	-0.852	-0.692	-0.524	-0.351	-0.176	0	0.176	0.351	0.524	0.692	0.855
	Calculated	-0.832	-0.666	-0.499	-0.333	-0.167	0	0.167	0.333	0.499	0.666	0.832
PD [%]		2.756	3.938	4.865	5.531	5.931	/	5.931	5.531	4.865	3.938	2.756

Figure 5.16   Graphical representation of the results for VLM simulation of the tapered swept wing.
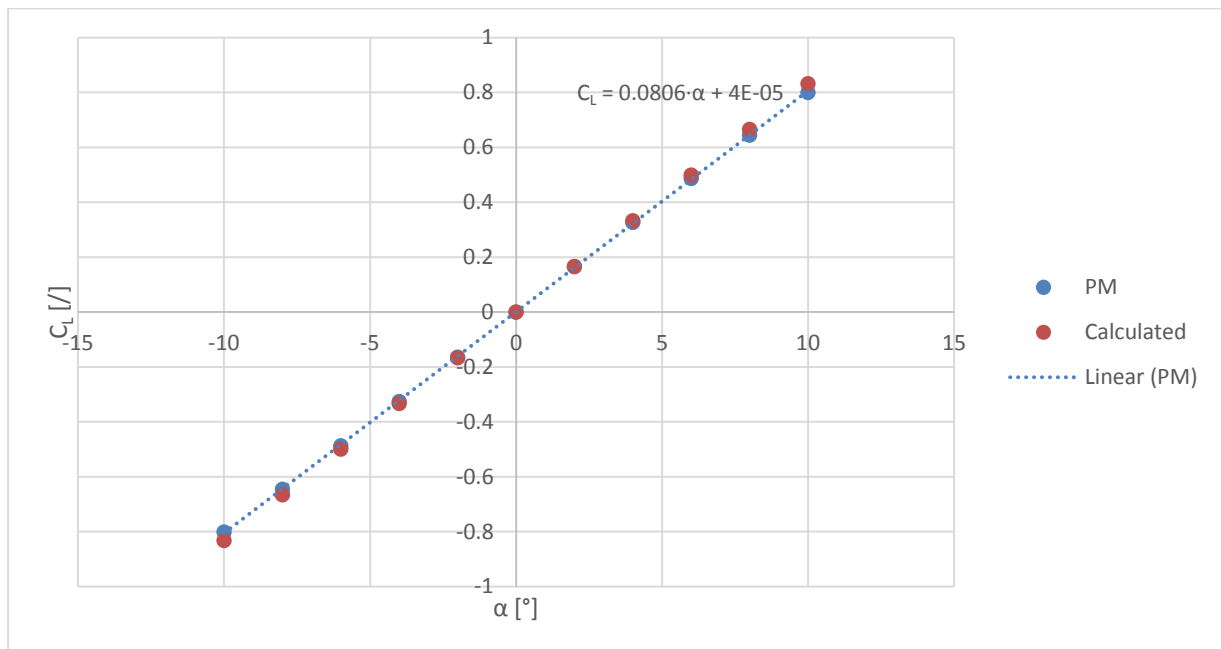
Panel Method

The results of the last simulation are shown in Table 5.9 and Figure 5.17. It immediately stands out that the results are not symmetrical anymore. Taking a look at +6° or -6°, the respective simulation results for C_L are +0.4868 and -0.48705. This difference is minimal, but cannot be ignored. A supposed expalation can be found in numerical roundings done by VSPAERO during the simulation.

The same trend as in the first simulations is found again. The biggest percentage deviations are found at the greatest angles of attack. With a maximum deviation of 4%, these results are considered as satisfying.

Table 5.9   Results for the panel method simulation of the tapered swept wing.

Alpha (°)		-10	-8	-6	-4	-2	0	2	4	6	8	10
CL	Simulated	-0.801	-0.645	-0.487	-0.326	-0.164	0	0.166	0.327	0.487	0.645	0.800
	Calculated	-0.832	-0.666	-0.499	-0.333	-0.167	0	0.167	0.333	0.499	0.666	0.832
PD [%]		3.876	3.163	2.524	2.207	1.431	/	0.603	1.875	2.577	3.265	4.021

Figure 5.17   Graphical representation of the results for the panel method simulation of the tapered swept wing.

6 Hoerner's Curve

As generally known, drag of a wing consists of two component, namely the zero-lift drag $C_{D,0}$ and the induced drag (due to the lift, caused by downwash) C_{Di}. To estimate this last, the *span efficiency factor*, better known as Oswald factor e, is needed. In preliminary sizing, usually typical values of e are taken, to shorten calculations. Nevertheless has every wing its appropriate value.

This chapter will try to find out whether VSPAERO can be used to gain reliable results for e. To do so, rectangular and tapered wings are examinated and compared with theoretical values.

6.1 Theoretical Background

Hoerner's curve $f(\lambda)$ is a function which describes the relationship between induced drag and the taper ratio of a wing geometry (Hoerner 1965).

The Oswald factor e, or as said the span efficiency factor, is a correction factor that represents the change in drag with lift considering a three-dimensional wing (or airplane), copared with the ideal wing having the same aspect ratio. The ideal wing has an elliptical lift distribution (Raymer 1992).

The absolute Oswald factor e includes a theoretical Oswald factor e_{theo} and correction factors which describe the effect of respectively fuselage $k_{e,F}$, viscous drag $k_{e,D0}$, and compressibility effects $k_{e,M}$.

$$e = e_{theo} \cdot k_{e,F} \cdot k_{e,D_0} \cdot k_{e,M} \qquad (6.1)$$

As said before, VSPAERO uses VLM or the panel method to do simulations. As stated in Chapter 0, this means that the flow is supposed to be inviscid. Therefore, the simulation result for e will be equal to e_{theo} of Equation (6.1).

For an elliptical wing, the induced drag will be minimum. Therefore, this is considered as an ideal and reference shape and it's Oswald factor is set to the unity, $e = 1$. Other shapes will always have an induced drag higher than the elliptical wing, and thus an Oswald factor smaller than one, $e < 1$. However, producing a elliptical wing is more difficult than a trapezoidal one, which has similar values for the Oswald factor. This is why very few planes had elliptical wings. The aircraft best known with a wing like this was the Supermarine Spitfire (Kroo 2007).

The induced drag coefficient is described by

$$C_{D,i} = \frac{C_L{}^2}{\pi \cdot A \cdot e} \quad .$$

(6.2)

There are many ways to calculate the Oswald factor. Niţă (2012) describes the curve $f(\lambda)$ derived by Hoerner with two equations.

$$e_{theo} = \frac{1}{1 + f(\lambda) \cdot A}$$

(6.3)

$$f(\lambda) = 0.0524 \cdot \lambda^4 - 0.15 \cdot \lambda^3 + 0.1659 \cdot \lambda^2 - 0.0706 \cdot \lambda + 0.0119$$

(6.4)

(6.3) can be reformed to

$$f(\lambda) = \frac{1 - e_{theo}}{A \cdot e_{theo}} \quad .$$

(6.5)

Here, the theoretical Oswald factor only depends on the geometry of the wing, the taper ratio λ and aspect ratio A. Hoerner's Equation (6.4) only depends on taper ratio. This value is later used to get to e_{theo} with (6.3).

(6.2) has e in the denominator. Obviously this means that $C_{D,i}$ will grow when e_{theo} gets smaller. But note that A has an impact on e_{theo} and $C_{D,I}$ as well. For a growing aspect ratio, (6.3) gives that accompanying e_{theo} will get smaller. As explained before, this would mean that the $C_{D,i}$ will grow. Important to note is that in (6.2) also the aspect ratio is in the denominator. Therefore, a growing A would have to have a decreasing effect on $C_{D,i}$ which is contradictory to what is explained before. All in all, it can be stated that $C_{D,i}$ gets smaller with increasing A, but not linearly (Budziak 2015).

Figure 6.1 represents Hoerner's function $f(\lambda)$. The function reaches a minimum, where e_{theo} will be maximum. The taper ratio where this counts is called the optimum taper ratio λ_{opt} and is equal to 0.357.
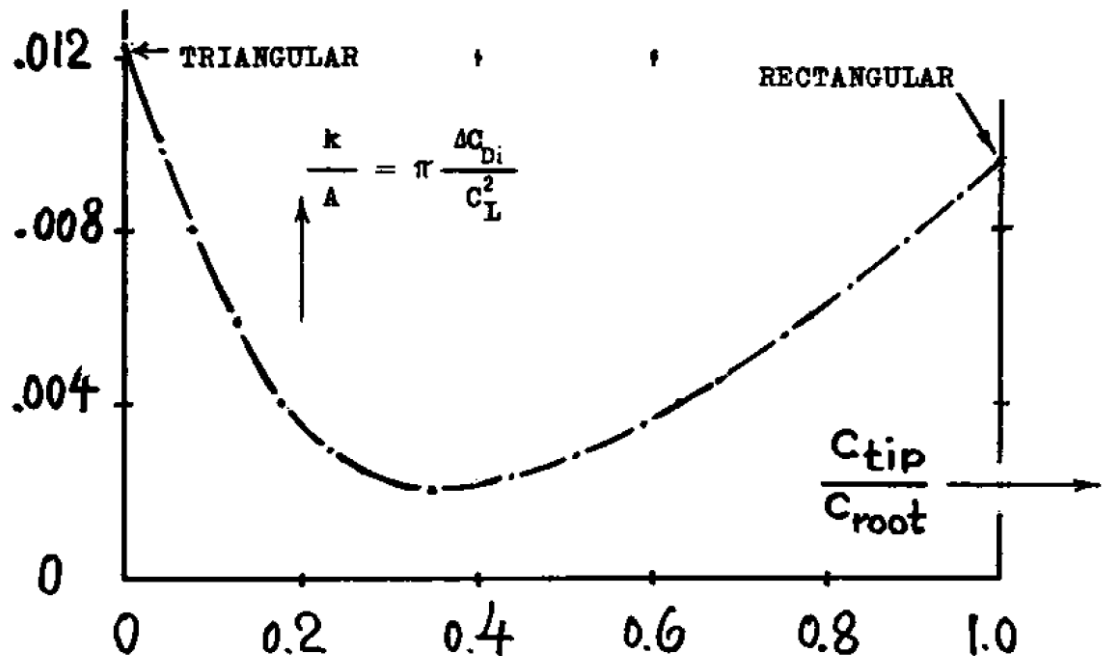
Figure 6.1   Additional induced drag of tapered wings, better known as Hoerner's Curve $f(\lambda)$ (Hoerner 1965).

6.2   Working Method

This experiment is executed in nine cases, which can be devided in two main groups. In one group, the taper ratio is held constant with a changing aspect ratio. The other group has a changing taper ratio with a constant aspect ratio.

Group 1:
Case 1: $\lambda = 1$ A = Variable
Case 2: $\lambda opt = 0.357$ A = Variable

Group 2:
Case 3: λ = variable $A = 5$
Case 4: λ = variable $A = 6$
Case 5: λ = variable $A = 7.5$
Case 6: λ = variable $A = 10$
Case 7: λ = variable $A = 20$
Case 8: λ = variable $A = 30$
Case 9: λ = variable $A = 40$

The first two cases examinate if the aspect ratio of a wing has an influence on the result for C_L, e, C_{Di}, or $f(\lambda)$. For every case from 3 to 9, a Hoerner Curve is constructed and compared to one another. Also, the difference between VLM and panel method will be investigated.

The simulations are executed with the same airfoil and settings as the previous experiments. This means that properties as β, κ, $C_{L\alpha}$, M, etc. are the same as calculated in 0.

Now, only one *AoA* ($\alpha = 10°$) is simulated.

Below, one theoretical calculation is done, so the reader can easily get how those values are gathered. Case 2, for an $A = 10$ is taken as an example. The theoretical lift coefficient C_L is calculated by using (5.6) and multiplying by the *AoA*.

$$C_L = \frac{2\pi \cdot A}{2 + \sqrt{\frac{A^2 \cdot \beta^2}{\kappa^2}\left(1 + \frac{\tan^2(\varphi_{50})}{\beta^2}\right) + 4}} \cdot \alpha$$

$$C_L = \frac{2\pi \cdot 10}{2 + \sqrt{\frac{10^2 \cdot 0.9798^2}{0.9744^2}\left(1 + \frac{\tan^2(0°)}{0.9798^2}\right) + 4}} \cdot 10°$$

$$C_L = 0.89503$$

With (6.4)

$$f(\lambda) = 0.0524 \cdot \lambda^4 - 0.15 \cdot \lambda^3 + 0.1659 \cdot \lambda^2 - 0.0706 \cdot \lambda + 0.0119$$
$$f(0.357) = 0.0524 \cdot 0.357^4 - 0.15 \cdot 0.357^3 + 0.1659 \cdot 0.357^2 - 0.0706 \cdot 0.357 + 0.0119$$
$$f(0.357) = 0.001866 \quad .$$

Using this, the theoretical Oswald factor can be calculated by filling in (6.3).

$$e_{theo} = \frac{1}{1 + f(\lambda) \cdot A} \quad,$$

$$e_{theo} = \frac{1}{1 + 0.001866 \cdot 10} \quad,$$

$$e_{theo} = 0.98168 \quad .$$

Now, every quantity is known to calculate $C_{D,i}$. This is done by using (6.2).

$$C_{D,i} = \frac{C_L{}^2}{\pi \cdot A \cdot e} \quad ,$$

$$C_{D,i} = \frac{0.89503^2}{\pi \cdot 10 \cdot 0.98168} \quad ,$$

$$C_{D,i} = 0.02598 \quad .$$

So far for the theoretical calculation. To compare the Hoerner curves, $f(\lambda)$ will be calculated out of the simulation results using (6.5). For current simulation, the simulation result for e is equal to 0.96573. Using this in (6.5) gives

$$f(\lambda) = \frac{1 - e_{theo}}{e_{theo} \cdot A} \quad ,$$

$$f(\lambda) = \frac{1 - 0.96573}{0.96573 \cdot 10} \quad ,$$

$$f(\lambda) = 0.003549 \quad .$$

For every simulation e, $C_{D,I}$, C_L, and $f(\lambda)$ are compared with the theoretical value by calculating the percentage deviation as in (5.19).

6.3   Results

First, the results of every case when using VLM are compared with values calculated with theoretical formulas. Afterwards, the same is done with the results gained by using the panel method. In the end, for some cases, the results of VLM and panel method are compared to one another.

For the first and second case, four graphs are made. The aspect ratio covers the horizontal axis, where respectively the Oswald factor, induced drag coefficient, lift coefficient, or $f(\lambda)$ cover the vertical axis.

From case 3 to 9, each time the Hoerner curve is created with theoretical values by (Niţă 2012) as well as with the simulation results gained by using respectively VLM or panel method.

6.3.1 VLM

The numerical values for every case can be found in Appendix A – Results for Hoerner's Curve When Using the VLM.

Case 1

For the first case, VLM seems to provide good results when looking at the Oswald efficiency (Figure 6.2). Generally, the form of the curve made by the simulation results follows the theoretical one. Nevertheless, the deviation between both values seem to grow with growing aspect ratio. With a maximum error of 7.59%, this is still between reasonable measures.

When looking at C_{Di} (Figure 6.3) , the error between simulated and theoretical value is bigger than when analizing e. With a minimal error of 6.11% and a maximum error of -16.19%, there is something to keep an eye on. Nevertheless, the simulated curve follows the form or the one prescripted by theory, which is still satisfying.
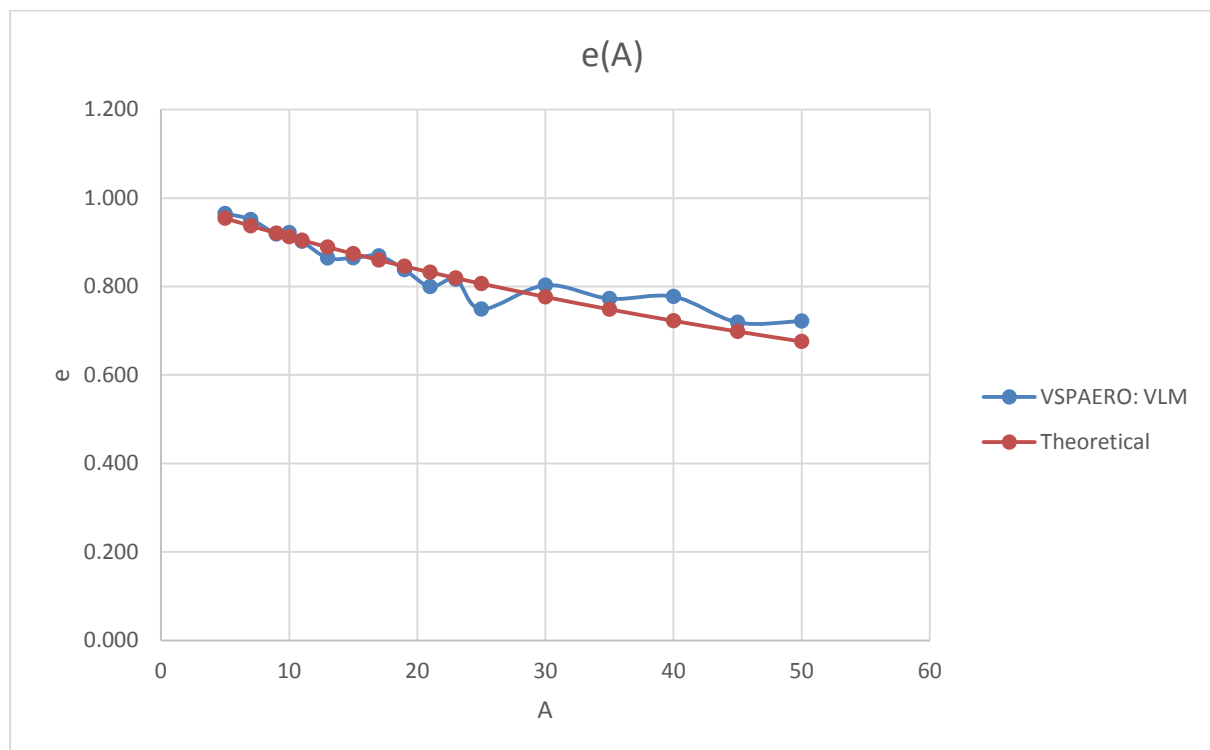
Figure 6.2   Plot showing relationship between Oswald efficiency factor and aspect ratio for Case 1. One is based on results gained from VSPAERO: VLM, another on theoretical formulas.
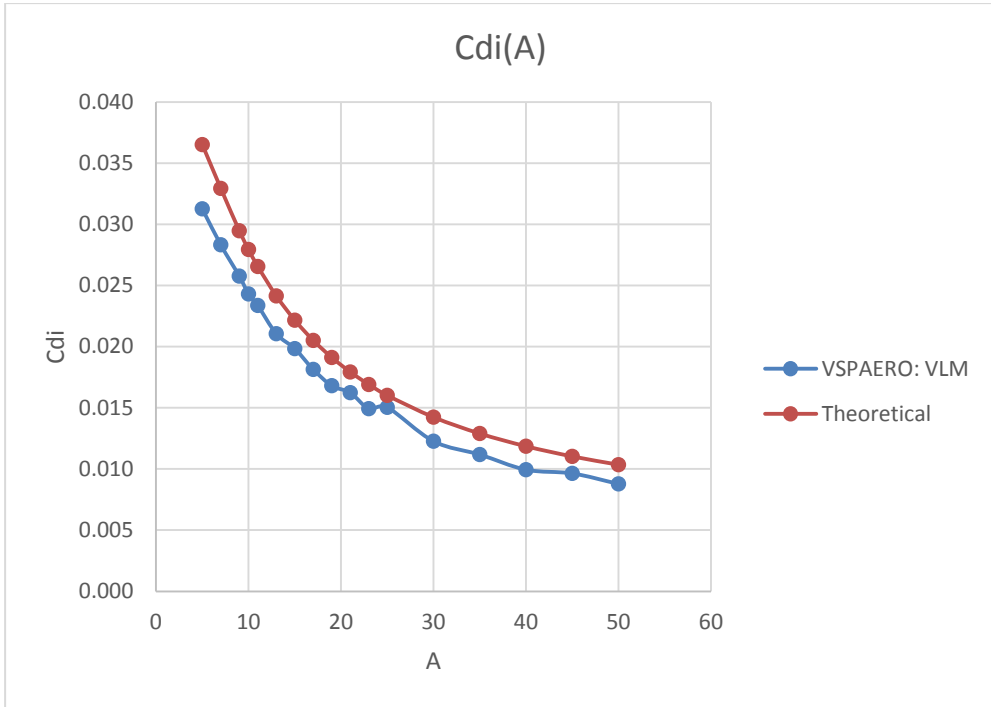
Figure 6.3   Plot showing relationship between induced drag and aspect ratio for Case 1. One is based on results gained from VSPAERO: VLM, another on theoretical formulas.

Figure 6.4 shows the relationship between lift coefficient C_L and aspect ratio. Again, the curve formed by the simulated values follows the theoretical one very nicely. The minimal error is equal to -4.81%, where the biggest error equals -6.81%. Therefore, it can be stated that this values are more correct than when looking at the induced drag coefficient, shown in Figure 6.3.
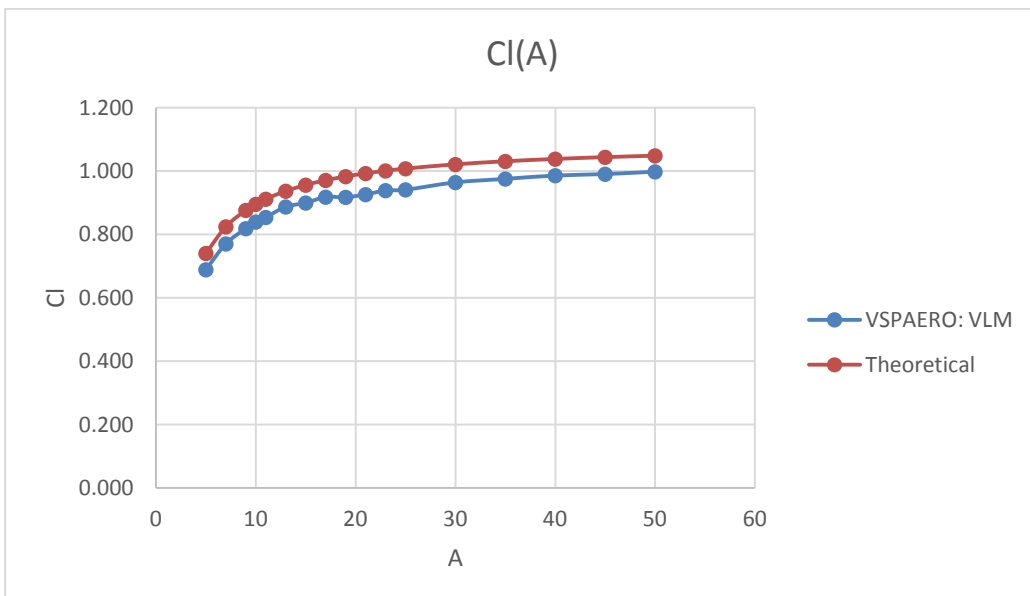
Figure 6.4   Plot showing relationship between lift and aspect ratio for Case 1. One is based on results gained from VSPAERO: VLM, another on theoretical formulas.

The last graph of this case is the one which shows the relationship between $f(\lambda)$ and aspect ratio, shown by Figure 6.5. Here, the values gathered by the simulation results fluctuates very strongly. A maximum positive error of +39.67% and a maximum negative error equal to -25.42% shows that these results are not as reliable as the ones before. This due to the way the simulation value of $f(\lambda)$ is calculated, see (6.5). Remember that this is done by using the outcome of e_{theo}. This means that also the corresponding error is taken into this calculation. Also, the theoretical value cannot be seen as completely correct. Equation (6.4) stated by (Niţă 2012) consists of rounded factors and will therefore not give the exact values.
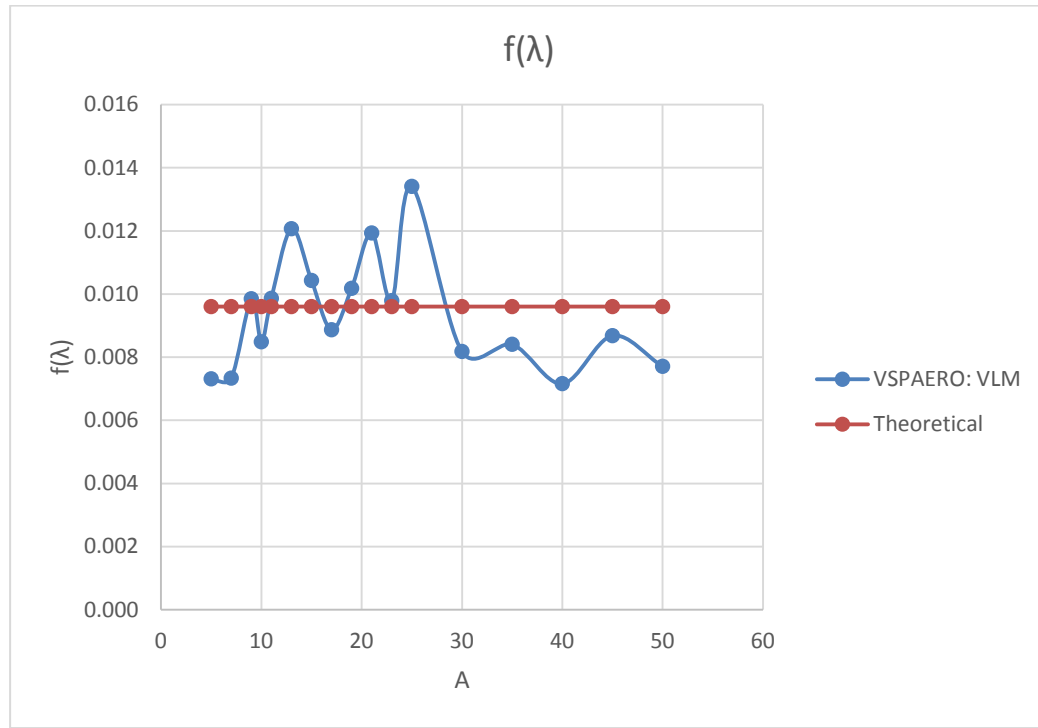
Figure 6.5   Plot showing relationship between f(λ) and aspect ratio for Case 1. One is based on results gained from VSPAERO: VLM, another on theoretical formulas.

Case 2

Immediately there's a remarkable difference visible between the result for the Oswald factor between Case 1 and Case 2. The relationship between the Oswald factor and aspect ratio for an optimal tapered wing, remember $\lambda_{opt} = 0.357$ is shown in Figure 6.6.

At first, it seems that for growing aspect ratio, the simulated value gets closer and closer to the theoretical one. Until, at around an estimated aspect ratio equal to 38, the simulated curve crosses the theoretical one. From then on, there's an overestimation of the Oswald factor which only seems to keep increasing with continued growing of the aspect ratio. Eventhough this remarkability, the errors are still considerably small. The maximum error is equal to -1.75%, which is noticeably smaller than at Case 1.

Looking at the second curve created by the results of Case 2 (Figure 6.7), it seems that the simulation result for C_{Di} for is very close to the theoretical value for every aspect ratio, because the two curves almost fall over each other, especially with growing aspect ratio.

At first thought, the reader might think therefore the error will be very little. However, the maximum error here, is equal to -7.58%, which is remarkably greater than the plot of the Oswlald factor. This confirms that the reader always has to pay attention to the relative scales at the axes.

For the plot showing the relationship between the lift coefficient and aspect ratio (Figure 6.8), the same remarks can be made as for the induced drag factor (Figure 6.7). The curve build by the simulation results almost follows the shape of the theoretical one perfectly. A maximum error of -4.62% confirms that these results too, are reliable and sufficient.

The last plot of the first group of cases is made visual in Figure 6.9 which shows the relationship between $f(\lambda)$ and aspect ratio. First, it seems to be that the simulation curve asymptotically gets closer to the constant theoretical one. Because the simulated values are calculated by the simulation results for e, the same crossing between the two curves occurs and the deviation only increases with growing aspect ratio.

All in all, the first two cases produce reliable results given by VLM. In the upcoming cases, the aspect ratio is kept constant and the taper ratio λ will vary from 0 to 1.
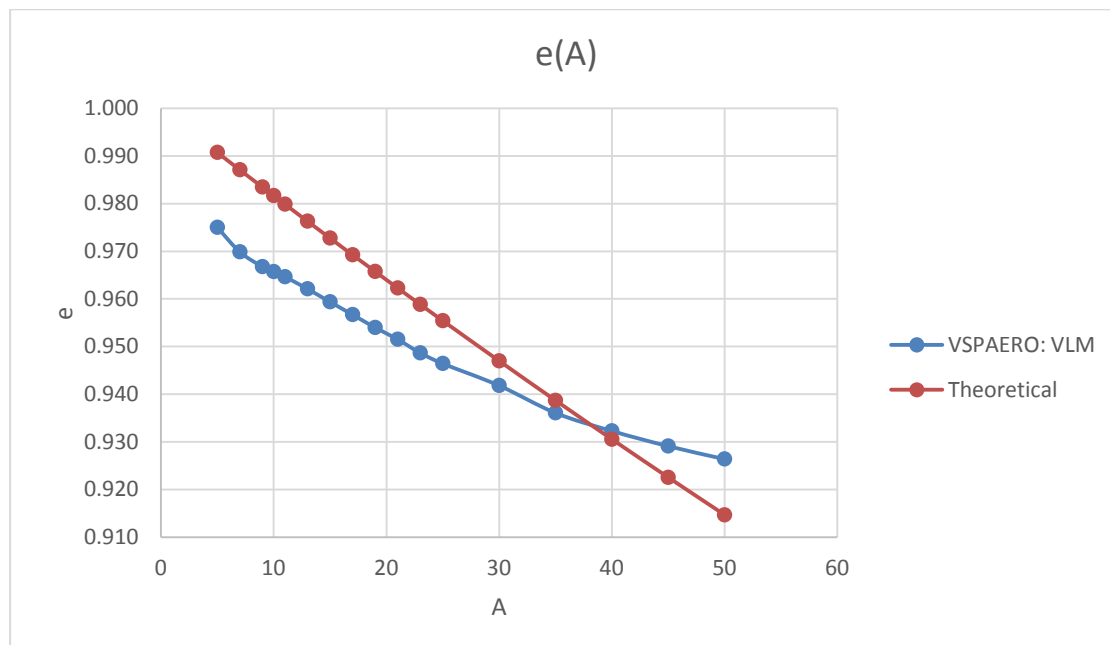
Figure 6.6   Plot showing relationship between Oswald efficiency factor and aspect ratio for Case 2. One is based on results gained from VSPAERO: VLM, another on theoretical formulas.
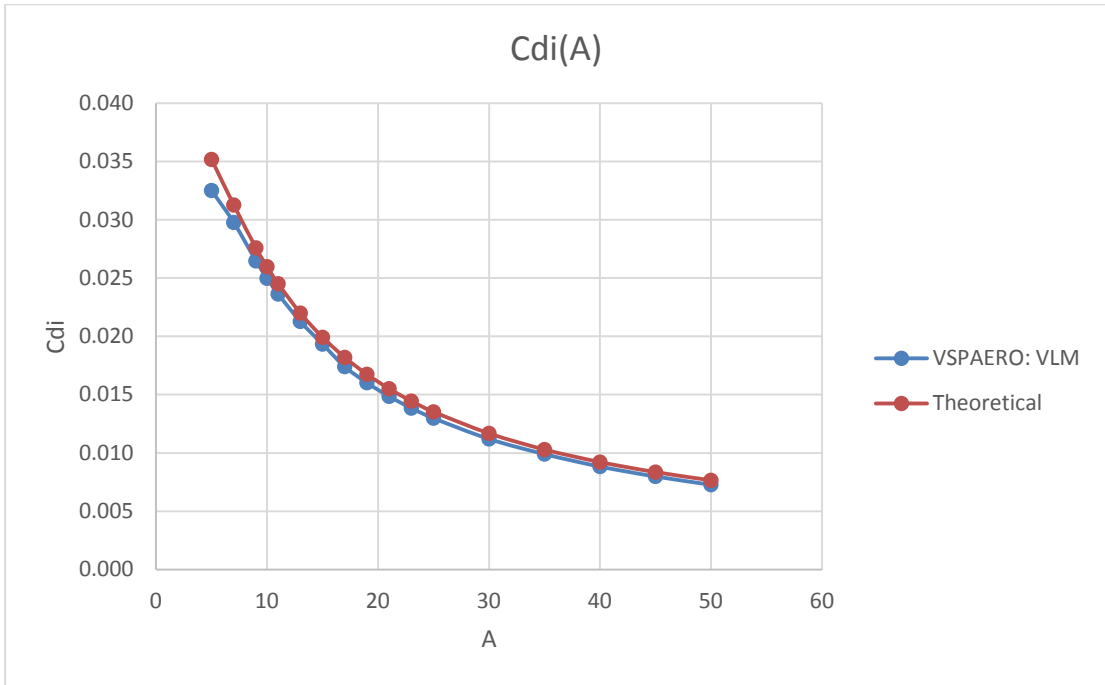
Figure 6.7 Plot showing relationship between induced drag and aspect ratio for Case 2. One is based on results gained from VSPAERO: VLM, another on theoretical formulas.
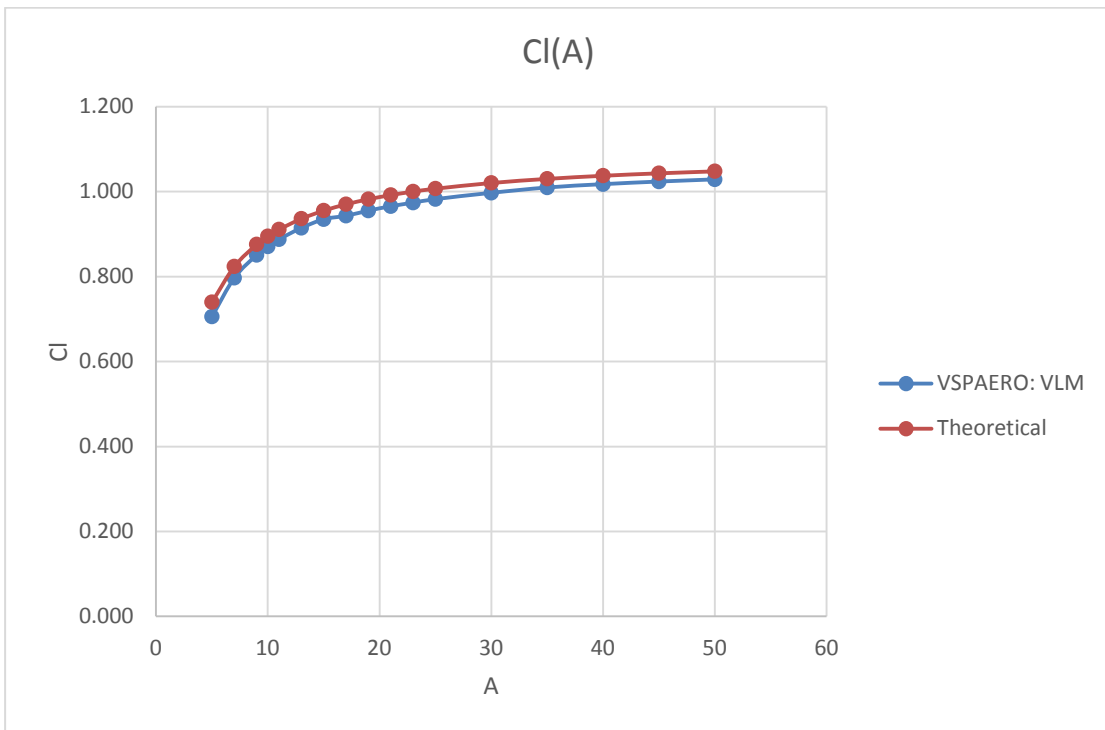
Figure 6.8 Plot showing relationship between lift and aspect ratio for Case 2. One is based on results gained from VSPAERO: VLM, another on theoretical formulas.
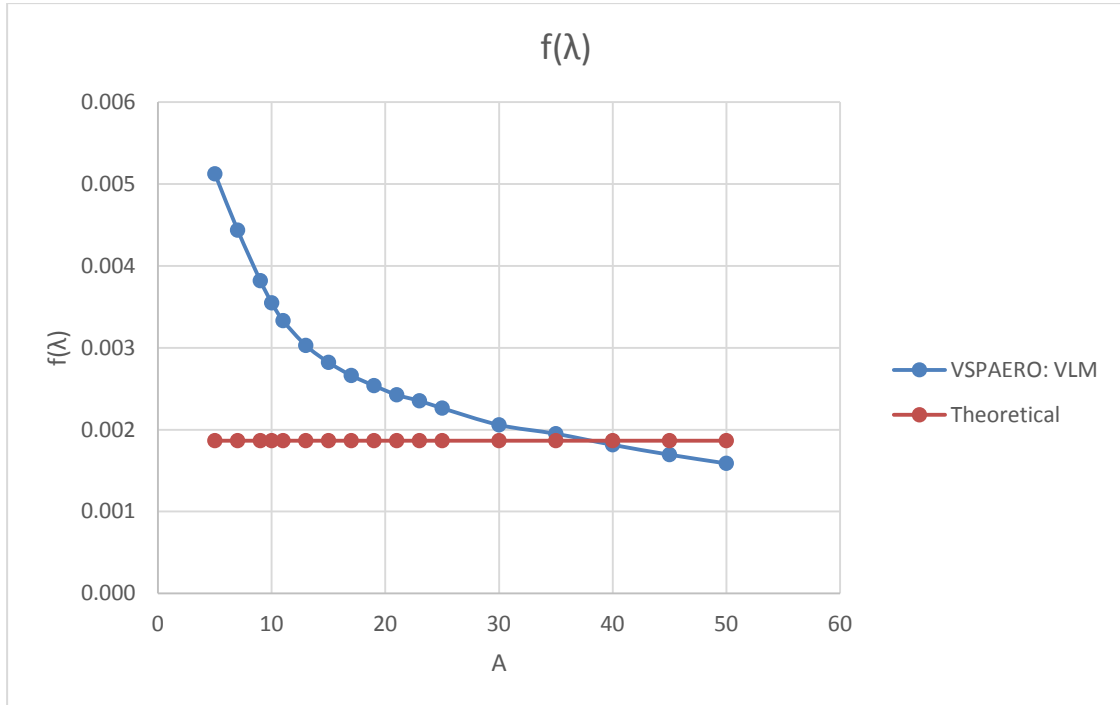
Figure 6.9   Plot showing relationship between f(λ) and aspect ratio for Case 2. One is based on results gained from VSPAERO: VLM, another on theoretical formulas.

Case 3

This case covers the simulation of a wing with constant aspect ratio, A is equal to 5, and varying taper ratio λ (Figure 6.10). Immediately, the first simulation point ($\lambda = 0$) stands out. In this particular point, the tip chord is zero, so the wing goes from a three-dimensional profile to a one-dimensional point. It is assumed this has numerical errors as a consequence as an explanation of the big error occurring here. Still, in general, the curve formed by the simulation results follows the form of the theoretical Hoerner curve with, exept for $\lambda = 0$, a constant underestimation of $f(\lambda)$, or better, an overestimation of the Oswald factor. Also, The minimum value of the simulation results for $f(\lambda)$ occurs at $\lambda = 0.357$, which is correct as stated by (Niţă 2012).
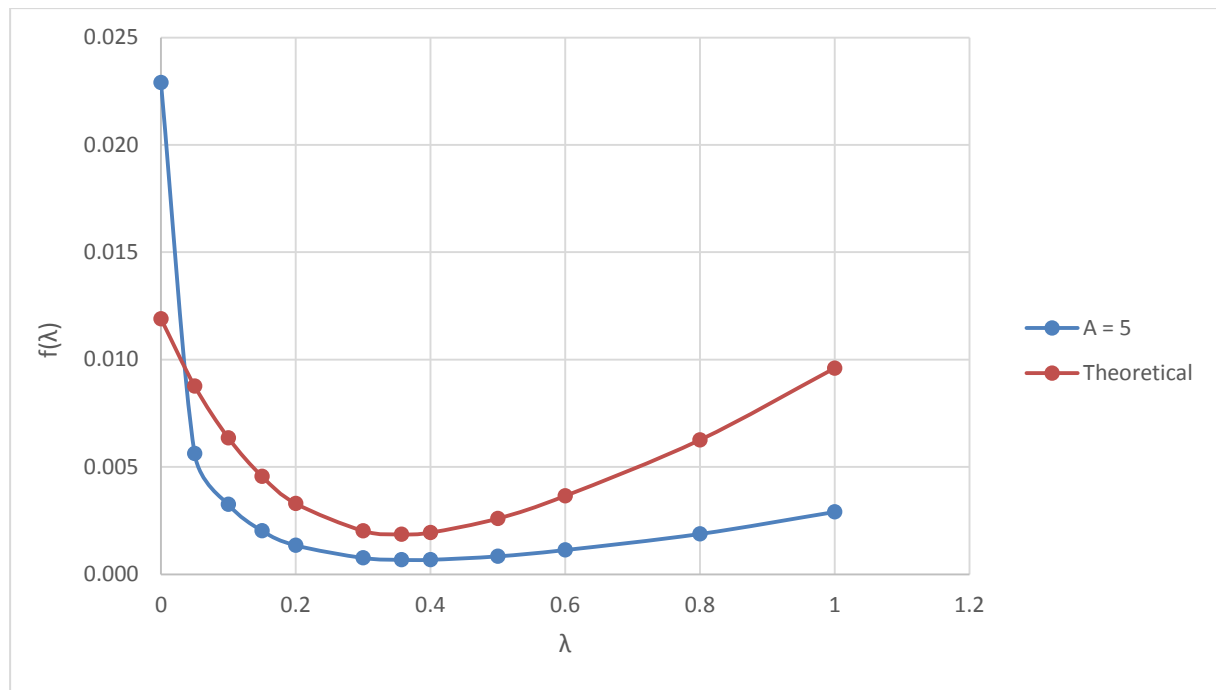
Figure 6.10   Plot showing relationship between function f(λ) and taper ratio for Case 3. One is based on results from VSPAERO: VLM, the other is based on theoretical formulas.

Case 4

The fourth case, shown in Figure 6.11, has the same problem with the first simulation point as Case 3. Also, the minimum value of the simulation results for f(λ) occurs at $\lambda = 0.4$, which is not correct according to (Niţă 2012). Apart from that, the curve formed by the simulation results follows the theoretical one a lot closer than when looking at Case 3, especially for lower taper ratio's. When λ gets closer to one, the deviation between theoretical value and simulation value starts to grow again.
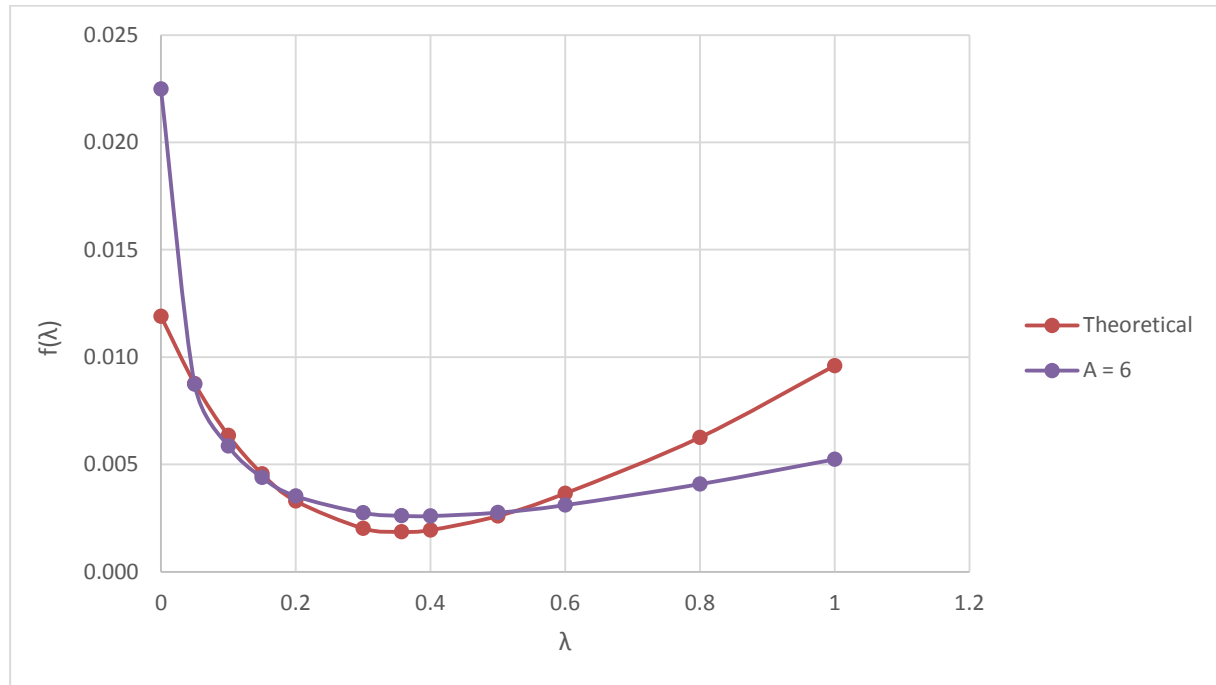
Figure 6.11   Plot showing relationship between function f(λ) and taper ratio for Case 4. One is based on results from VSPAERO: VLM, the other is based on theoretical formulas.

Case 5

Figure 6.12 shows the relationship between the simulation values for Case 5, compared to the theoretical Hoerner curve. Again, the same simulation error occurs at $\lambda = 0$. Another thing to notice is that there's only one crossing point between both curves, just after $\lambda = 0.6$. It speaks for itself that before this point, there's an underestimation of the Oswald factor and behind, there's an overestimation of the Oswald factor.
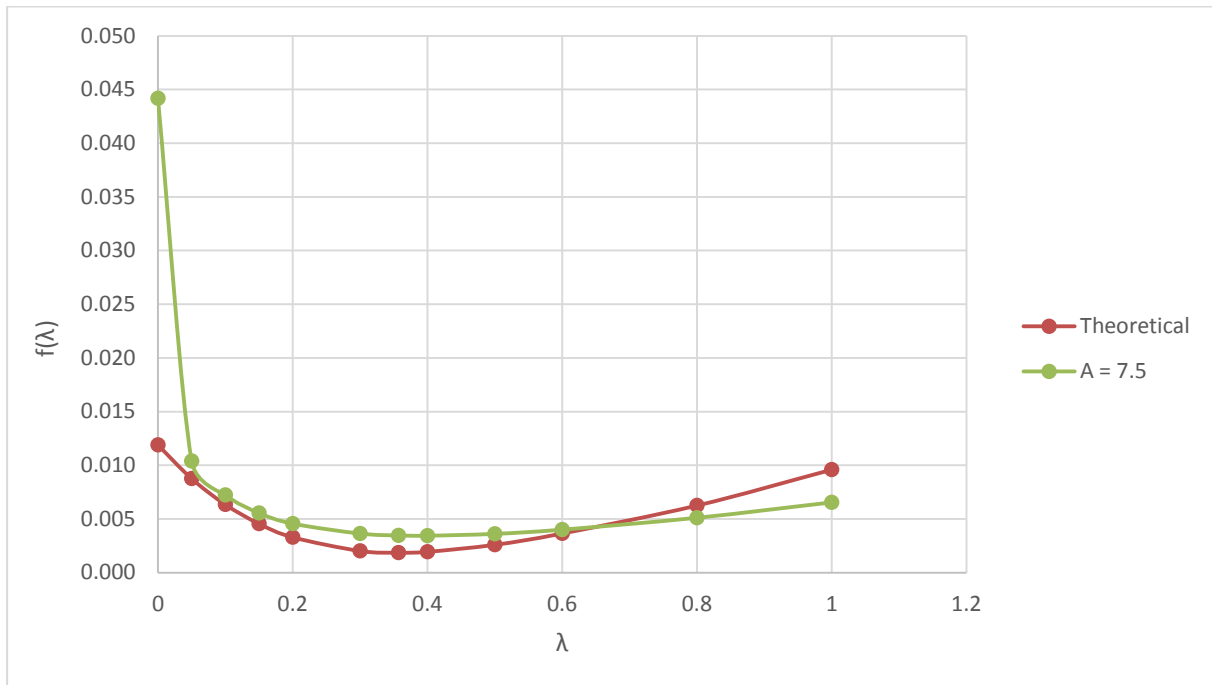
Figure 6.12   Plot showing relationship between function f(λ) and taper ratio for Case 5. One is based on results from VSPAERO: VLM, the other is based on theoretical formulas.

Case 6

Next up is Case 6, made visual by Figure 6.13. Generally, the same conclusions as before can be made. The simulated curve follows the form of the theoretical one well, with one crossing point between both. Nevertheless, this crossing point is replaced to $\lambda = 0.85$ approximately. Also, the error at simulation point $\lambda = 0$ seems to get smaller compared to the results from cases with lower aspect ratio. Again, the minimum value of the simulation results for $f(\lambda)$ occurs at $\lambda = 0.4$, which is something to keep in mind for next cases.
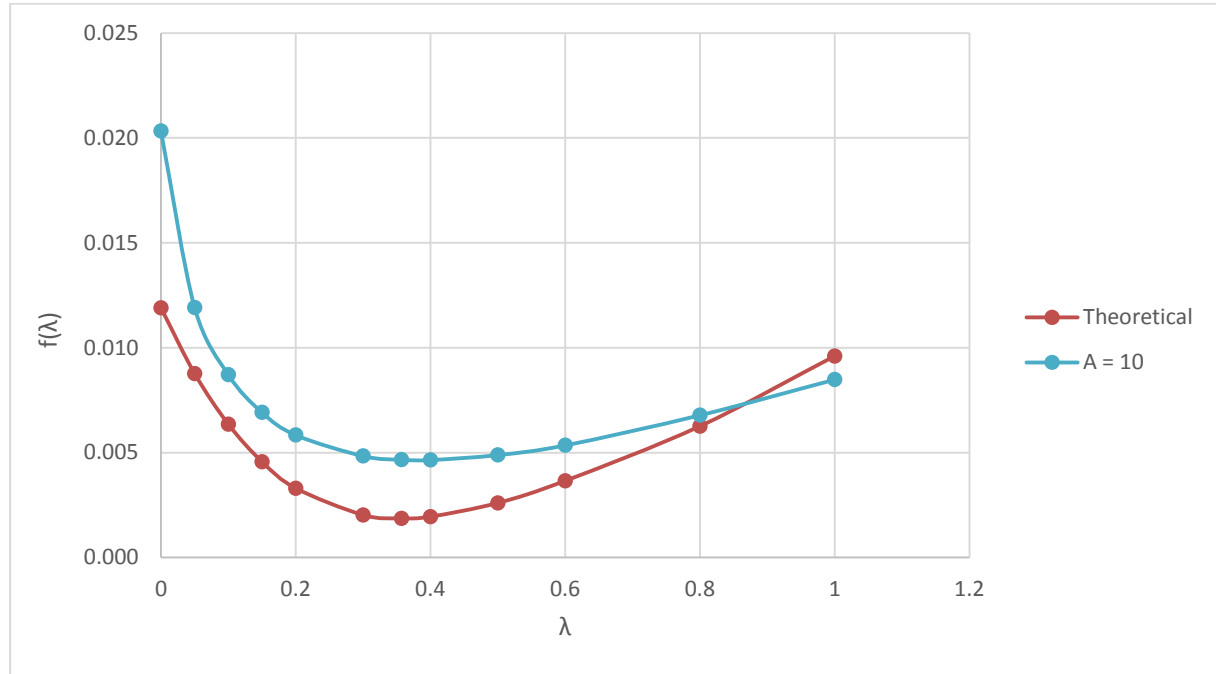
Figure 6.13   Plot showing relationship between function f(λ) and taper ratio for Case 6. One is based on results from VSPAERO: VLM, the other is based on theoretical formulas.

Case 7

The next examinated aspect ratio equals 20 (Figure 6.14). Again, the same conclusions can be made as for e.g. Case 6. The crossing point between theoretical and simulated curve stays at approximately the same λ, with an overestimation before, and an underestimation behind. In the mean time, the error for $\lambda = 0$ keeps getting smaller, which is a satisfying development. Also, the value of the simulation results for $f(\lambda)$ now takes place at $\lambda = 0.357$, which is considered as more correct.
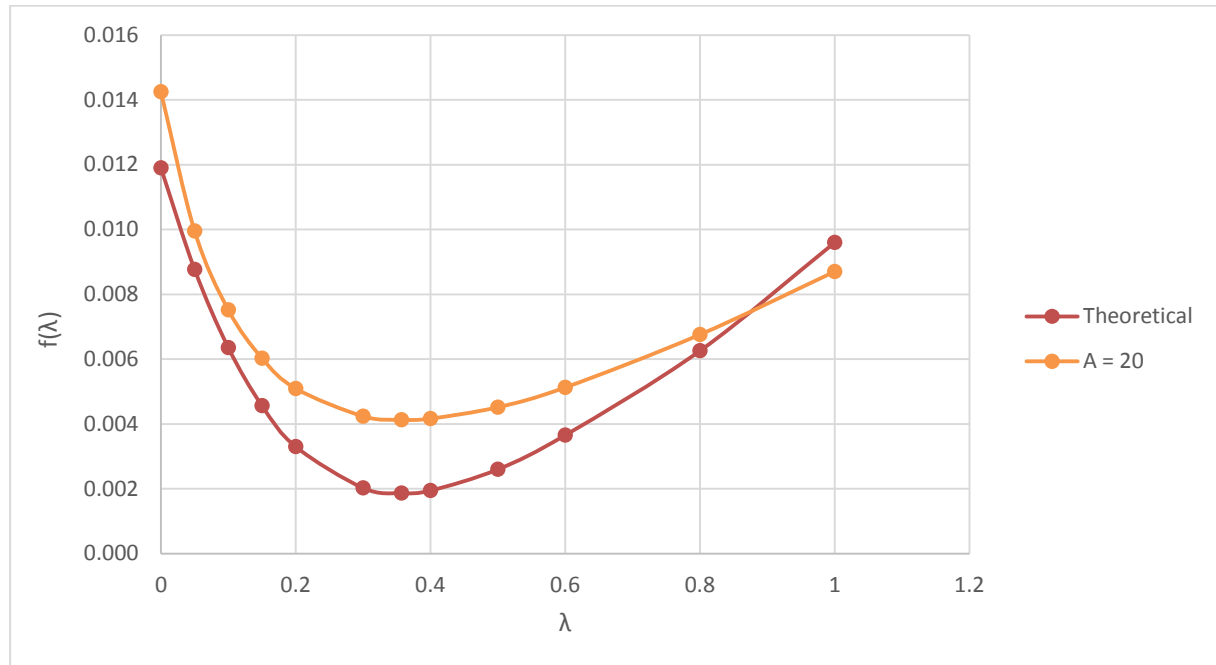
Figure 6.14   Plot showing relationship between function f(λ) and taper ratio for Case 7. One is based on results from VSPAERO: VLM, the other is based on theoretical formulas.

Case 8

Looking at Figure 6.15, it can be concluded that the error which kept occurring at $\lambda = 0$ is gone. There now even is a little underestimation of $f(\lambda)$ compared to the theoretical value. Also, there are two crossing points between both curves. One at λ between 0.1 and 0.15 and a second at approximately $\lambda = 0.8$. Before the first, there's an overestimation of the Oswald factor, between both this changes to an underestimation and obviously again an overestimation behind the second crossing point.
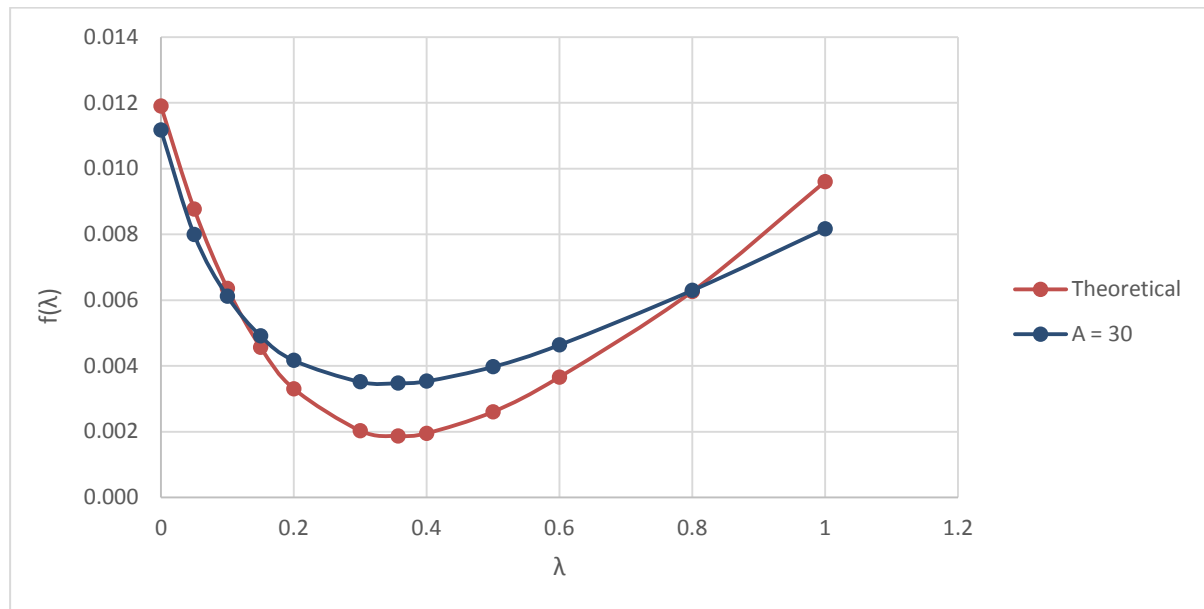
Figure 6.15   Plot showing relationship between function f(λ) and taper ratio for Case 8. One is based on results from VSPAERO: VLM, the other is based on theoretical formulas.

Case 9

The last case is made visual by Figure 6.16, and quickly, the same conclusions as for Case 8 can be made. Two crossing points, with an overestimation of the Oswald factor before the first, an underestimation between both, and again an overestimation after the second. Note that those crossing points replace themselves to approx. $\lambda = 0.2$ and $\lambda = 0.65$ respectively.
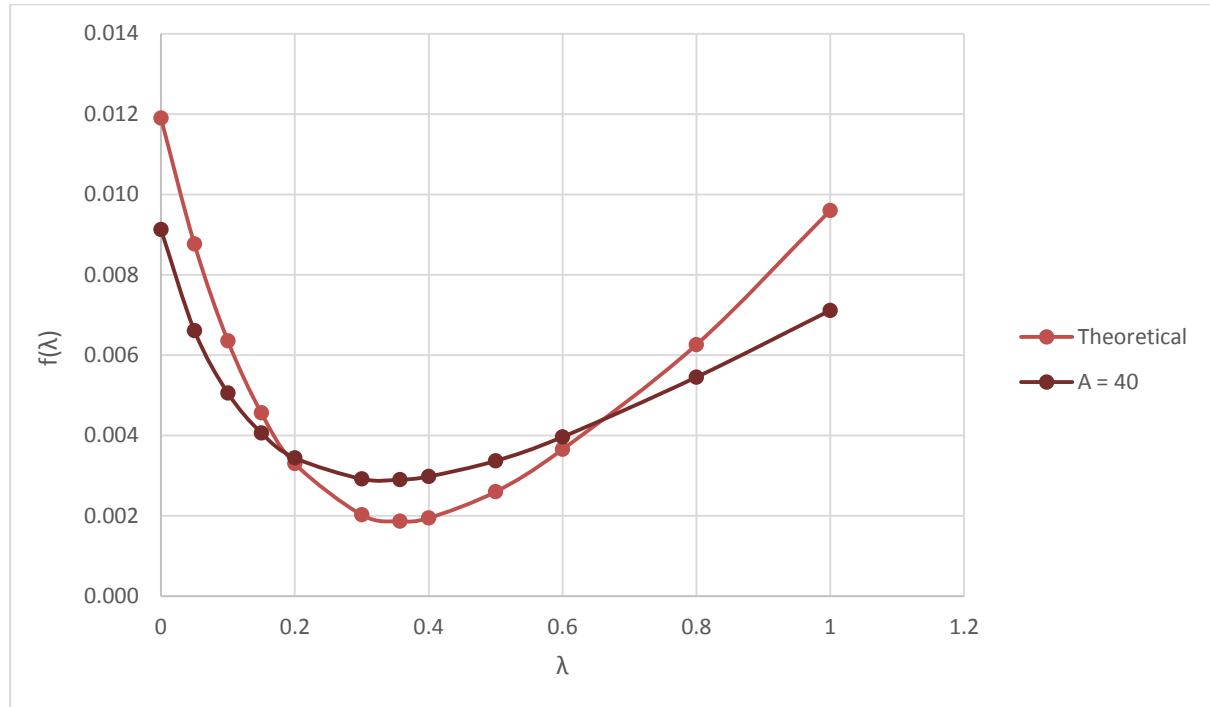
Figure 6.16   Plot showing relationship between function f(λ) and taper ratio for Case 9. One is based on results from VSPAERO: VLM, the other is based on theoretical formulas.

Summary for VLM

All in all, during this experiment, VSPAERO delivers good results when using VLM. The simulated curves always follow the form prescripted by the theoretical curve. It can be observed that for aspect ratio between 10 and 40 the minimum of the curves decreases steadily and comes closer to the minimum of Hoerner's curve (see Figure A.1). Across all aspect ratios (5 to 40) the VLM curves $f(\lambda, A)$ show a less unified picture (see Figure A.2).

6.3.2 Panel Method

The numerical values for every case can be found in Appendix B – Results for Hoerner's Curve When Using the Panel Method.

Case 1

For the first case, using panel method seems to provide good results when looking at the Oswald efficiency (Figure 6.17). Generally, the form of the curve made by the simulation results gets closer to the theoretical one with growing aspect ratio. The maximum error equals -11.77% at $A = 9$, and jumps to a minimum of -0.05% for $A = 50$. This can be explained as followed: By always increasing it's aspect ratio, the simulation model always gets closer to the infinite wing, where the theoritacal calculation are based on. Therefore, is is expected that the panel method will give the most correct values at the biggest aspect ratio's.

When looking at C_{Di} (Figure 6.18) , the error between simulated and theoretical value is in the same order as when looking at e. With a minimal error of -2.44% and a maximum error equal to -9.26%, these results can be seen as reliable. Also, the simulated curve follows the form or the one prescripted by theory, which is satisfying.

Figure 6.19 shows the relationship between lift coefficient CL and aspect ratio. Again, the curve formed by the simulation results follows the theoretical one very nicely. The minimal error is equal to −3.86%, while the biggest error equals -10.14%. Therefore, it can be stated that this values are equally correct as when looking at results for the induced drag coefficient (Figure 6.18).
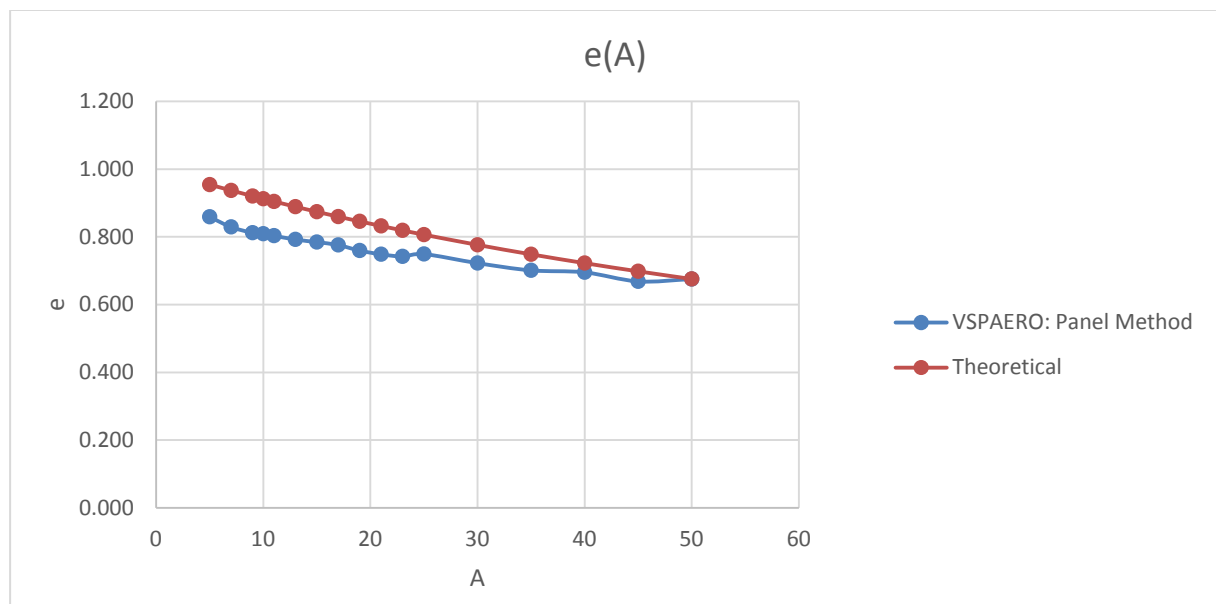
Figure 6.17 Plot showing relationship between Oswald efficiency factor and aspect ratio for Case 1. One is based on results gained from VSPAERO: Panel Method, another on theoretical formulas.
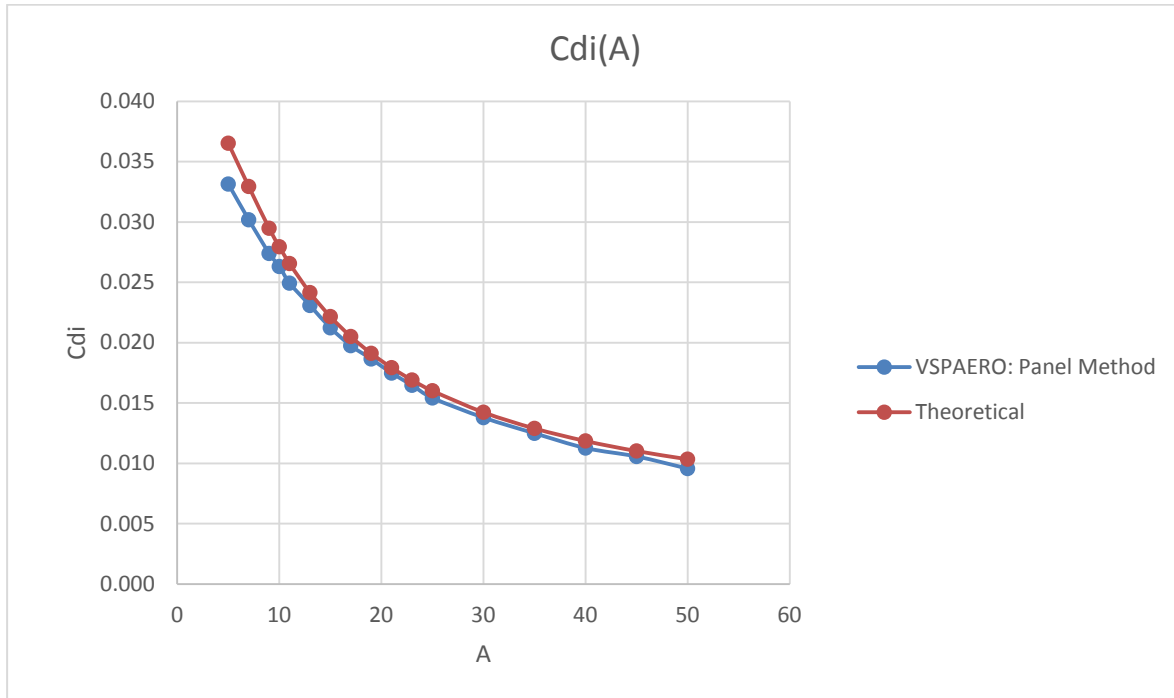
Figure 6.18 Plot showing relationship between induced drag and aspect ratio for Case 1. One is based on results gained from VSPAERO: Panel Method, another on theoretical formulas.
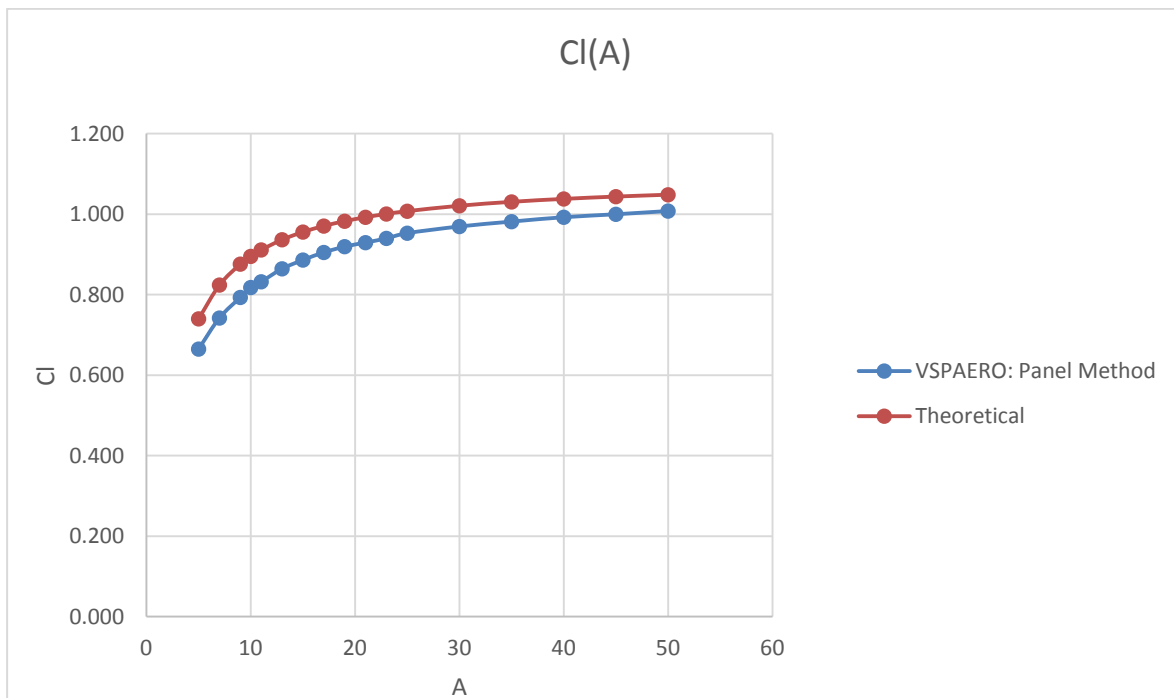
Figure 6.19 Plot showing relationship between lift and aspect ratio for Case 1. One is based on results gained from VSPAERO: Panel Method, another on theoretical formulas.
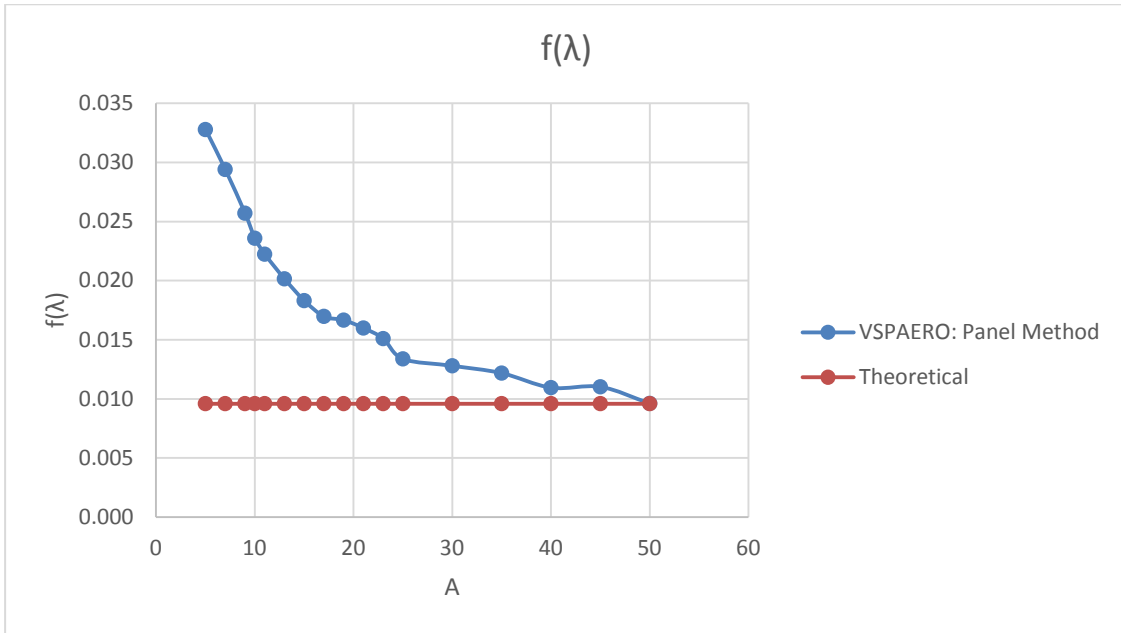
Figure 6.20   Plot showing relationship between f(λ) and aspect ratio for Case 1. One is based on results gained from VSPAERO: Panel Method, another on theoretical formulas.

The relationship between f(λ) and aspect ratio is shown in the last graph of Case 1. Figure 6.20 shows that for growing aspect ratio, the simulation result gets closer and closer to the theoretical value equal to 0.0096, as expected. First, this seems to happen asymptotically, but with very big aspect ratio's, there are bigger jumps in the curve. This can be because the number of panels in the simulation grows very fast and therefore the simulation will ask more computational power, with the risk of numerical errors as a consequence. Nevertheless, the error keeps dropping, which is satisfying.

Case 2

All numerical values of the simulation of Case 2 when using panel method, can be found in Table B.2.

Figure 6.21 shows a continuous underestimation of the Oswald factor compared to the theoretical value. The error varies between -16.58% and -10.53%. Again, this error declines with growing aspect ratio. Also, there are no unexpected jumps or whatsoever in the simulation results. Therefore, these results are seen as reliable and sufficient.

That last statement is repeated when looking at Figure 6.22, which shows the relationship between induced drag and aspect ratio for current case. Again, the simulation curve follows the theoretical one almost identically. Looking at the error between both, it seems to be that the biggest errors occur in the middle part of the tested range. Nevertheless, these errors never exceed 9% and that's why also these results are accepted as reliable.

The same counts when looking at the plot showing the relationship between lift coefficient and aspect ratio (Figure 6.23). The theoretical curve is set and the simulated curve follows almost perfectly, with a constant underestimation. This error again drops when increasing the aspect ratio (from -8.84% at $A = 5$ to -2.47% at $A = 50$). This order of error is very small and therefore these results are accepted as reliable.

The relationship between $f(\lambda)$ and aspect ratio is shown in the last graph of Case 2, while using panel method. Figure 6.24 shows that for growing aspect ratio, the simulation result gets closer and closer to the theoretical value equal to 0.0096, as expected. This seems to happen asymptotically. It can be assumed that for even bigger aspect ratio's, the error between both will keep on dropping. Nevertheless minimum error here, is still in the order of 10^2 %. These errors are much bigger than simulations using AVL, done by (Budziak, 2015).
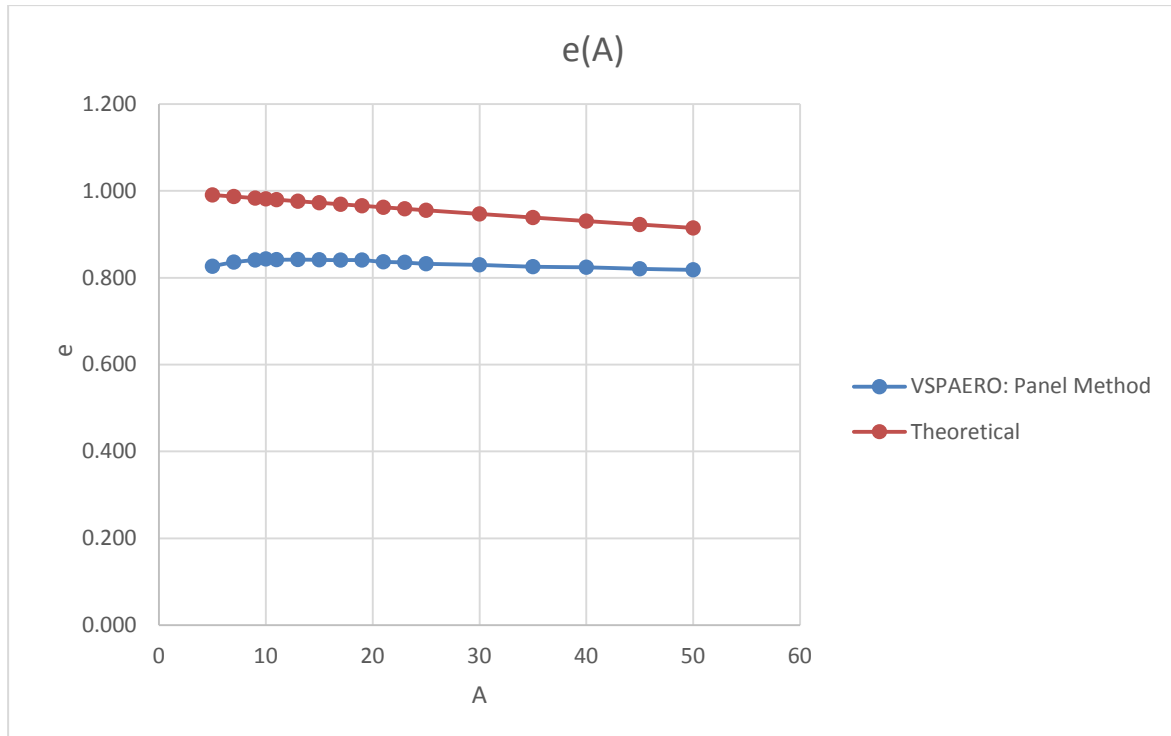
Figure 6.21   Plot showing relationship between Oswald efficiency factor and aspect ratio for Case 2. One is based on results gained from VSPAERO: Panel Method, another on theoretical formulas.
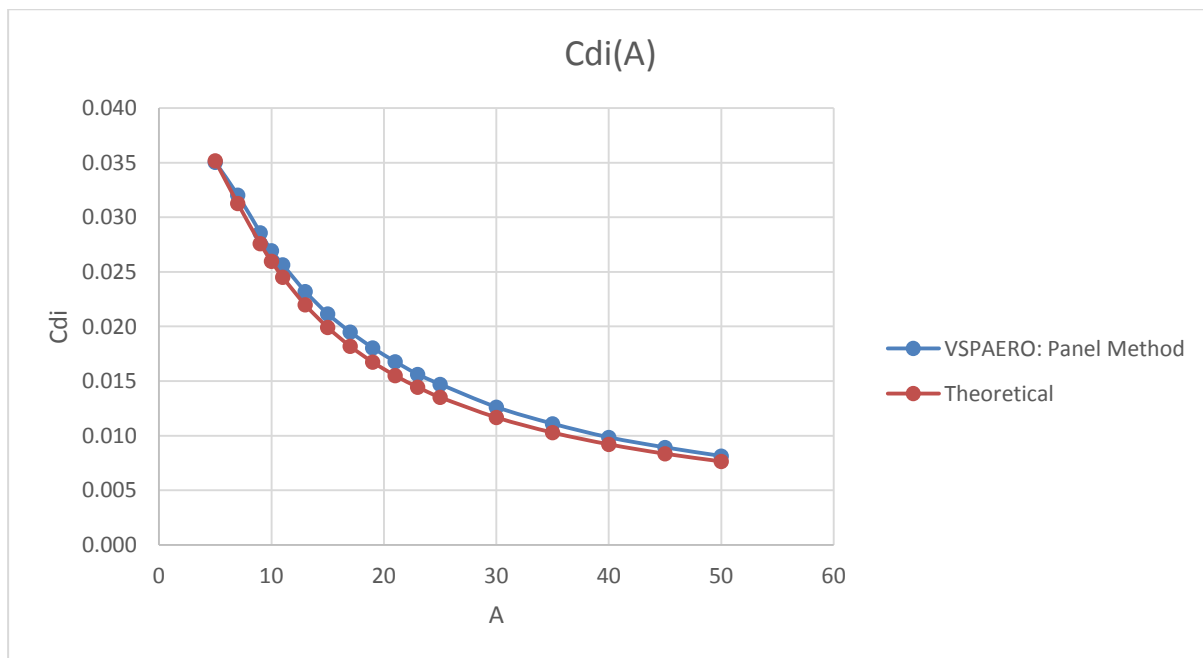
Figure 6.22   Plot showing relationship between induced drag and aspect ratio for Case 2. One is based on results gained from VSPAERO: Panel Method, another on theoretical formulas.
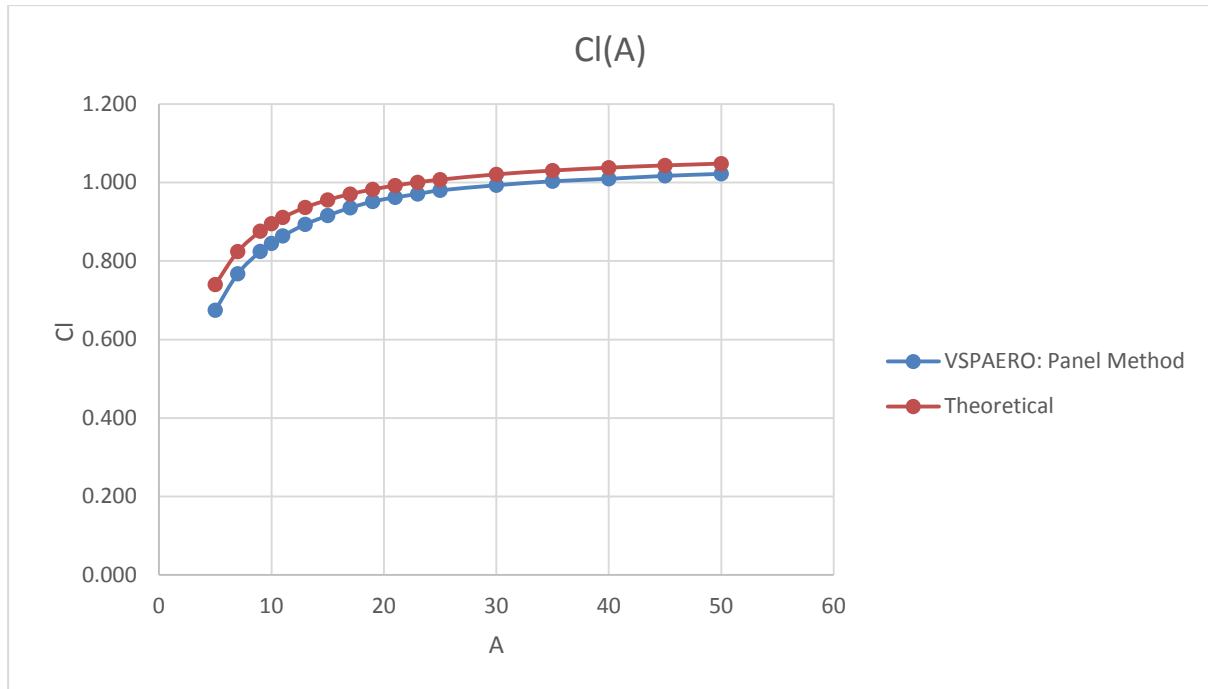
Figure 6.23 Plot showing relationship between lift and aspect ratio for Case 2. One is based on results gained from VSPAERO: Panel Method, another on theoretical formulas.
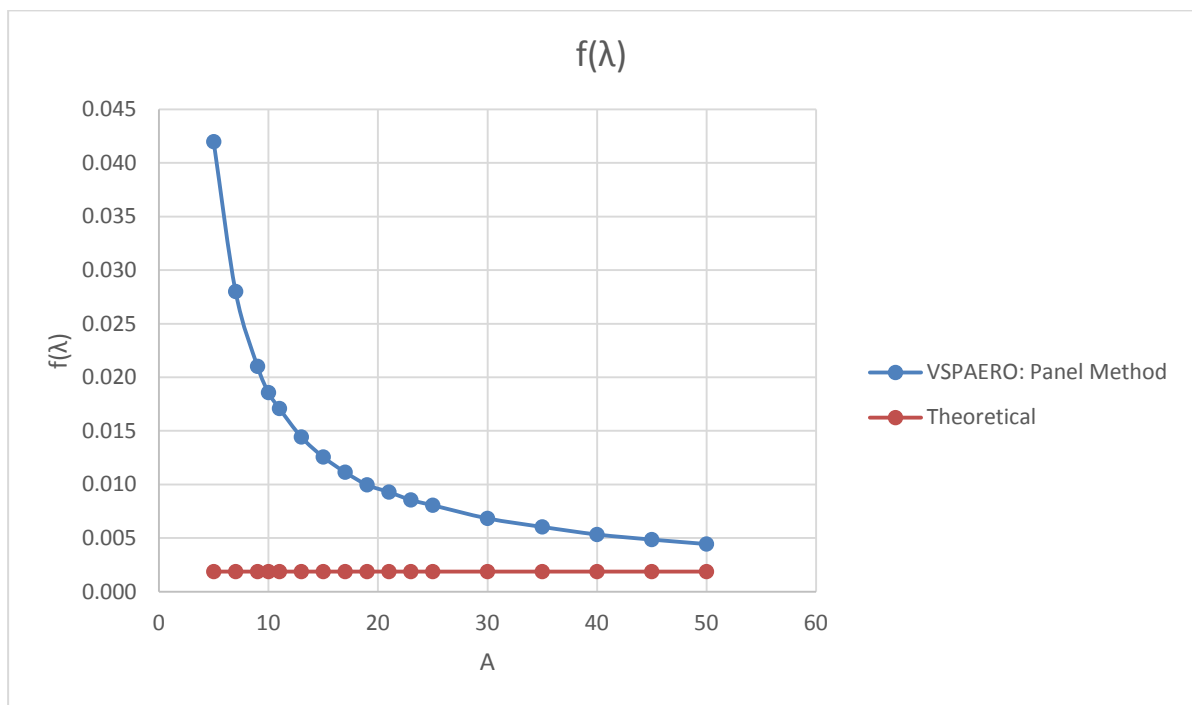
Figure 6.24 Plot showing relationship between f(λ) and aspect ratio for Case 2. One is based on results gained from VSPAERO: Panel Method, another on theoretical formulas.

Case 3 to 9

All results for Case 3 to 9 will be discussed together and are brought together in Figure 6.25. The numerical values for each case can be found in Table B.3 to Table B.9.

The results follow the expectation. By growing aspect ratio, the model always approaches the infinite wing more and more. This is clearly visible in Figure 6.25. The curve of the lowest aspect ratio ($A = 5$) can be found above all others, and the theoretical one below every other curve. The curve below a selected curve, will always be the one of the next aspect ratio. E.g. looking at the curve representing $A = 7.5$, the curve below represents the results of $A = 10$ and the curve above represents the results of $A = 6$.

Obviously, the simulation of Case 3 is the least reliable. Not only for the biggest deviation compared to the theoretical values, but also the curve these results make. It is clear to see that these results don't follow the form of the theoretical curve like the others all do. This can again be explained by the fact that the model used for these simulations are relatively more three-dimensional compared to the models used in the simulations for bigger aspect ratio's.
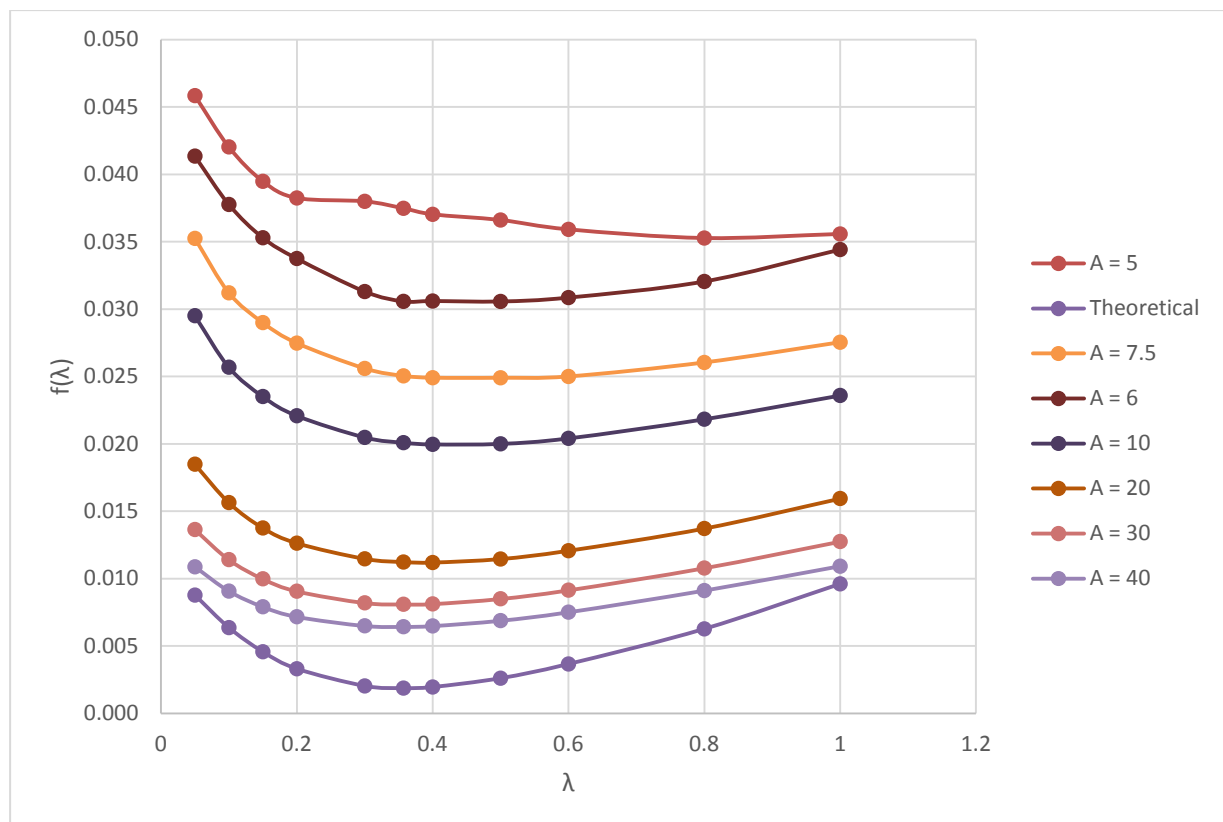
Figure 6.25   Function obtained from simulations done with VSPAERO: Panel method from Case 3 to 9. For comparison Hoerner's curve by Niţă (2012) is given. See also Figure B.1.

6.3.3 VLM vs Panel Method

This section covers a comparison between the results obtained by using VLM or Panel Method for Case 3 (Figure 6.26) and Case 9 (Figure 6.27). The results follow the form of the theoretical curve well, but it is clear to see that the results obtained by VLM are closer to Hoerner's theoretical curve than the results obtained by Panel Method.

Compare with Figure B.1, to understand that the theoretical span efficiency, e_{theo} is a function of aspect ratios and taper ratio λ, expressed with the parameter $f(\lambda)$ from the fundamental Equation (6.3). For e.g. $e_{theo} = 0.8$, a large aspect ratio, needs only a small $f(\lambda)$. In contrast a small aspect ratio, needs a large $f(\lambda)$. With Hoerner's curve quite high (near to 1) values for e_{theo} are calculated. If in contrast to Hoerner, the VLM or the panel method predict a lower span efficiency factor e (which is considered to be e_{theo}) this leads to $f(\lambda)$ calculated with (6.5) higher than the $f(\lambda)$ from Hoerner. The higher the aspect ratio, A the smaller $f(\lambda)$ calculated with (6.5). However, $f(\lambda)$ will not go to Hoerner's $f(\lambda)$ asymptotically with larger A, but can well fall under Hoerner's $f(\lambda)$.

This means that the correction should not be expected in $f(\lambda)$, but in a correction factor applied to the span efficiency factor, e_{theo} directly. Without comparable wind tunnel experiments, we do not know, if the VLM or the panel method yiel "correct" values.

$$e_{theo,VML} = e_{theo,Hoerner} \cdot k_{e,VML} \qquad (6.6)$$

and

$$e_{theo,panel} = e_{theo,Hoerner} \cdot k_{e,panel} \cdot \qquad (6.7)$$

Based on the post processing tables stored at Harvard Dataverse (see page 2), we get approximately
- $k_{e,VLM} = 0.98$ (valid for aspect ratios, $A \geq 10$) if the VLM is considered to yield "correct" results and
- $k_{e,panel} = 0.85$ (valid for aspect ratios, $A \geq 5$) if the panel method is considered to yield "correct" results.
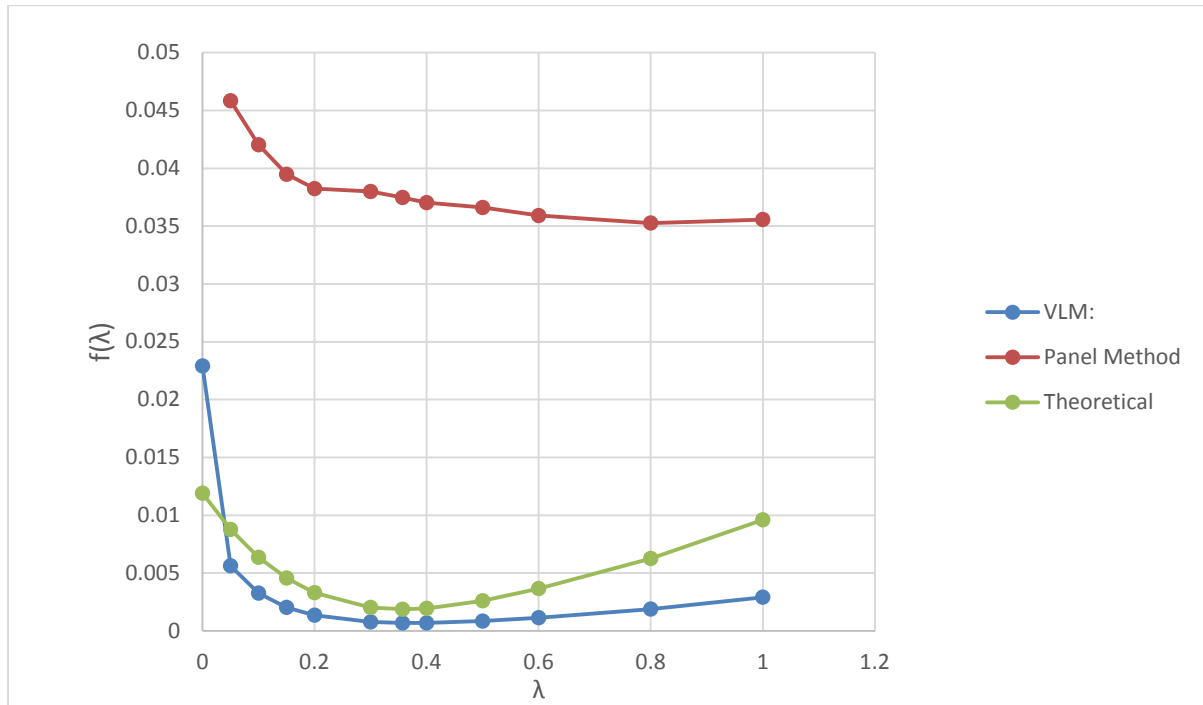
Figure 6.26   Plots showing the relation between f(λ) and taper ratio for results obtained by using VSPAERO: VLM compared with VSPAERO: Panel Method and with theoretical formulas for Case 1.
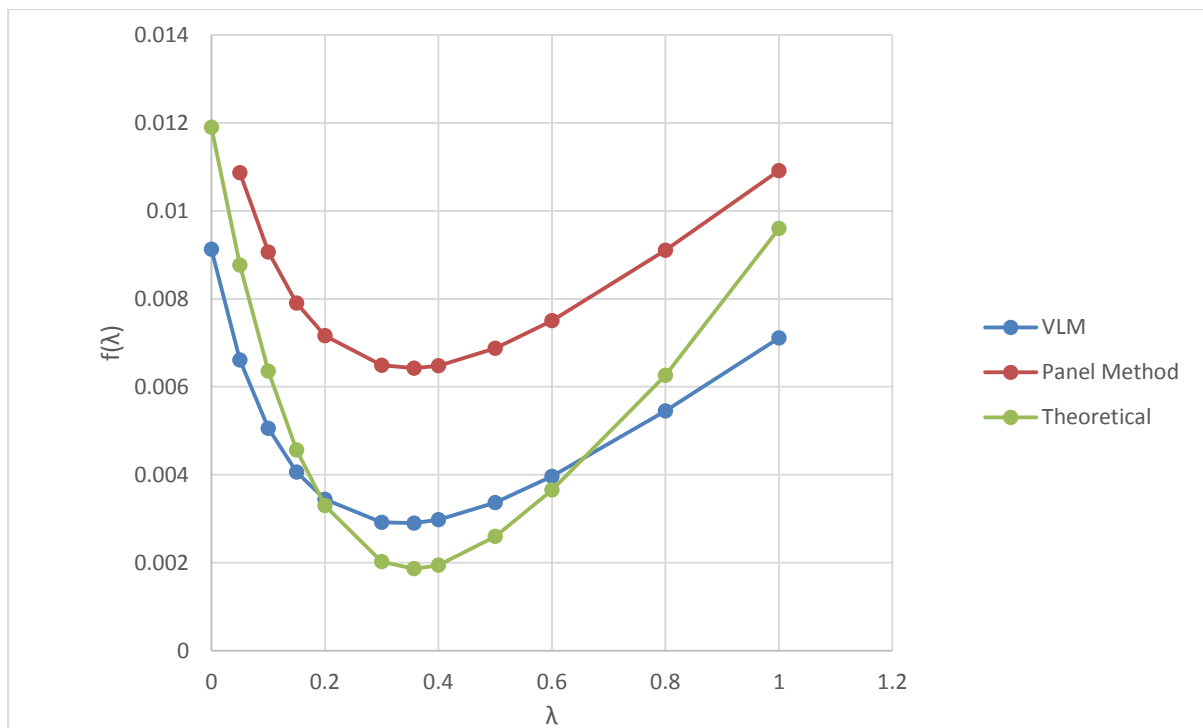
Figure 6.27   Plots showing the relation between f(λ) and taper ratio for results obtained by using VSPAERO: VLM compared with VSPAERO: Panel Metod and with theoretical formulas for Case 9.

7 Box Wing Calculation

7.1 Introduction

The aim of this part of the thesis is to assess VSPAERO's potential as a tool to preliminary designing a box wing. A simple model is taken into account, which will be showed later. With the results of simulations of box wings with different *h/b* ratio (vertical distance length/span), a plot of the $k-$ curve, introduced by Prandtl is created for both VLM and Panel Method. These curves are then compared with those generated from previous research.

7.2 Theoretical Background

In search for leaner and greener ways of air travelling, companies are looking for ways to reduce the induced drag of the wing. Reduced drag will lead to less fuel consumption, which will eventually lead to a reduced ecological footprint. One of the options to do so, is a box wing configuration (Figure 7.1). In a box wing design, a wing is mounted to on the lower belly of the plane and another on the top of the plane which are joined to each other at the tips (Barnstorff 2017). Important to note is that a box wing configuration is still conceptual.

Figure 7.1   Lockheed Martin's concept using a box wing to achieve green aviation goals (Barnstorff 2017).

In this experiment, it is supposed that both wings of the box wing configuration have equal spans. Therefore, the aspect ratio has to be defined as stated in Schiktanz (2011).

$$A = \frac{b^2}{S_1 + S_2} = \frac{b^2}{S} \qquad (7.1)$$

Knowing that the wing of a conventional reference is split into the two wings of the box wing aircraft and assuming that the total wing area as well as the wing span remain the same, the reference aspect ratio is equal to the box wing aspect ratio (Schiktanz 2011).

It is of course possible that both wings of the box wing aircraft have different spans. This would make it necessary to adapt the definition of the aspect ratio. However, this is not considered in this thesis.

The main feature of a box wing configuration is its low induced drag, most commonly expressed by its coefficient as in (7.2) (Schiktanz 2011).

$$C_{D,i} = \frac{C_L{}^2}{\pi \cdot A \cdot e} \qquad (7.2)$$

Clearly, increasing a wings aspect ratio or Oswald factor are possibilities to reduce the induced drag. However, increasing A would make the wing heavier and bigger, which will eventually lead to bigger fuel consumption. Therefore, it is better to increase the Oswald factor of the wing. One way to do so, is using a non planar wing, which have much higher e.

As shown in Figure 7.2, different modifications already have been examined by (Kroo 2005). Important to keep in mind is that in this figure, all configurations have the same span, total lift, and h/b ratio. The number shown next to each configuration is its span efficiency factor e.
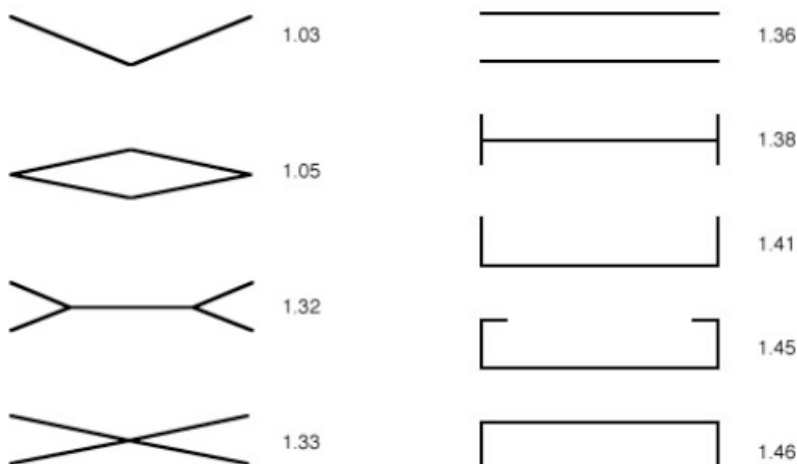
Figure 7.2   Span efficiency for various optimally loaded non planar wing configurations (Kroo 2005).

The following overview gives the reader a rundown of important parameters and assumptions based on literature and already performed experiments.

Span: the same for lower and upper wing.

Reference Area: a sum of the area of a lower and upper wing.

Reference Wing: a single rectangular wing of the same area and span as box wing, for this reason, of a twice longer chord.

h/b – ratio: vertical distance (called also vertical stagger) between both wings over their span. The higher h/b ratio, the higher e, because both wings interfere less with each other. Hence, the best result would be when $h/b \to \infty$.

Decalage: an angle between lower and upper wing. It has an influence on lift distribution. Unit: degree. Positive value means that the upper wing is tilted backwards, increasing α.

Horizontal Stagger: a horizontal distance between lower and upper wing. According to Munk's Stagger Theorem:

> *"The total induced drag of a system of lifting surfaces is not changed when the elements are moved in the streamwise direction." (Munk 1923)*

The glide ratio (*L/D – Lift/Drag*) of a wing is the parameter that determines 'how good' this wing is. To maximize *L/D*, lift should be distributed equally on both wings. In the end Schiktanz (2011) hows the lift distribution on the horizontal wings and the winglets on the left. On the right, it illustrates the wing tip vortices of the box wing configuration Figure 7.3. Those neutralize each other which has a good influence on the induced drag of the wing (Budziak 2015).
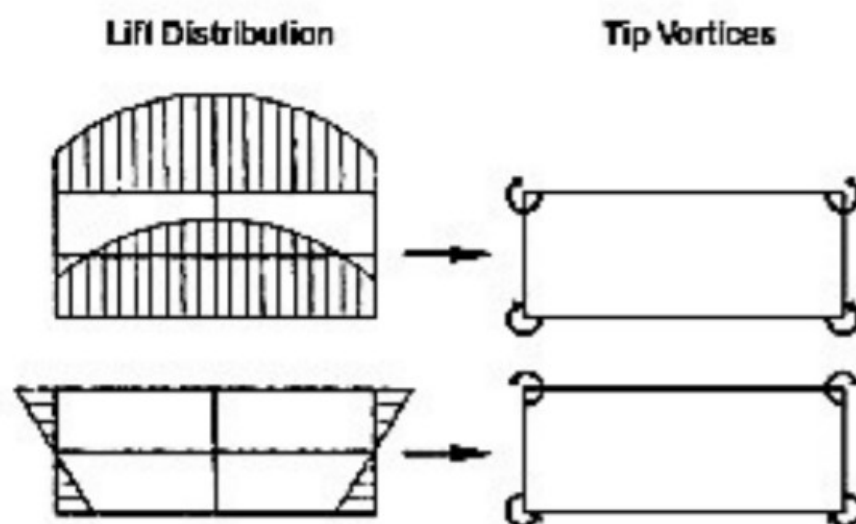
Figure 7.3   Left: Lift distribution on horizontal wings and winglets of the box wing. Right: Counteracting tip vortices due to the lift distribution (Schiktanz 2011).

The induced drag (7.3) is used to compare the performance of the box wing to the performance of the reference wing with the same wing span (Schiktanz 2011).

$$D_i = \frac{L^2}{q \cdot \pi \cdot b^2 \cdot e} \tag{7.3}$$

Assuming that both aircraft have the same weight, wing span and are exposed to the same dynamic pressure, (7.3) can be applied and gives factor k, which is called the induced drag factor and equals to the ratio between the induced drag of the box wing, to the induced drag of the reference wing.

$$\frac{D_{i,BW}}{D_{i,ref}} = \frac{e_{ref}}{e_{BW}} = k \tag{7.4}$$

$D_{i,BW}$ Box wing induced drag,
e_{BW} Box wing Oswald factor,
$D_{i,ref}$ Reference wing induced drag,
e_{ref} Reference wing Oswald factor.

(7.5) is known as *the box wing equation*, introduced by Prandtl, which expresses the induced drag as a function of the h/b ratio. Note that this only accounts for ideally loaded wings.

$$k = \frac{D_{i,BW}}{D_{i,ref}} = f(h/b) = \frac{k_1 + k_2 \cdot h/b}{k_3 + k_4 \cdot h/b} \tag{7.5}$$

In (7.5), k_1 and k_3 are equal to each other as presented in (Rizzo 2007).

7.3 Wind Tunnel Experiment

In the past, a scaled model of a box wing is tested in wind tunnel experiments HAW Hamburg. This wind tunnel has open test section (Göttingen-Type) and is shown in Figure **7.4**.

The airfoil used in the experiment is NACA0015. The reference wing had the dimensions as given in Table 7.1.

Table 7.1   Dimensions of the reference wing used in wind tunnel experiments at HAW Hamburg.

Name	Symbol	Dimension
Span	b	520 mm
Chord	c	100 mm
Aspect ratio	$A=b/c=b^2/S$	5.2

The box wing is build up by two of those reference wings, joined at the tips. Therefore, the wing surface is twice the surface of the reference wing. The aspect ratio of the box wing will hereby be half of the reference wing ($A_{box} = 2.6$).
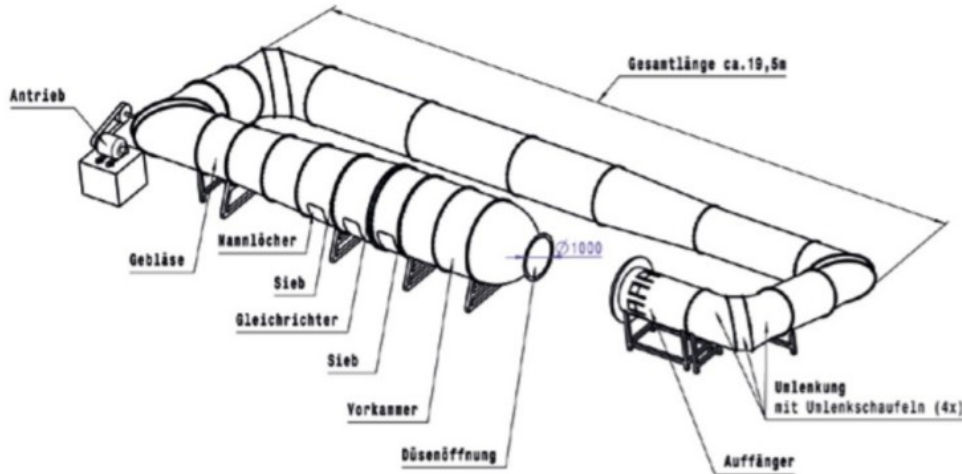
Figure 7.4   Schematic representation of the wind tunnel used to do box wing experiments at HAW Hamburg (Scholz 2019).

First, the reference wing was tested. Afterwards, three box wing configurations were measured, with respectively h/b ratio equal to 0.31, 0.62, and 0.93, done three different times. For each box wing configuration, they calculated the factor k by using (7.4). The results of these experiments can be found in Table 7.2. Afterwards, the mean k is calculated to have one value for each h/b ratio. With these results, k_1 to k_4 were calculated by means of Excel Solver and a curve was fitted at more h/b ratio's (Scholz 2021a). The results obtained by VSPAERO will be compared to these, as well as theoretical values by (Prandtl 1924), (Rizzo 2007), and (Budziak 2015).

Table 7.2   Results for box wing aircraft measurement done by three students at HAW Hamburg

Student Name	type of e_ref	e_ref	e_box			k = e_ref/e_box		
			h/b=0,31	h/b=0,62	h/b=0,93	h/b=0,31	h/b=0,62	h/b=0,93
Fekete	own e_ref	0.805	1.896	1.914	2.177	0.425	0.421	0.370
	average e_ref	0.736	1.896	1.914	2.177	0.388	0.385	0.338
Bikkannavar	own e_ref	0.611	1.161	1.392	1.574	0.526	0.439	0.388
		0.633	1.161	1.392	1.574	0.545	0.455	0.402
	average e_ref	0.736	1.161	1.392	1.574	0.634	0.529	0.468
Ribeiro	own e_ref, 1	0.738	1.190	1.491	1.649	0.620	0.495	0.448
	own e_ref, 2	0.773	1.190	1.491	1.649	0.650	0.519	0.469
	own e_ref, 3	0.753	1.190	1.491	1.649	0.633	0.505	0.457
	average e_ref	0.736	1.190	1.491	1.649	0.619	0.494	0.446
				average:		0.560	0.471	0.420

7.4 Simulation Set-Up

The model used in this experiment, is an exact copy of the test objects used in the wind tunnel experiments as showed in Table 7.1.

Further, in VSPAERO, the *AoA* is set at one point equal to 10°. Bisides that, the Mach number is set on 0.0735. This is calculated based on the air speed in the wind tunnel, which was set on 25 m/s. Calculating towards the Mach number was done based on ISA circumstances (
Table **5.1**).

The simulations were done for a range of h/b ratio from 0.0 (reference wing) to 1.0. The model where h/b is equal to 0.62 is shown in Figure 7.5.
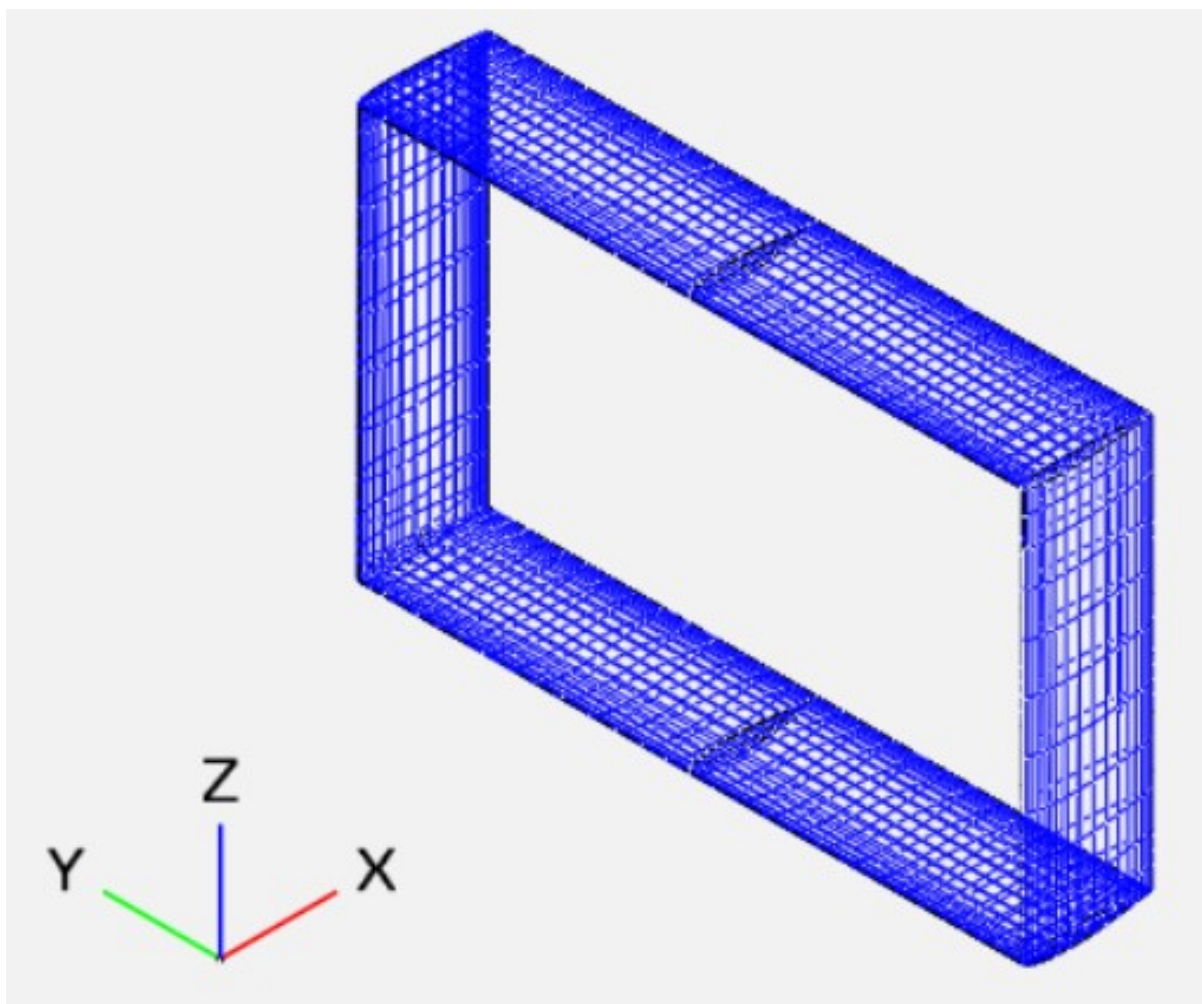
Figure 7.5   Model used for the box wing experiment at h/b =0.62.

7.5 Results

7.5.1 VLM

Simulation of the reference wing, gave an Oswald factor of $e_{ref} = 0.98542$.

The results of the simulations of all h/b ratio is given in Table 7.3. The column called *HAW_VSPAERO_VLM* represents factor k, which is obtained by using (7.4).

Table 7.3   Simulation results for box wing experiment, obtained by using VSPAERO: VLM.

h/b	e_{box}	*HAW_VSPAERO_VLM*
0	0.985	1.000
0.1	1.219	0.808
0.15	1.316	0.749
0.2	1.404	0.702
0.25	1.485	0.663
0.31	1.594	0.618
0.35	1.655	0.595
0.4	1.709	0.577
0.45	1.778	0.554
0.5	1.874	0.526
0.6	1.980	0.498
0.62	2.004	0.492
0.7	2.108	0.467
0.8	2.211	0.446
0.93	2.349	0.420
1	2.487	0.396

It is clear to say that the Oswald factor obtained by VSPAERO: VLM is overestimated, compared to the wind tunnel experiments. E.g. at h/b equal to 0.310, VSPAERO: VLM gives $e_{box} = 1.594$, where the wind tunnel experiment done by Ribeiro only gives $e_{box} = 1.190$. This is the same for the Oswald factor of the reference wing ($e_{ref} = 0.985$ for VSPAERO: VLM and only 0.736 for the wind tunnel experiment by Ribeiro).

Eitherway, when calculating k with the results of VSPAERO: VLM, these errors seem to cancel each other out. For h/b equal to 0.620, VSPAERO: VLM gives $k = 0.492$, where the wind tunnel experiment done by Ribeiro gives $k = 0.494$. The error between both is very small and as factor k is the only factor of interest in this experiment, it can be concluded that the results for k are correct. Nevertheless, it cannot be expressed enough that the result of the individual Oswald factor clearly is overestimated by VSPAERO: VLM, compared to the wind tunnel experiments, which are considered as more realistic.

7.5.2 Panel Method

Simulation of the reference wing, gave an Oswald factor of $e_{ref} = 0.822$.

The results of the simulations of all h/b ratio is given in Table 7.4. The column called *HAW_VSPAERO_PM* represents factor k, which is obtained by using (7.4).

Table 7.4   Simulation results for box wing experiment, obtained by using VSPAERO: Panel Method.

h/b	e_{box}	HAW_VSPAERO_PM
0	0.985	1.000
0.1	1.219	0.808
0.15	1.316	0.749
0.2	1.404	0.702
0.25	1.485	0.663
0.31	1.594	0.618
0.35	1.655	0.595
0.4	1.709	0.577
0.45	1.778	0.554
0.5	1.874	0.526
0.6	1.980	0.498
0.62	2.004	0.492
0.7	2.108	0.467
0.8	2.211	0.446
0.93	2.349	0.420
1	2.487	0.396

Again, the Oswald factor obtained by VSPAERO: Panel Method is overestimated, compared to the wind tunnel experiments. Although, with the Panel Method this is not as big as when using VLM. E.g. at h/b equal to 0.310, VSPAERO: Panel Method gives $e_{box} = 1.281$, where the wind tunnel experiment done by Ribeiro only gives $e_{box} = 1.190$. This is the same for the Oswald factor of the reference wing ($e_{ref} = 0.821$ for VSPAERO: Panel method and only 0.736 for the wind tunnel experiment by Ribeiro). Where the error between wind tunnel experiments and VSPAERO was around 25% for VLM, this is lowered to around 10% when using the Panel Method instead.

When calculating k with the results of VSPAERO: Panel Method, these errors cancel each other out again. Looking at h/b equal to 0.620, VSPAERO: Panel Method gives $k = 0.493$, where the wind tunnel experiment done by Ribeiro gives $k = 0.494$. The error between both is very small and, as said, factor k is the only factor of interest in this experiment. Thus, it can be concluded that also when using the Panel Method, the results for k are correct. But also again, it cannot be expressed enough that the result of the individual Oswald factor clearly is overestimated by VSPAERO: Panel Method, compared to the wind tunnel experiments, which are considered as more realistic.

7.5.3 Comparison with Previous Research

Figure 7.6 shows the results obtained by this experiment.

The plot derived by using VLM is very similar to the one obtained from Prandtl and the wind tunnel experiments (*HAW_exp,fit*). The same goes for the panel method. Although, at low h/b ratio the panel method seems to be less stable and thus reliable than VLM. From $h/b = 0.400$ this doesn't seem to be a problem anymore. From then on, both curves are almost copies of each other. Even looking at the last simulation point, where there is a little kink in the curve visible. Nevertheless, this kink stays in the expected range so this point is still seen as correct.
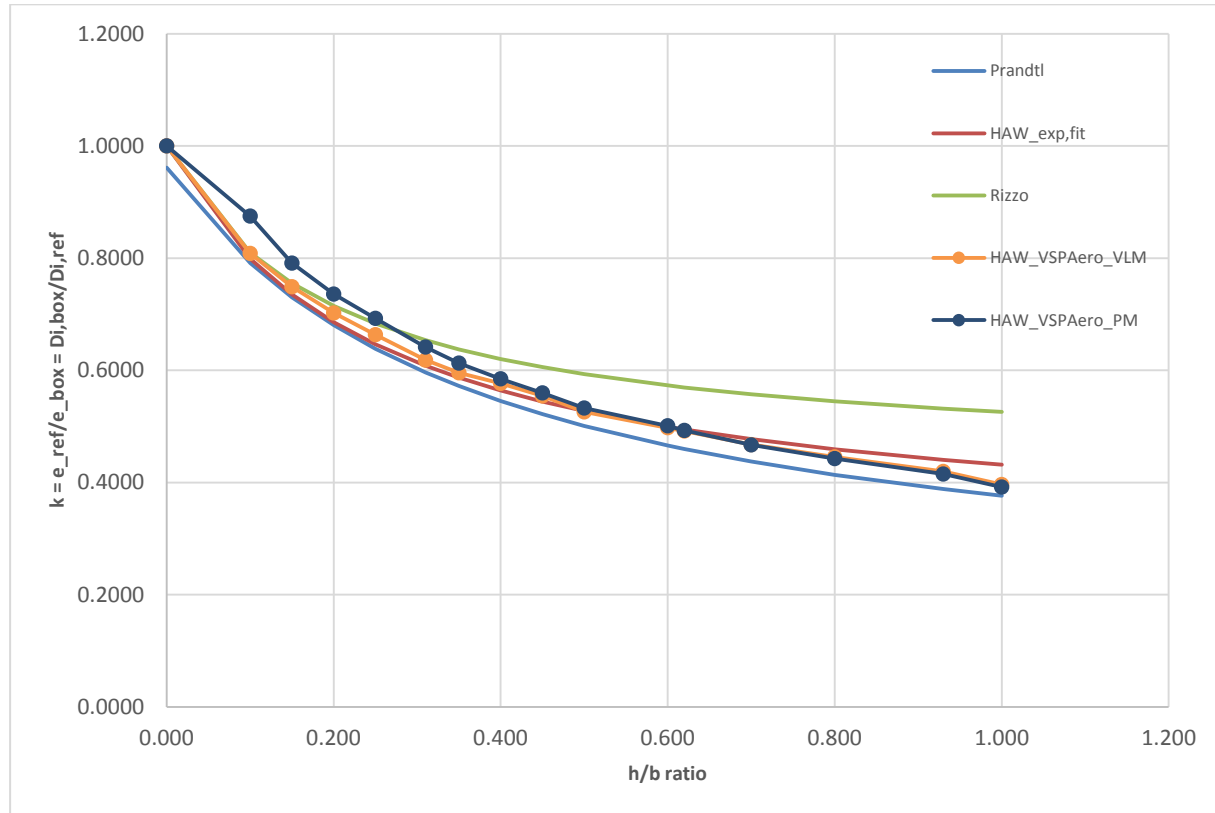
Figure 7.6   Plots showing factor k as function of h/b ratio for multiple experiments and calculations.

8   Pressure Distribution

VSPAERO's Viewer allows the user to see the flow visualization like pressure distribution, trailing wakes, vorticity, and so on of the simulation. This chapter will briefly check if this happens as expected, by looking at the pressure distribution and trailing wakes, without looking at exact numbers.

8.1   Theoretical Background

When two solid object interect in a mechanical process, forces apply at the point of contact. But when a solid object interacts with a fluid, things are harder to describe, because the fluid can change its shape. For a body immersed in a fluid, the "point of contact' is every point on the surface of the body. The fluid can flow around the body and maintain physical contact at all points. The application of mechanical forces between the solid body and cluid therefore occurs at every point on the surface of the body, through the fluid pressure (Hall 2021a).

The magnitude of the force F acting on a small section of the immeres object equals the pressure p times the area S of the section is

$$F = p \cdot S \ .$$
(8.1)

Pressure is a scalar quantity releated to the momentum of the molecuses of a fluid. Since a force is a vector quantity, having both magnitude and direction, the direction of the pressure force has to be determined. It is known that pressure always acts perpendicular to the solid surface of an object. Therefore, the direction of the force on the small section of the object is alont the normal to the surface. This direction is denoted by the letter n (Hall 2021a).

Along the body of a solid body (in this case an aircraft), the normal direction changes. To obtain the net mechanical foce F over the entire solid object, the contribution of every small section have to be summed up (Hall 2021a).

$$F = \sum (p \cdot n \cdot \Delta S)$$
(8.2)

In the limit of infinitely small sections, this gives the integral of the pressure multiplied by the area around the closed surface. The integral is taken all around the body, that's why there's a circle sign trough the integral sign (Hall 2021a).

$$F = \oint (p \cdot n) dS \tag{8.3}$$

From general fluid dynamics, flow separation is known as the detachment of a boundary layer from the surface into a wake (White 2011). In aerodynamics, flow separation results in reduced lift and increased pressure drag, caused by the pressure differential between the front and rear surfaces of the object.[2]

According to the Bernoulli's principle, the total pressure p_t along a streamline is constant. This means that the sum of the static pressure p_s and dynamic pressure p_d is constant. Because the air over the top of the wing has to travel a longer distance than the air under the wing, this air has to go faster. According to Bernoulli's principle (8.4), faster flowing air will exert less pressure than slower flowing air. This pressure difference will eventually lead to lift on the wing. Flow restrictions of Bernoulli's principle are:
- Flow is considered inviscid
- Flow is considered steady
- Flow is considered incompressible
- No heat addition
- Negligible change in height

(Hall 2021b)

$$p_s + p_d = p_t = constant \tag{8.4}$$

The dynamic pressure is calculated by dividing the multiplication of the fluid density ρ with the square of its velocity V by two (Hall 2021b) is

$$p_d = \frac{\rho \cdot V^2}{2} \quad . \tag{8.5}$$

Combining (8.4) and (8.5) gives

$$\left(p_s + \frac{\rho \cdot V^2}{2} \right)_1 = \left(p_s + \frac{\rho \cdot V^2}{2} \right)_2 \quad . \tag{8.6}$$

8.2   Simulation Set-up

The model used is a copy of the Airbus A320, created with OpenVSP-Connect. OpenVSP-Connect is an Excel-besed interface file format, which is defined for the exchange of aircraft sizing data. It is an Excel file with macro's (called OpenVSP-connect.xlsm) and connects to

---

[2]   For more details, the reader can look into literature such as (Anderson 1995).

OpenVSP for the display of the aircraft (Scholz 2021b). OpenVSP-Connect is part of the lecture Aircraft Design at Hamburg Open Online University and Aircraft Design / Flugzeugentwurf at HAW Hamburg.

Important to know is that OpenVSP-Connect works with OpenVSP 2 instead of OpenVSP 3 used in this thesis. Therefore, the .vsp file created by OpenVSP-connect has to be converted to a .vsp3 file in order to do aerodynamic analysis on it. When doing this, the engines of the airplane disappear. Therefore, also the pylons are manually removed in the .vsp3 file. The resulting model is thus a fuselage, wing and tail configuration, as shown in Figure 8.1.

Further, the simulation is done at an *AoA* of 10°, at the cruise Mach number of the Airbus A320 ($M = 0.78$) (Airbus 2019), see Figure 8.2.
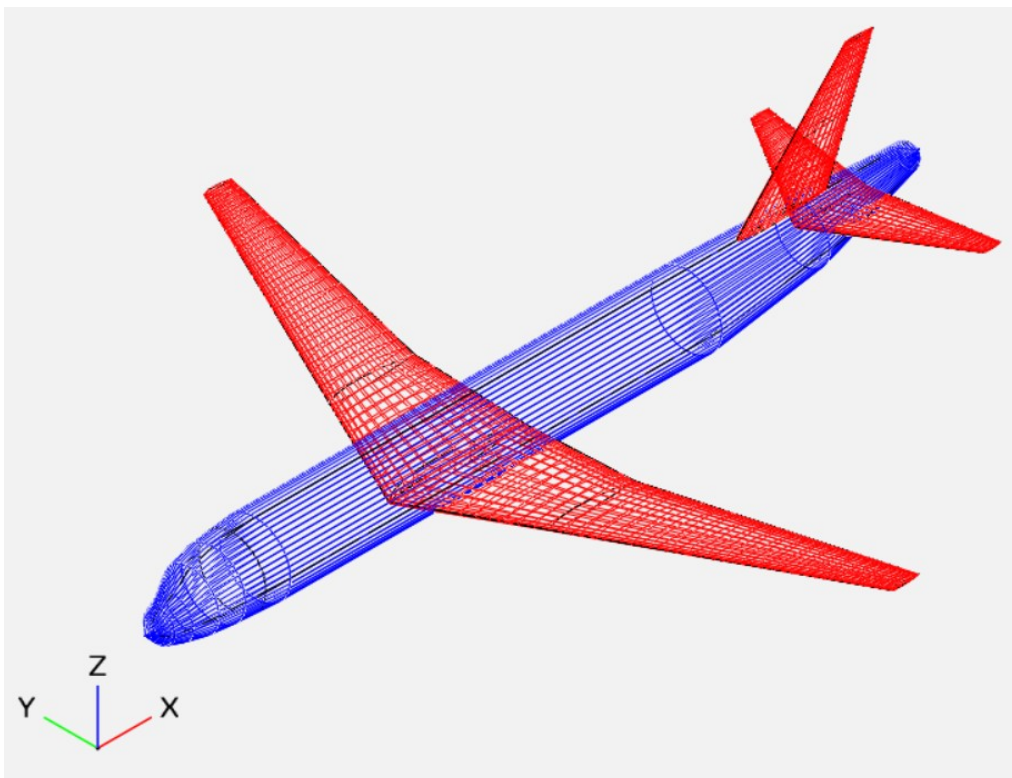
Figure 8.1   Model created by OpenVSP-Connect, based on parameters of the Airbus A320.
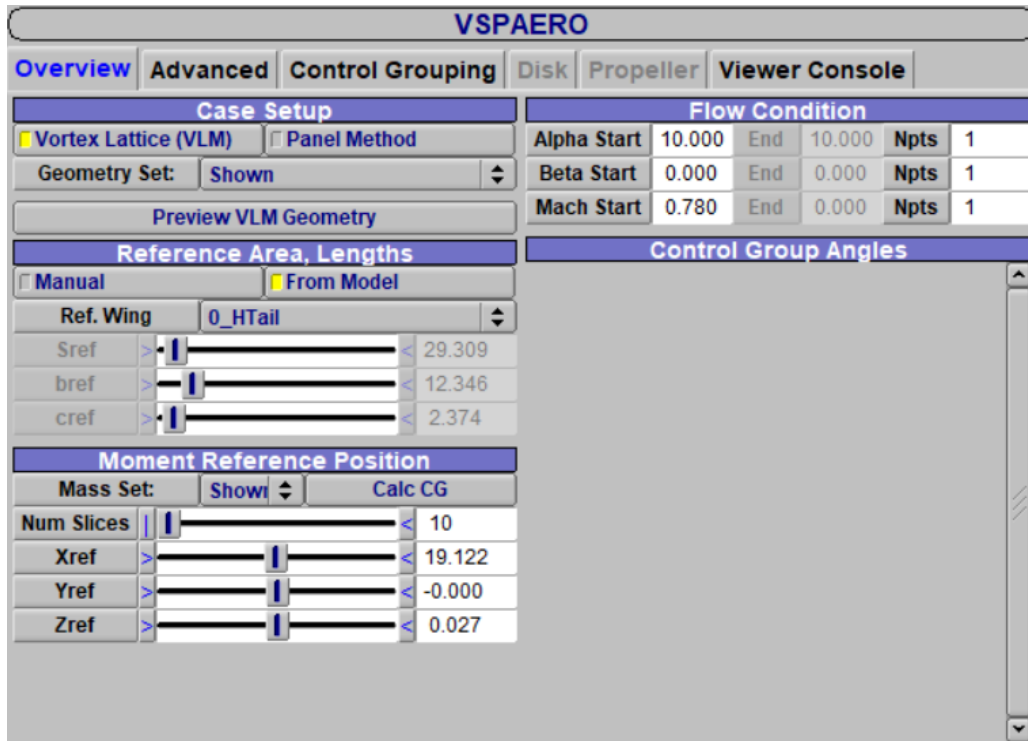
Figure 8.2   VSPAERO simulation set-up for the pressure distribution experiment.

8.3   Results

The results are shown in three figures, from the top, bottom, and front. The reader must know that VSPAERO does not provide its user with a 'live' simulation. The wake build up and pressure distribution as in the last iteration will be presented.

Because of Bernoulli's principle, it is expected to have a low pressure on the top of the wing and a high pressure coefficient on the bottom of the wing.

8.3.1   VLM

For starters, the visualization obtained by using VLM is shown in Figure 8.3 and Figure 8.4.

It can easily be stated that VLM isn't a well suited option for flow visualization. For starters, the trailing wakes of the simulation are very straight. Very little vortices are visible. Furthermore, the pressure distribution doesn't satisfy the expectations. In Figure 8.4, it can be seen that also the pressure on the bottom of the wing would be very low. This completely goes into Bernoulli's principle and is therefore considered inaccurate.

On the other side, the wing tip vortices are visible, especially in Figure 8.5. This does satisfy the expectations.
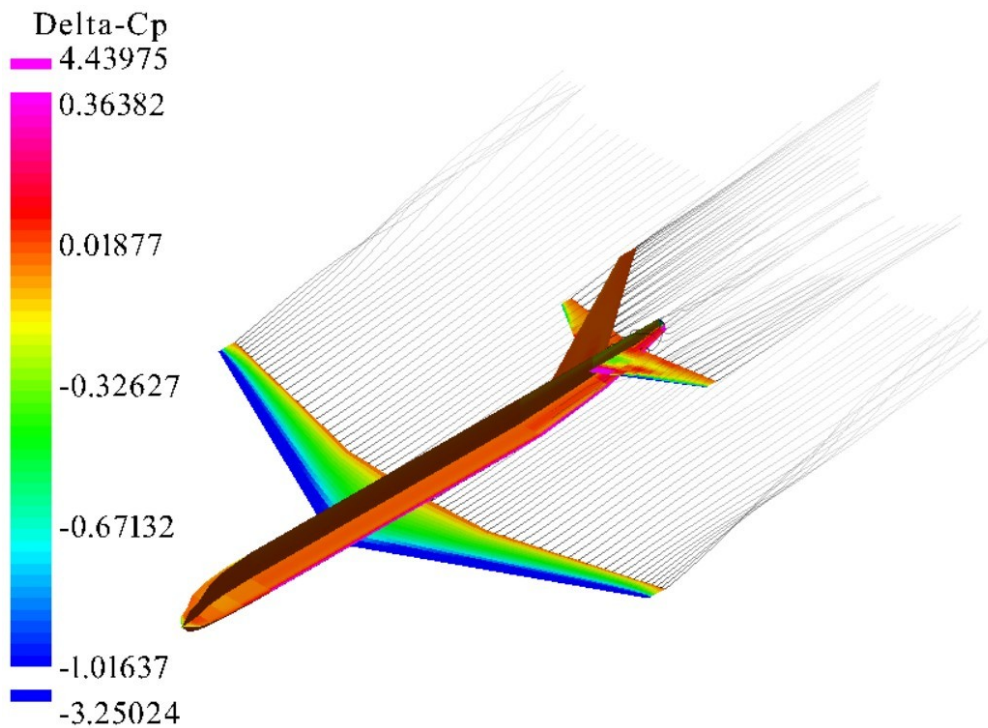
Figure 8.3   Visualization by VSPAERO Viewer for simulation of an Airbus A320 configuration by means of VLM seen from the top left isometric perspective.
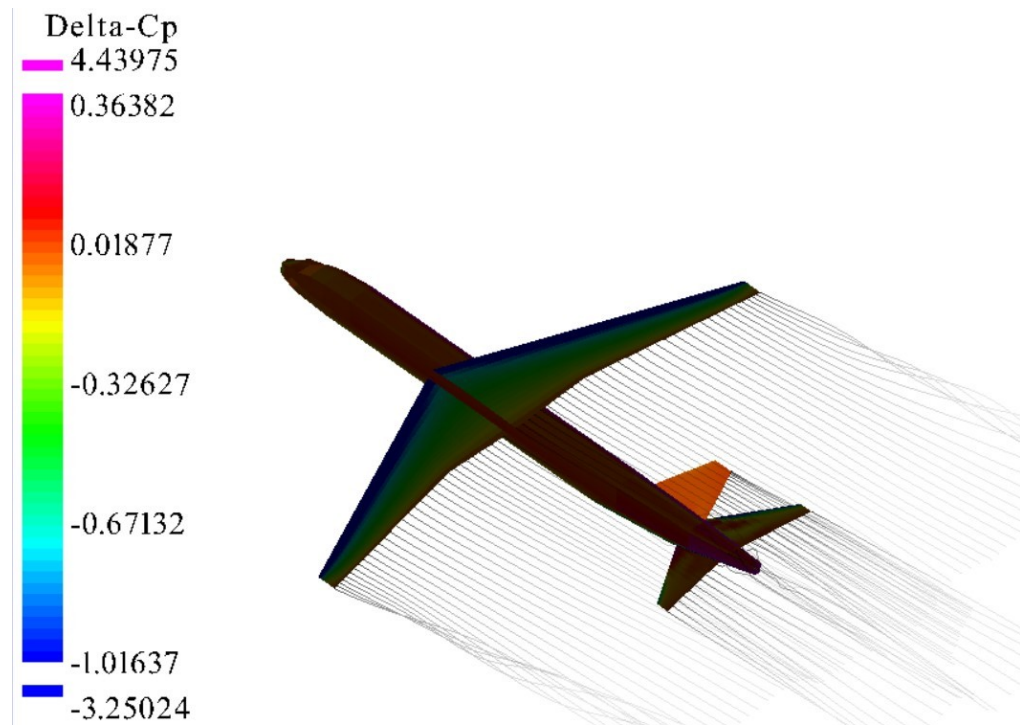
Figure 8.4   Visualization by VSPAERO Viewer for simulation of an Airbus A320 configuration by means of VLM seen from the bottom left isometric perspective.
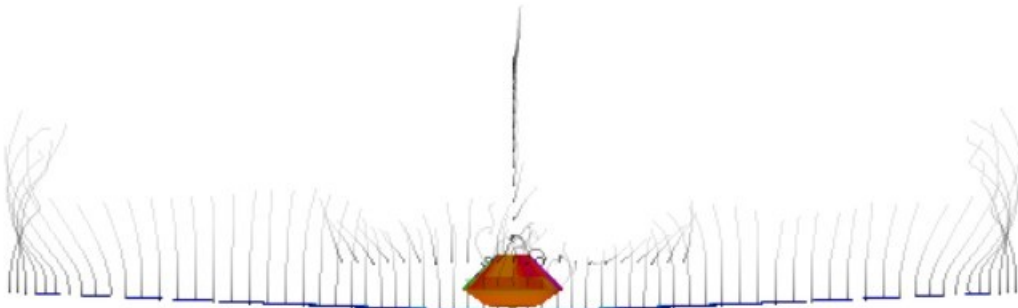
Figure 8.5   Visualization by VSPAERO Viewer for simulation of an Airbus A320 configuration by means of VLM seen from the front.

8.3.2   Panel Method

Secondly, the visualization obtained by simulating with the Panel Method is shown (Figure 8.6, Figure 8.7 and Figure 8.8) and discussed.

At a first glance the panel method seems a lot more suited for flow visualization than VLM. The trailing wakes are much more 'active' when using Panel Method than with VLM. Also, the pressure distribution is completely according to the expectations based on Bernoulli. On Figure 8.7, the background is changed to blue to make the colored scheme visually better.
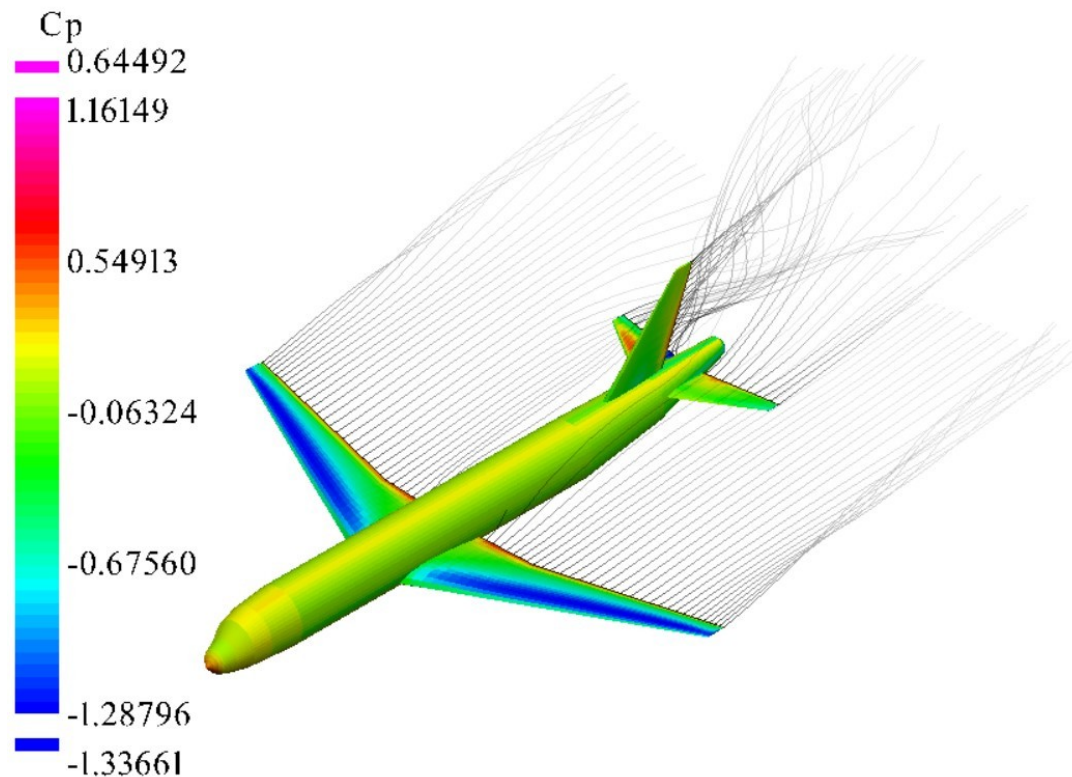
Figure 8.6   Visualization by VSPAERO Viewer for simulation of an Airbus A320 configuration by means of the panel method seen from the top left isometric perspective.
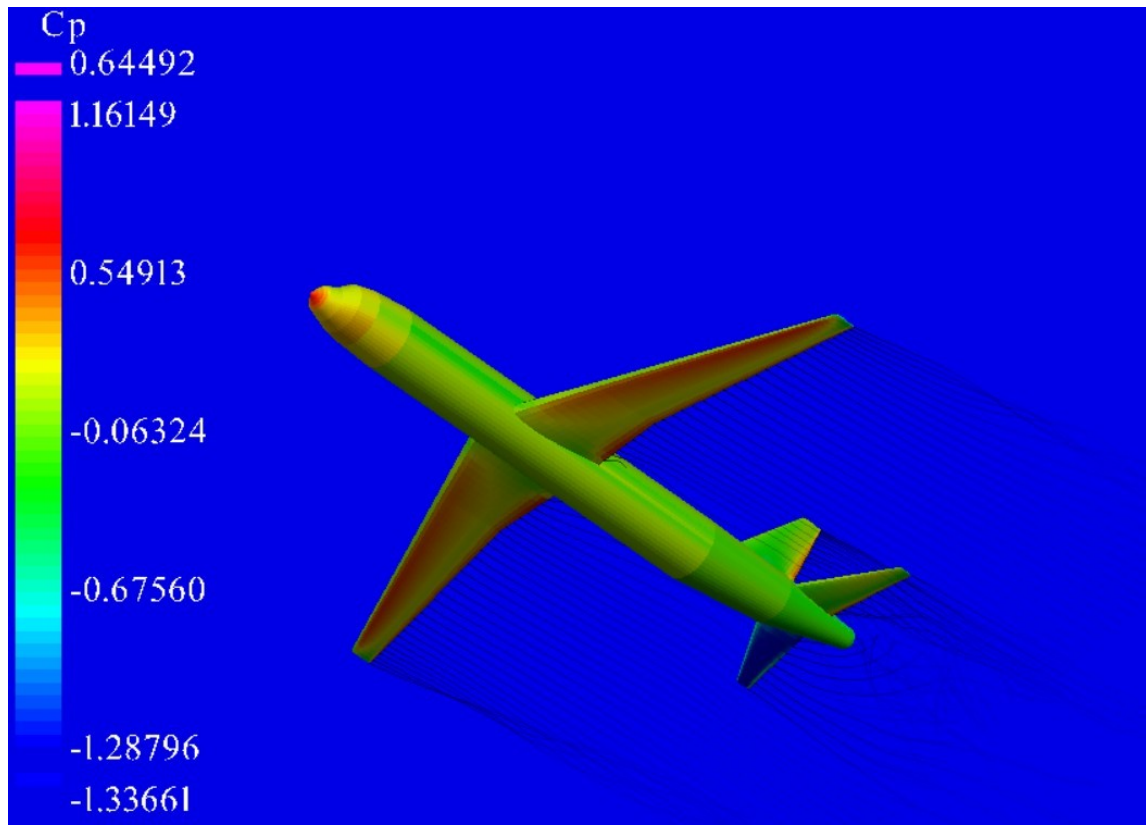
Figure 8.7   Visualization by VSPAERO Viewer for simulation of an Airbus A320 configuration by means of the panel method seen from the bottom left isometric perspective.
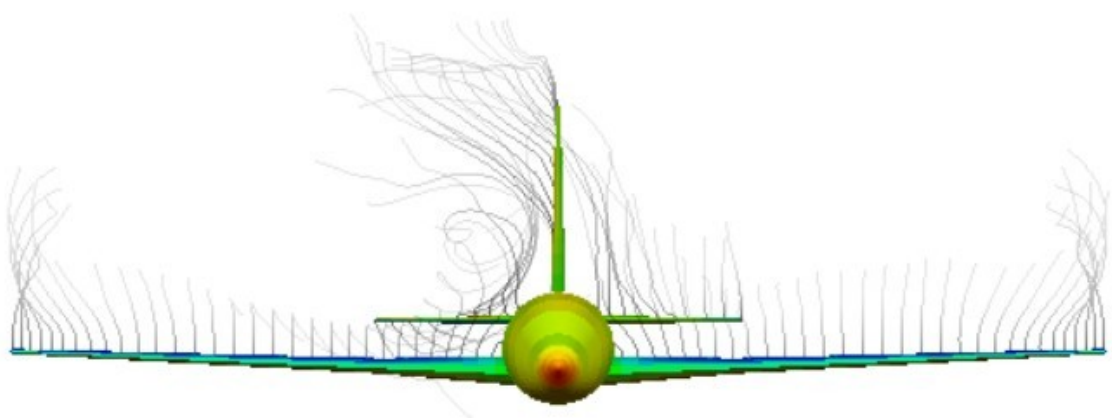
Figure 8.8   Visualization by VSPAERO Viewer for simulation of an Airbus A320 configuration by means of the panel method seen from the front.

9   User Guide

This chapter will provide the reader a bullet point user guide to get started with VSPAERO. For more detailed information, the reader is invited to visit OpenVSP's website, follow their tutorials and read through the OpenVSP Ground School, which is still in development at moment of writing.

9.1   Launching Simulation

- Once the model is appropriately defined, VSPAERO can be opened by opening the Analysis tab and clicking on VSPAERO, illustrated by Figure 9.1.
- VSPAERO opens in the form of a pop-up window, looking like shown in Figure 9.2.
- In this window, the user can choose to use whether VLM or the Panel Method under the tab Case Setup
- At Geometry Set, the user is allowed to select which set(s) of geometries he wants to analyse. As per default, this is set to all shown geometries.
- At the tab Reference Area, Lengths it is recommended to select From Model. By default, VSPAERO then selects the main wing of your model as reference geometry and copies the corresponding properties.
- After that, the Moment Reference Position has to be calculated. First, the Mass set has to be selected. This works the same as selecting the Geometry Set at Case Setup. Afterwards, the center of gravity is calculated by just clicking the button Calc CG.
- Then, the flow condition is defined by the input of different Alpha and Beta angles, as well as the Mach number.
- Under the tab Advanced (Figure 9.3) there are some more possibilities:
- At first, at Advanced Case Setup, the user can select where he wants to store the Degen or Panel file. All other default options were sufficient for the experiments done in this thesis. Therefore, it is supposed this is the same for most simulations.
- The Wake part, is where the user can adapt how many iterations have to be done and for how many wake nodes. The number of iterations has to be big enough, to make sure there are little residuals left and the final outcome is stable.
- At Control Grouping, VSPAERO allows trimming of the vehicle's control surface deflections.[3] This was not necessary for the experiments done in this thesis.
- The simulation is started by clicking the Launch Solver button.
- A simulation can be stopped by clicking the Kill Solver button.

---

[3]   More details about Control Grouping can be found in (Litherland 2018b) under the heading "Control Grouping".
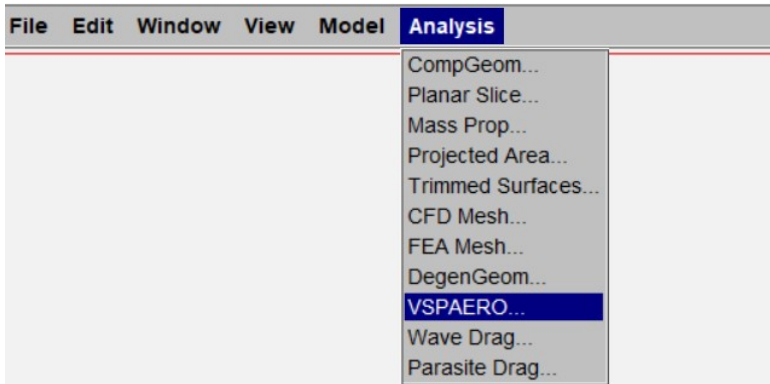
Figure 9.1   Opening VSPAERO by unfolding the Analysis tab in OpenVSP.
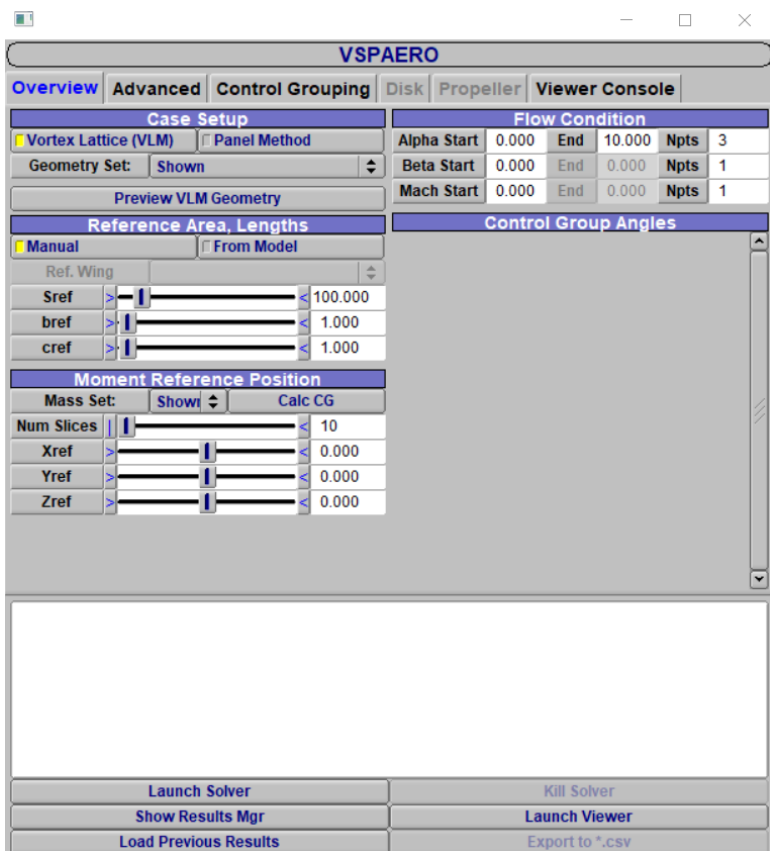
Figure 9.2   Pop-up window after opening VSPAERO.
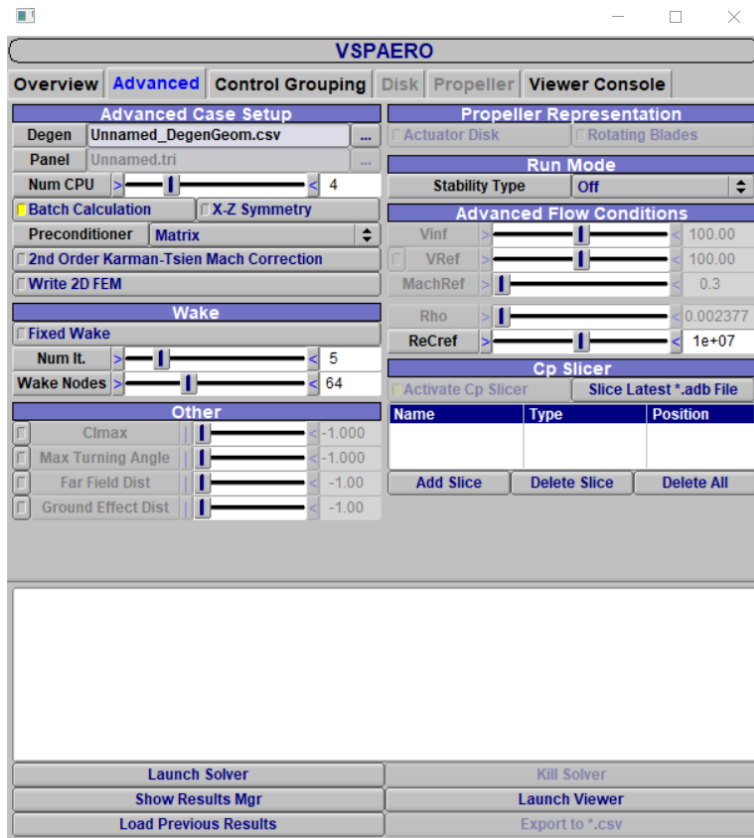
Figure 9.3   Advanced tab in VSPAERO.

9.2   Managing Results

- After the simulation is completed, the results manager pops up. Here, the user gets a graphical overview of the residuals of selected parameters, lift distribution, etc. Or he can make a graphic as he needs under the Sweep tab, by selecting correct x-data and y-data, as shown in Figure 9.4.

- Further, the results can me exported to a .csv-file. This makes further analysis and calculations with the results possible.

- Another possibility is making the results visual. This is explained in Chapter 1.
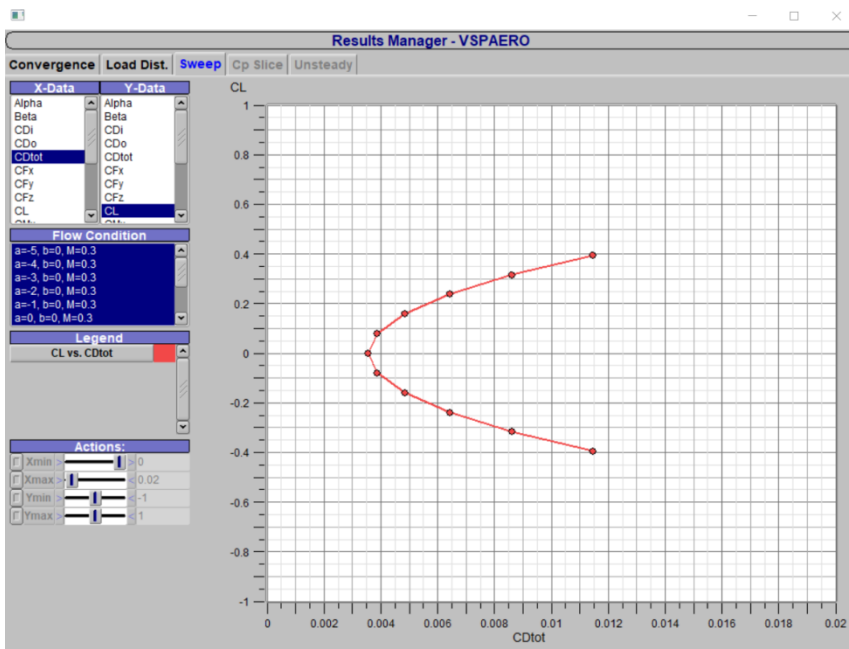
Figure 9.4   Results Manager of VSPAERO showing the drag polar obtained by simulating the default wing with AoA going from -5° to +5° at M = 0.3.

10   Summary and Conclusions

10.1   Summary

After studying the possibilities of VSPAERO, the theory behind it, and what has been done before, several experiments were set up to determine the working of VSPAERO while using VLM and also Panel Method.

First, there has been experimented with panel refinement. This was done to find the sweet spot between reliable results and a short solve time. Out of this experiment, some rules of thumb were adopted and used during the rest of the experiments.

Afterwards, the lift curve slope was examined for a rectangular wing. The simulation results were compared to calculations done with well-known theoretical formulas. Comparison was done visually, by plotting the simulation results and the calculated values for C_L as a function of α, as well as numerically, by calculating the deviation percentage between both outcomes. There is also good agreement for values of the lift curve slope calculated with theoretical formulas and those values obtained with the VLM or panel method.

The third experiment was the recreation of Hoerner's Curve. By means of simulation results for C_L, C_{Di}, and e, Hoerners function $f(\lambda)$ was calculated and compared with $f(\lambda)$ obtained from the VLM and the panel method. The VLM showed a less unified picture on its $f(\lambda)$ curves. VLM and the panel curves where defined as "correct". Subsequently, correction factors were applied to Hoerner approach (6.3) to yield either the VLM or the panel values approximately.

After working with monoplane wings, box wing configurations were investigated too. With the results gathered form the simulations where a box wing configuration varied in h/b rato, the curve k was built for VLM as well as Panel Method. These curves were then compared to the ones presented by Prandtl, Rizzo and extensive wind tunnel experiments done at HAW Hamburg. Previous results were confirmed.

The last experiment covered the possibilities of flow visualization in VSPAERO. By launching the viewer and selecting *pressure distribution* and *trailing wakes* the figures as shown in Chapter 9 are obtained. As said before, VSPAERO does not provide live imaging of the simulation but only the outcome of the last iteration is shown.

To end this thesis, a bullet point user guide for doing simulations with VSPAERO was written.

10.2 Conclusions

Coming to the end of this thesis, it can be concluded that VSPAERO meets its design requirements. VSPAERO provides quick, reliable, and relative correct results compared to theoretical, and experimental results done before. In preliminary aircraft design, VSPAERO can provide a rough idea of the aerodynamics of the design, without having to do extensive CFD simulations or wind tunnel tests. This can save a significant amount of time in the design process.

Nevertheless, there are imperfections to it. The flow conditions are simplified and therefore VSPAERO will not provide exact results. It is designed for giving quick results. Also, the model used in simulations has to be carefully refined to get relevant results as an outcome. And from trials done on the side, it was experienced that VSPAERO had difficulties with solving when the model got more complex.

In general, VLM is the most straight forward method to be used to get results for e.g. lift coefficient, induced drag coefficient, etc. On the other hand, regarding flow visualization, it is clear to say that using the Panel Method provides more realistic results. As a pay-off for that, the simulation will generally take longer compared to using VLM.

11   Recommendations

As mentioned in the beginning, the refinement study can use a more systematic build-up to get to the optimum refinement for each model. A design of experiments (DOE) can explicitly clarify which parameters have the biggest influence on the results, and on the other hand, the solve time.

Further research into VSPAERO can imply research done on more complicated models, e.g. wings with flaps, aircraft with disc actuators, etc. Also, there are lots of experiments that can be done with VSPAERO, that aren't carried out in this thesis. For example, there could be taken a look at the lift distribution of a wing, or making a drag estimation for a full aircraft configuration and compare the results with theoretical methods.

List of References

ABBOTT, Ira H., 1959. *Theory of Wing Sections*. New York, USA: Dover Publications, Inc.
   Available from: https://doi.org/10.1017/S0368393100116724
   Open access at: https://bit.ly/36DC3Y2
   Archived at: https://perma.cc/UP68-9ZSG

AIRBUS, 2019. *A320 Family Technology*. Airbus S.A.S..
   Archived at: https://bit.ly/3B8fuZv

ANDERSON, John D. Jr, 2011. *Fundamentals of Aerodynamics*. Second Edition. New York, USA: McGraw-Hill.
   Available from: https://www.mheducation.com/highered/product/M9781259129919.html
   Open access at: https://bit.ly/36FkfMf
   Archived at: https://perma.cc/V2PX-N7L3

BARNSTORFF, Kathy, 2017. *New Ideas Sharpen Focus for Greener Aircraft*. National Aeronautics and Space Administration.
   Available from: https://www.nasa.gov/topics/aeronautics/features/greener_aircraft.html
   Archived at: https://perma.cc/T9HG-AD4X?type=image

BERTIN, John J., 2009. *Aerodynamics For Engineers*. New Jersey, USA: Pearson Education.
   Available from: https://doi.org/10.1017/9781009105842
   Open access at: https://bit.ly/3hLz7iC
   Archived at: https://perma.cc/WPQ3-FMM7

BUDZIAK, Kinga, 2015. *Aerodynamic Analysis with Athena Vortex Lattice (AVL)*. Project. Hamburg, Germany: Hamburg University of Applied Sciences.
   Available from: https://nbn-resolving.org/urn:nbn:de:gbv:18302-aero2015-09-20.015

DATCOM, 1978. *USAF Stability and Control Datcom*. Long Beach, California, USA: USAF.
   Available from: https://apps.dtic.mil/sti/citations/ADB072483
   Archived at: https://perma.cc/LQ5Y-RE5K

DRELA, Mark, 2013. *AVL Overview*. Massachusetts, USA: Massachusetts Institute of Technology.
   Available from: https://web.mit.edu/drela/Public/web/avl
   Archived at: https://perma.cc/95A7-98ER

ERICKSON, Larry L., 1990. *Panel Methods – An Introduction*. National Aeronautics and Space Administration. NASA Technical Paper 2995.
Available from: https://ntrs.nasa.gov/citations/19910009745
Archived at: https://perma.cc/W63S-FWW2

FUENTES GALAN, Marius, 2018. *Aircraft Modeling Through BeX & OpenVSP*. Project. Linköping, Sweden: Linköping University.
Available from: https://hdl.handle.net/10251/144510
Archived at: https://perma.cc/H7DZ-2A3R

GUDMUNDSSON, Snorri, 2014. *General Aviation Aircraft Design*. First edition. Oxford, UK: Elsevier.
Available from: https://www.elsevier.com/books/gudmundsson/978-0-12-818465-3
Open Access at: https://bit.ly/3rcNjE8
Archived at: https://perma.cc/Y4RU-M9CJ

HALL, Nancy, 2021a. *Aerodynamic Forces*. Cleveland, USA: National Aeronautics and Space Administration.
Available from: https://www.grc.nasa.gov/www/k-12/airplane/presar.html
Archived at: https://perma.cc/FV9S-KXJX

HALL, Nancy, 2021b. *Bernoulli's Equation*. Cleveland, USA: National Aeronautics and Space Administration.
Available from: https://www.grc.nasa.gov/www/k-12/airplane/bern.html
Archived at: https://perma.cc/RJA6-WA53

HOERNER, Sighard F., 1965. *Fluid-Dynamic Drag*. Bakersfield, CA, USA: Published by the Author.
Available from: https://bit.ly/3k1VjGj
Open access at: https://n2t.net/ark:/13960/t57f0bk2j

HULL, David G., 2007. *Fundamentals of Airplane Flight Mechanics*. Austin, Texas, USA: Springer.
Available from: https://www.springer.com/gp/book/9783540465713
Open access at: https://www.academia.edu/40860295
Archived at: https://perma.cc/9LJF-DA6G

KROO, Ilan., 2005. *Nonplanar Wing Concepts For Increased Aircraft Efficiency*. Stanford, USA: Von Karman Institute for Fluid Dynamics [Lecture series].
Available from: https://bit.ly/36FuJv3
Archived at: https://perma.cc/MRV7-7PD7

KROO, Ilan, 2007. *Applied Aerodynamics: A Digital Textbook*. Stanford, CA, USA: Desktop
Aeronautics.
Archived at: https://bit.ly/3yhtGwy

LAMBERT, Mark, 1993. *Jane's all the World's Aircraft*. United Kingdom: Jane's Information
Group.
Available from: https://bit.ly/3lhGOgU
Archived at: https://perma.cc/GS87-U4LZ

LAN, Edward, C., 1973. *A Quasi-Vortex-Lattice Method in Thin Wing Theory*. Kansas, USA:
American Institute of Aeronautics and Astronautics.
Available from: https://doi.org/10.2514/3.60381 (Closed Access)

LITHERLAND, Brandon, 2021a. *OpenVSP Ground School*. National Aeronautics and Space
Administration.
Available from: https://vspu.larc.nasa.gov
Archived at: http://web.archive.org/web/20210920032443/https://vspu.larc.nasa.gov

LITHERLAND, Brandon, 2021b. *Using VSPAERO*. National Aeronautics and Space
Administration.
Available from: http://openvsp.org/wiki/doku.php?id=vspaerotutorial
Archived at: https://perma.cc/YQ5U-B7QE

LIU, Chao, 2007. *Wake Vortex Encounter Analysis with Different Wake Vortex Models Using
Vortex-Lattice Method*. Master Thesis. Delft: Delft University of Technology.
Available from: https://bit.ly/3z6FPoW

MASON, William H., 2015. *Applied Computational Aerodynamics: A Modern Engineering
Approach*. Cambridge, USA: Cambridge University Press.
Available from: https://doi.org/10.1017/CBO9781107284166.001
Open access at: http://www.dept.aoe.vt.edu/~mason/Mason_f/CAtxtTop.html
Archived at: https://bit.ly/3Ex6RJQ

MUNK, Max M., 1923. *General Biplane Theory*. Springfield, Virginia, USA: National
Advisory Committee for Aeronautics Report: 151.
Available from :   https://digital.library.unt.edu/ark:/67531/metadc65802/
Archived at: https://perma.cc/X522-AWWG

NIȚĂ, Mihaela; SCHOLZ, Dieter, 2012. Estimating the Oswald Factor from Basic Aircraft Geometrical Parameters. In: *Publikationen zum DLRK 2012* (Deutscher Luft- und Raumfahrtkongress, Berlin, 10. - 12. September 2012).
Available from: http://nbn-resolving.org/urn:nbn:de:101:1-201212176728

OPENVSP. *About OpenVSP*. National Aeronautics and Space Administration.
Available from: http://openvsp.org/learn.shtml
Archived at: https://perma.cc/HG5M-2H8M

OPENVSP, 2021. *OpenVSP Hangar*. National Aeronautics and Space Administration.
Available from: http://hangar.openvsp.org
Archived at: https://perma.cc/PZE9-BGKX

OPENVSP, 2014. *OpenVSP Logo*. Twitter.
Available from: https://twitter.com/openvsp
Archived at: https://perma.cc/D2AJ-4XE2?type=image

OPENVSP, 2015. *OpenVSP3.1.0 and VSPAERO Released*. National Aeronautics and Space Administration.
Available from: https://bit.ly/3z4sJZl
Archived at: https://perma.cc/6S3Z-4PMT

PRAMESWARI, Carry, 2017. *Simulation Model Development of a Subscale Fighter Demonstrator: Aerodynamic Database Generation and Propulsion Modeling*. Master Thesis. Linköping, Sweden: Linköping University.
Available from: https://urn.kb.se/resolve?urn=urn:nbn:se:liu:diva-138769
Archived at: https://perma.cc/EBP2-76C2

PRANDTL, Ludwig, 1924. *Induced Drag of Multiplanes*. National Advisory Committee for Aeronautics. Technical Report 182.
Available from: https://go.nasa.gov/2VJe8ok
Archived at: https://perma.cc/8QF3-7ZHR

RAYMER, Daniel P., 1992. *Aircraft Design: A Conceptual Approach*. Playa del Rey, California, USA: AIAA Education Series.
Available from: https://doi.org/10.2514/4.104909
Archived at: https://perma.cc/TA7P-7VYA

RIZZO, Emanuele, 2007. *Optimization Methods Applied to the Preliminary Design of Innovative, Non Conventional Aircraft Configurations*. Pisa, Italy: Edizioni ETS. ISBN: 978-8-846724-5-88
Available from: https://bit.ly/3hIDCu8
Archived at: https://perma.cc/DL3Y-5CXL

SCHIKTANZ, Daniel, SCHOLZ, Dieter, 2011. Box Wing Fundamentals - An Aircraft Design Perspective. In: *DGLR: Deutscher Luft- und Raumfahrtkongress 2011 : Tagungsband - Manuskripte* (DLRK, Bremen, 27. - 29. September 2011), pp. 601-615. - ISBN: 978-3-932182-74-X. DocumentID: 241353.
Available from: http://Airport2030.ProfScholz.de
Archived at: https://perma.cc/3K8E-N6L7

SCHOLZ, Dieter, 2017. Chapter 7: Wing Design. In: *Aircraft Design Lecture Notes*. Hamburg, Germany: Hamburg University of Applied Sciences.
Available from: https://bit.ly/3wFAzad
Archived at: https://perma.cc/4EZ3-ZL26

SCHOLZ, Dieter, 2019. *Induced Drag Estimation of Box Wings for Conceptual Aircraft Design*. Deutscher Luft- und Raumfahrtkongress 2019, (Darmstadt, Germany, 30.09 – 02.10.2019)
Available from: https://doi.org/10.5281/zenodo.4072692

SCHOLZ, Dieter, 2021a. *Evaluation of Box Wing Aircraft Measurements*. Excel-Table [Personal Communication]

SCHOLZ, Dieter, 2021b. *OpenVSP-Connect*. Hamburg, Germany: Hamburg University of Applied Sciences.
Available from: http://openvsp.profscholz.de
Archived at: https://perma.cc/V9G2-DVF8

RAM, Mohan T.R., 2020. *Airbus Beluga XL*. OpenVSP.
Available from: http://hangar.openvsp.org/vspfiles/431
Archived at: https://perma.cc/2TYC-UB3N

TORENBEEK, Egbert, 1982. *Synthesis of Subsonic Airplane Design*. Delft, The Netherlands: Martinus Nijhoff Publishers.
Available from: http://resolver.tudelft.nl/uuid:229f2817-9be9-49b6-959a-d653b5bac054

WHITE, Frank M, 2011. *Fluid Mechanics*. Seventh Edition. New York, USA: McGraw-Hill.
Available from: https://doi.org/10.13140/RG.2.2.21339.62244
Available from :   https://perma.cc/4TTH-MYL4

WIKIPEDIA, 2021a. *International Standard Atmosphere*.
   Available from: https://en.wikipedia.org/wiki/International_Standard_Atmosphere

WIKIPEDIA, 2021b. *OpenVSP*.
   Available from: https://en.wikipedia.org/wiki/OpenVSP

WIKIPEDIA, 2021c. *Vortex Lattice Method*.
   Available from: https://en.wikipedia.org/wiki/Vortex_lattice_method

Appendix A – Results for Hoerner's Curve When Using the VLM

Table A.1   Comparison of results for Case 1 obtained by VSPAERO, using VLM, and by theoratical formulas.

A	Alpha [°]	VSPAERO: VLM				Theoretical				Error [%]			
		e	Cdi	Cl	f(λ)	e	Cdi	Cl	f(λ)	e	Cdi	Cl	f(λ)
5	10	0.965	0.031	0.688	0.007	0.954	0.037	0.740	0.010	1.104	-14.381	-6.965	-23.834
7	10	0.951	0.028	0.770	0.007	0.937	0.033	0.824	0.010	1.509	-13.995	-6.562	-23.606
9	10	0.919	0.026	0.818	0.010	0.920	0.029	0.876	0.010	-0.205	-12.577	-6.590	2.589
10	10	0.922	0.024	0.839	0.008	0.912	0.028	0.895	0.010	1.027	-13.014	-6.255	-11.607
11	10	0.902	0.023	0.853	0.010	0.904	0.027	0.911	0.010	-0.261	-11.997	-6.320	2.735
13	10	0.864	0.021	0.887	0.012	0.889	0.024	0.936	0.010	-2.772	-12.796	-5.312	25.699
15	10	0.865	0.020	0.899	0.010	0.874	0.022	0.956	0.010	-1.075	-10.489	-5.904	8.632
17	10	0.869	0.018	0.918	0.009	0.860	0.021	0.970	0.010	1.083	-11.558	-5.443	-7.638
19	10	0.838	0.017	0.917	0.010	0.846	0.019	0.982	0.010	-0.922	-12.067	-6.655	6.032
21	10	0.800	0.016	0.926	0.012	0.832	0.018	0.992	0.010	-3.916	-9.422	-6.713	24.295
23	10	0.816	0.015	0.938	0.010	0.819	0.017	1.000	0.010	-0.356	-11.693	-6.210	1.975
25	10	0.749	0.015	0.941	0.013	0.806	0.016	1.007	0.010	-7.130	-6.108	-6.611	39.668
30	10	0.803	0.012	0.964	0.008	0.776	0.014	1.021	0.010	3.424	-13.816	-5.578	-14.805
35	10	0.773	0.011	0.975	0.008	0.749	0.013	1.030	0.010	3.229	-13.330	-5.386	-12.436
40	10	0.777	0.010	0.985	0.007	0.723	0.012	1.038	0.010	7.587	-16.186	-5.043	-25.415
45	10	0.719	0.010	0.990	0.009	0.698	0.011	1.043	0.010	2.981	-12.591	-5.119	-9.595
50	10	0.722	0.009	0.998	0.008	0.676	0.010	1.048	0.010	6.828	-15.165	-4.812	-19.707

Table A.2   Comparison of results for Case 2 obtained by VSPAERO, using VLM, and by theoratical formulas.

A	Alpha [°]	VSPAERO: VLM				Theoretical				Error [%]			
		e	Cdi	Cl	f(λ)	e	Cdi	Cl	f(λ)	e	Cdi	Cl	f(λ)
5	10	0.975	0.033	0.706	0.005	0.991	0.035	0.740	0.002	-1.588	-7.575	-4.623	174.598
7	10	0.970	0.030	0.797	0.004	0.987	0.031	0.824	0.002	-1.745	-4.793	-3.274	137.754
9	10	0.967	0.026	0.851	0.004	0.983	0.028	0.876	0.002	-1.699	-4.055	-2.882	104.669
10	10	0.966	0.025	0.871	0.004	0.982	0.026	0.895	0.002	-1.625	-3.831	-2.725	90.172
11	10	0.965	0.024	0.888	0.003	0.980	0.025	0.911	0.002	-1.555	-3.600	-2.575	78.532
13	10	0.962	0.021	0.914	0.003	0.976	0.022	0.936	0.002	-1.454	-3.235	-2.348	62.303
15	10	0.959	0.019	0.935	0.003	0.973	0.020	0.956	0.002	-1.376	-2.948	-2.167	51.229
17	10	0.957	0.017	0.943	0.003	0.969	0.018	0.970	0.002	-1.294	-4.355	-2.824	42.642
19	10	0.954	0.016	0.955	0.003	0.966	0.017	0.982	0.002	-1.218	-4.307	-2.775	36.002
21	10	0.952	0.015	0.965	0.002	0.962	0.016	0.992	0.002	-1.118	-4.230	-2.696	29.993
23	10	0.949	0.014	0.974	0.002	0.959	0.014	1.000	0.002	-1.061	-4.178	-2.645	26.071
25	10	0.946	0.013	0.982	0.002	0.955	0.014	1.007	0.002	-0.940	-3.999	-2.486	21.286
30	10	0.942	0.011	0.997	0.002	0.947	0.012	1.021	0.002	-0.545	-4.047	-2.319	10.330
35	10	0.936	0.010	1.010	0.002	0.939	0.010	1.030	0.002	-0.277	-3.752	-2.022	4.537
40	10	0.932	0.009	1.017	0.002	0.931	0.009	1.038	0.002	0.189	-4.113	-1.958	-2.712
45	10	0.929	0.008	1.024	0.002	0.923	0.008	1.043	0.002	0.714	-4.411	-1.911	-9.149
50	10	0.926	0.007	1.029	0.002	0.915	0.008	1.048	0.002	1.283	-4.909	-1.855	-14.847

Table A.3   Comparison of results for Case 3 obtained by VSPAERO, using VLM, and by theoratical formulas.

Λ	Alpha [°]	VSPAERO: VLM				Theoretical				Error [%]			
		e	Cdi	Cl	f(λ)	e	Cdi	Cl	f(λ)	e	Cdi	Cl	f(λ)
0	10	0.897	0.032	0.676	0.023	0.944	0.037	0.740	0.012	-4.936	-12.223	-8.648	92.465
0.05	10	0.973	0.032	0.701	0.006	0.958	0.036	0.740	0.009	1.527	-11.537	-5.223	-35.823
0.1	10	0.984	0.033	0.710	0.003	0.969	0.036	0.740	0.006	1.522	-9.363	-4.078	-48.691
0.15	10	0.990	0.033	0.714	0.002	0.978	0.036	0.740	0.005	1.255	-7.924	-3.451	-55.548
0.2	10	0.993	0.033	0.718	0.001	0.984	0.035	0.740	0.003	0.967	-6.844	-3.017	-58.995
0.3	10	0.996	0.033	0.720	0.001	0.990	0.035	0.740	0.002	0.626	-5.887	-2.692	-62.036
0.357	10	0.997	0.033	0.720	0.001	0.991	0.035	0.740	0.002	0.591	-5.869	-2.698	-63.539
0.4	10	0.997	0.033	0.719	0.001	0.990	0.035	0.740	0.002	0.629	-6.077	-2.789	-64.927
0.5	10	0.996	0.033	0.717	0.001	0.987	0.035	0.740	0.003	0.876	-6.919	-3.094	-67.634
0.6	10	0.994	0.033	0.714	0.001	0.982	0.035	0.740	0.004	1.252	-8.162	-3.565	-68.908
0.8	10	0.991	0.032	0.705	0.002	0.970	0.036	0.740	0.006	2.167	-11.158	-4.726	-69.906
1	10	0.986	0.031	0.696	0.003	0.954	0.037	0.740	0.010	3.297	-14.326	-5.931	-69.690

Table A.4   Comparison of results for Case 4 obtained by VSPAERO, using VLM, and by theoratical formulas.

Λ	Alpha [°]	VSPAERO: VLM				Theoretical				Error [%]			
		e	Cdi	Cl	f(λ)	e	Cdi	Cl	f(λ)	e	Cdi	Cl	f(λ)
0	10	0.831	0.026	0.822	0.020	0.894	0.029	0.895	0.012	-7.006	-9.230	-8.124	70.838
0.05	10	0.894	0.026	0.847	0.012	0.919	0.028	0.895	0.009	-2.814	-7.913	-5.391	35.925
0.1	10	0.920	0.025	0.856	0.009	0.940	0.027	0.895	0.006	-2.173	-6.451	-4.326	37.183
0.15	10	0.935	0.025	0.862	0.007	0.956	0.027	0.895	0.005	-2.205	-5.149	-3.687	51.676
0.2	10	0.945	0.025	0.866	0.006	0.968	0.026	0.895	0.003	-2.402	-4.179	-3.296	77.054
0.3	10	0.954	0.025	0.868	0.005	0.980	0.026	0.895	0.002	-2.687	-3.366	-3.019	139.093
0.357	10	0.955	0.025	0.868	0.005	0.982	0.026	0.895	0.002	-2.675	-3.407	-3.050	150.075
0.4	10	0.956	0.025	0.867	0.005	0.981	0.026	0.895	0.002	-2.588	-3.675	-3.135	139.224
0.5	10	0.953	0.025	0.864	0.005	0.975	0.026	0.895	0.003	-2.184	-4.748	-3.470	88.118
0.6	10	0.949	0.025	0.860	0.005	0.965	0.026	0.895	0.004	-1.613	-6.247	-3.968	46.485
0.8	10	0.936	0.025	0.850	0.007	0.941	0.027	0.895	0.006	-0.495	-9.431	-5.076	8.442
1	10	0.922	0.024	0.839	0.008	0.912	0.028	0.895	0.010	1.027	-13.014	-6.255	-11.607

Table A.5   Comparison of results for Case 5 obtained by VSPAERO, using VLM, and by theoratical formulas.

		VSPAERO: VLM				Theoretical				Error [%]			
Λ	Alpha [°]	e	Cdi	Cl	f(λ)	e	Cdi	Cl	f(λ)	e	Cdi	Cl	f(λ)
0	10	0.778	0.018	0.938	0.014	0.808	0.019	0.988	0.012	-3.658	-6.371	-5.024	19.748
0.05	10	0.834	0.017	0.949	0.010	0.851	0.018	0.988	0.009	-1.979	-5.819	-3.928	13.534
0.1	10	0.869	0.017	0.955	0.008	0.887	0.017	0.988	0.006	-2.025	-4.474	-3.247	18.328
0.15	10	0.892	0.016	0.960	0.006	0.916	0.017	0.988	0.005	-2.612	-3.051	-2.825	32.065
0.2	10	0.908	0.016	0.962	0.005	0.938	0.017	0.988	0.003	-3.253	-1.901	-2.579	54.316
0.3	10	0.922	0.016	0.964	0.004	0.961	0.016	0.988	0.002	-4.077	-0.737	-2.430	109.160
0.357	10	0.924	0.016	0.963	0.004	0.964	0.016	0.988	0.002	-4.180	-0.742	-2.490	121.261
0.4	10	0.923	0.016	0.962	0.004	0.963	0.016	0.988	0.002	-4.097	-1.018	-2.582	114.076
0.5	10	0.917	0.016	0.959	0.005	0.951	0.016	0.988	0.003	-3.513	-2.311	-2.906	73.651
0.6	10	0.907	0.016	0.955	0.005	0.932	0.017	0.988	0.004	-2.669	-3.932	-3.314	40.250
0.8	10	0.881	0.016	0.946	0.007	0.889	0.017	0.988	0.006	-0.878	-7.519	-4.248	7.965
1	10	0.852	0.016	0.936	0.009	0.839	0.019	0.988	0.010	1.530	-11.568	-5.239	-9.354

Table A.6   Comparison of results for Case 6 obtained by VSPAERO, using VLM, and by theoratical formulas.

		VSPAERO: VLM				Theoretical				Error [%]			
Λ	Alpha [°]	e	Cdi	Cl	f(λ)	e	Cdi	Cl	f(λ)	e	Cdi	Cl	f(λ)
0	10	0.749	0.013	0.971	0.011	0.737	0.015	1.021	0.012	1.635	-11.065	-4.914	-6.116
0.05	10	0.807	0.013	0.977	0.008	0.792	0.014	1.021	0.009	1.869	-9.961	-4.241	-8.811
0.1	10	0.845	0.012	0.983	0.006	0.840	0.013	1.021	0.006	0.601	-7.832	-3.724	-3.730
0.15	10	0.872	0.012	0.985	0.005	0.880	0.013	1.021	0.005	-0.911	-5.942	-3.478	7.634
0.2	10	0.889	0.012	0.986	0.004	0.910	0.012	1.021	0.003	-2.315	-4.510	-3.436	26.306
0.3	10	0.905	0.011	0.987	0.004	0.943	0.012	1.021	0.002	-4.047	-2.518	-3.302	73.621
0.357	10	0.906	0.011	0.986	0.003	0.947	0.012	1.021	0.002	-4.375	-2.419	-3.400	86.313
0.4	10	0.904	0.011	0.984	0.004	0.945	0.012	1.021	0.002	-4.313	-2.895	-3.611	81.745
0.5	10	0.893	0.011	0.982	0.004	0.928	0.012	1.021	0.003	-3.684	-3.825	-3.750	52.861
0.6	10	0.878	0.012	0.979	0.005	0.901	0.012	1.021	0.004	-2.588	-5.671	-4.125	26.888
0.8	10	0.841	0.012	0.972	0.006	0.842	0.013	1.021	0.006	-0.094	-9.286	-4.803	0.596
1	10	0.803	0.012	0.964	0.008	0.776	0.014	1.021	0.010	3.455	-13.816	-5.580	-14.934

Table A.7   Comparison of results for Case 7 obtained by VSPAERO, using VLM, and by theoratical formulas.

		VSPAERO: VLM				Theoretical				Error [%]			
Λ	Alpha [°]	e	Cdi	Cl	f(λ)	e	Cdi	Cl	f(λ)	e	Cdi	Cl	f(λ)
0	10	0.733	0.011	1.006	0.009	0.678	0.013	1.038	0.012	8.129	-13.109	-3.086	-23.311
0.05	10	0.791	0.010	1.013	0.007	0.740	0.012	1.038	0.009	6.826	-10.834	-2.415	-24.612
0.1	10	0.832	0.010	1.017	0.005	0.797	0.011	1.038	0.006	4.322	-7.975	-2.031	-20.442
0.15	10	0.860	0.010	1.019	0.004	0.846	0.010	1.038	0.005	1.728	-5.262	-1.808	-11.002
0.2	10	0.879	0.009	1.020	0.003	0.883	0.010	1.038	0.003	-0.498	-2.889	-1.686	4.290
0.3	10	0.895	0.009	1.021	0.003	0.925	0.009	1.038	0.002	-3.197	-0.144	-1.656	44.067
0.357	10	0.896	0.009	1.020	0.003	0.931	0.009	1.038	0.002	-3.707	0.340	-1.726	55.438
0.4	10	0.894	0.009	1.019	0.003	0.928	0.009	1.038	0.002	-3.692	0.152	-1.803	53.091
0.5	10	0.881	0.009	1.016	0.003	0.906	0.009	1.038	0.003	-2.704	-1.377	-2.058	29.507
0.6	10	0.863	0.009	1.013	0.004	0.872	0.010	1.038	0.004	-1.062	-3.685	-2.367	8.417
0.8	10	0.821	0.010	1.006	0.005	0.800	0.011	1.038	0.006	2.658	-8.442	-3.054	-12.933
1	10	0.779	0.010	0.999	0.007	0.723	0.012	1.038	0.010	7.754	-14.079	-3.762	-25.936

Table A.8   Comparison of results for Case 8 obtained by VSPAERO, using VLM, and by theoratical formulas.

		VSPAERO: VLM				Theoretical				Error [%]			
Λ	Alpha [°]	e	Cdi	Cl	f(λ)	e	Cdi	Cl	f(λ)	e	Cdi	Cl	f(λ)
0	10	0.751	0.037	0.806	0.044	0.918	0.033	0.839	0.012	-18.186	12.854	-3.906	271.295
0.05	10	0.928	0.029	0.792	0.010	0.938	0.032	0.839	0.009	-1.134	-9.780	-5.560	18.589
0.1	10	0.949	0.029	0.803	0.007	0.955	0.031	0.839	0.006	-0.627	-7.934	-4.354	13.862
0.15	10	0.960	0.029	0.808	0.006	0.967	0.031	0.839	0.005	-0.716	-6.544	-3.671	21.783
0.2	10	0.967	0.029	0.812	0.005	0.976	0.031	0.839	0.003	-0.918	-5.484	-3.230	38.366
0.3	10	0.973	0.029	0.815	0.004	0.985	0.030	0.839	0.002	-1.180	-4.561	-2.884	79.822
0.357	10	0.975	0.029	0.815	0.003	0.986	0.030	0.839	0.002	-1.171	-4.614	-2.909	85.863
0.4	10	0.975	0.029	0.814	0.003	0.986	0.030	0.839	0.002	-1.095	-4.835	-2.992	76.960
0.5	10	0.974	0.029	0.811	0.004	0.981	0.030	0.839	0.003	-0.740	-5.851	-3.322	39.002
0.6	10	0.971	0.028	0.807	0.004	0.973	0.031	0.839	0.004	-0.257	-7.195	-3.788	9.646
0.8	10	0.963	0.028	0.797	0.005	0.955	0.031	0.839	0.006	0.828	-10.429	-4.965	-18.313
1	10	0.953	0.028	0.787	0.007	0.933	0.032	0.839	0.010	2.183	-13.896	-6.199	-31.809

Table A.9   Comparison of results for Case 9 obtained by VSPAERO, using VLM, and by theoratical formulas.

Λ	Alpha [°]	VSPAERO: VLM				Theoretical				Error [%]			
		e	Cdi	Cl	f(λ)	e	Cdi	Cl	f(λ)	e	Cdi	Cl	f(λ)
0	10	0.881	0.031	0.722	0.022	0.933	0.035	0.787	0.012	-5.598	-11.072	-8.369	88.980
0.05	10	0.950	0.031	0.745	0.009	0.950	0.035	0.787	0.009	0.016	-10.581	-5.434	-0.315
0.1	10	0.966	0.031	0.754	0.006	0.963	0.034	0.787	0.006	0.286	-8.544	-4.229	-7.766
0.15	10	0.974	0.031	0.759	0.004	0.973	0.034	0.787	0.005	0.097	-7.114	-3.577	-3.653
0.2	10	0.979	0.032	0.763	0.004	0.981	0.034	0.787	0.003	-0.136	-6.036	-3.133	7.024
0.3	10	0.984	0.032	0.765	0.003	0.988	0.033	0.787	0.002	-0.429	-5.116	-2.805	35.925
0.357	10	0.985	0.032	0.765	0.003	0.989	0.033	0.787	0.002	-0.443	-5.207	-2.859	40.173
0.4	10	0.985	0.031	0.764	0.003	0.988	0.033	0.787	0.002	-0.389	-5.432	-2.944	33.819
0.5	10	0.984	0.031	0.761	0.003	0.985	0.033	0.787	0.003	-0.096	-6.426	-3.312	6.285
0.6	10	0.982	0.031	0.757	0.003	0.979	0.034	0.787	0.004	0.320	-7.928	-3.894	-14.856
0.8	10	0.976	0.030	0.746	0.004	0.964	0.034	0.787	0.006	1.270	-11.336	-5.242	-34.661
1	10	0.970	0.029	0.732	0.005	0.946	0.035	0.787	0.010	2.534	-15.805	-7.080	-45.383
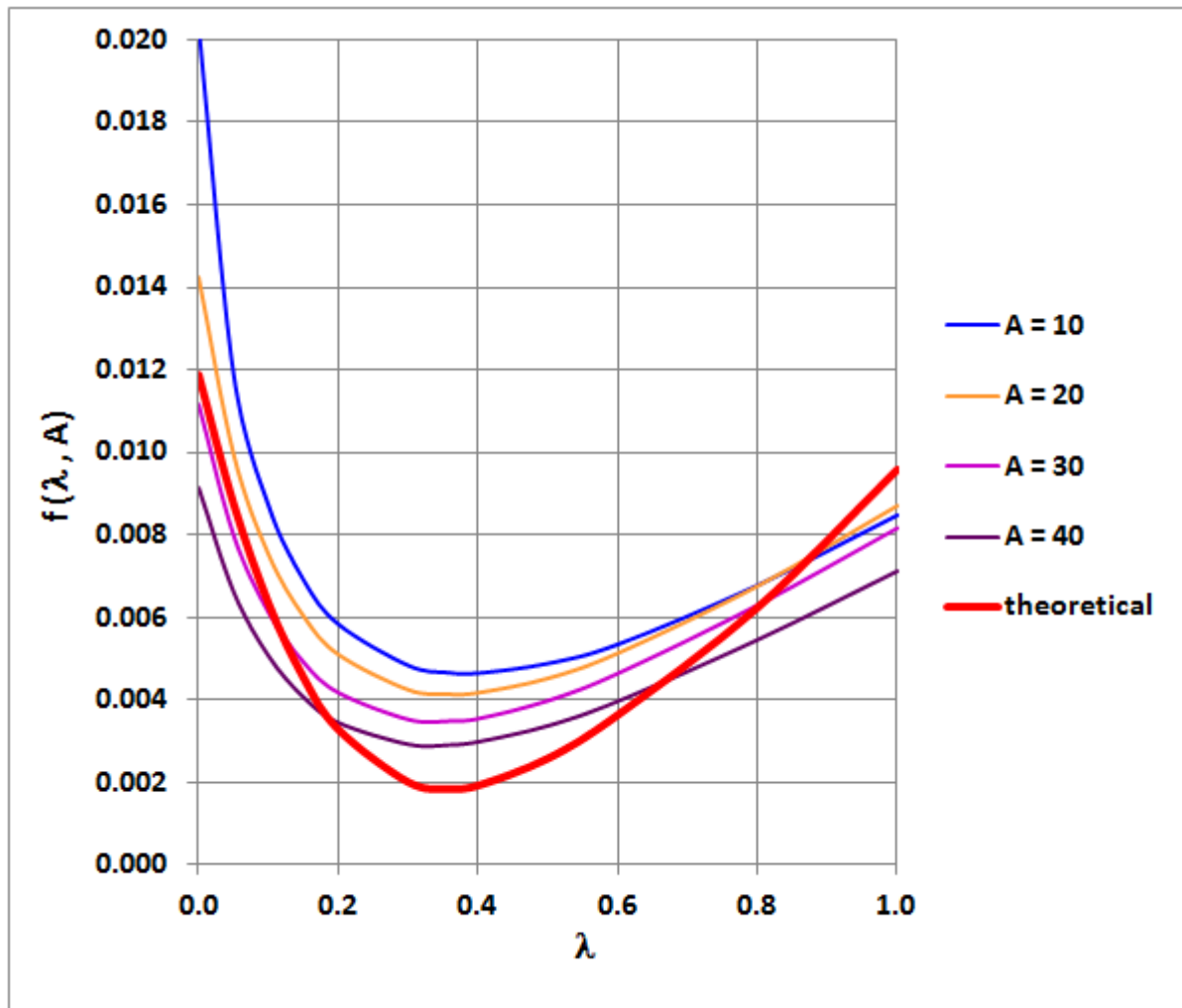
Figure A.1   f(λ,A) for aspect ratios, A from 10 to 40 from VLM compared with Hoerner's theoretical curve.
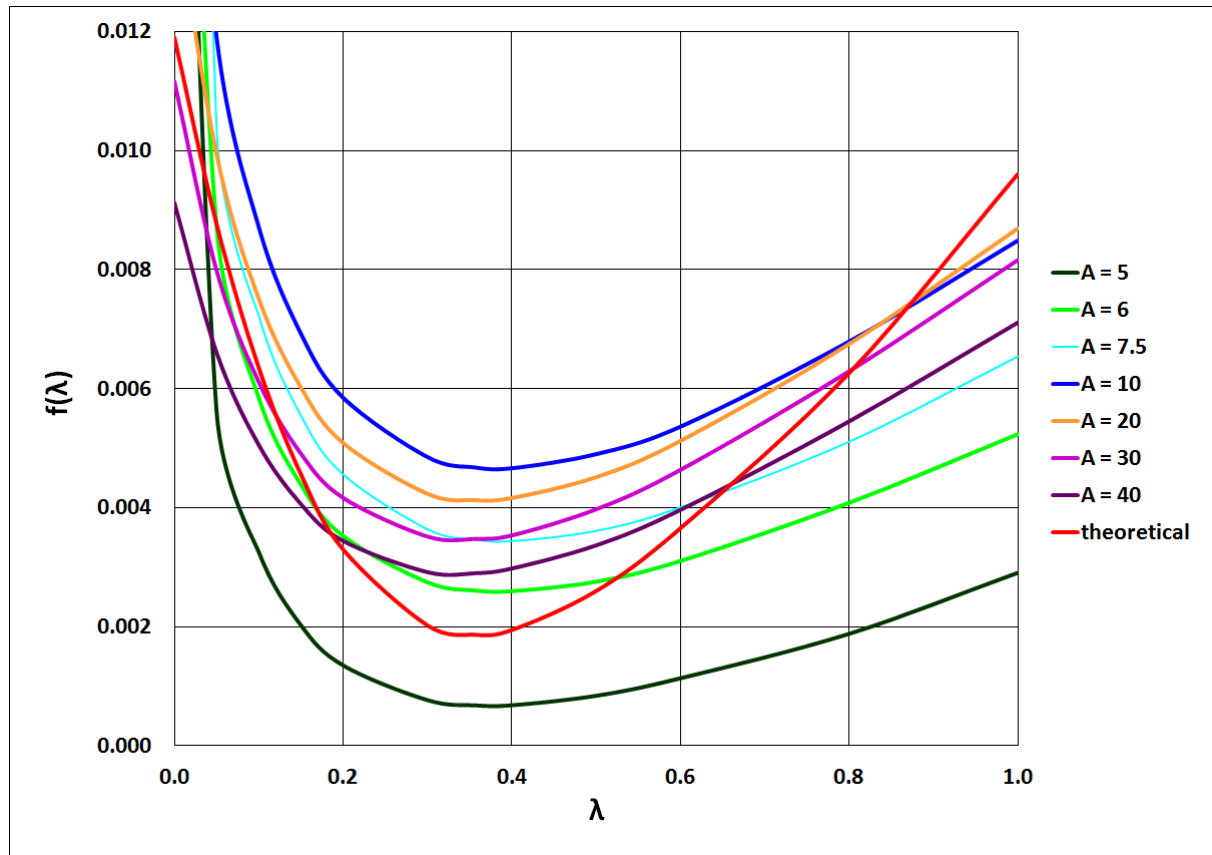
Figure A.2   f(λ,A) for aspect ratios, A from 5 to 40 from VLM compared with Hoerner's theoretical curve. Overall a less unified picture.

Appendix B – Results for Hoerner's Curve When Using the Panel Method

Table B.1 Comparison of results for Case 1 obtained by VSPAERO, using panel method, and by theoratical formulas.

A	Alpha [°]	VSPAERO: Panel Method				Theoretical				Error [%]			
		e	Cdi	Cl	f(λ)	e	Cdi	Cl	f(λ)	e	Cdi	Cl	f(λ)
5	10	0.859	0.033	0.665	0.033	0.954	0.037	0.740	0.010	-9.956	-9.261	-10.141	241.403
7	10	0.829	0.030	0.742	0.029	0.937	0.033	0.824	0.010	-11.495	-8.378	-9.943	206.261
9	10	0.812	0.027	0.793	0.026	0.920	0.029	0.876	0.010	-11.770	-7.081	-9.455	167.743
10	10	0.809	0.026	0.818	0.024	0.912	0.028	0.895	0.010	-11.315	-5.858	-8.635	145.661
11	10	0.803	0.025	0.832	0.022	0.904	0.027	0.911	0.010	-11.168	-6.123	-8.678	131.630
13	10	0.792	0.023	0.864	0.020	0.889	0.024	0.936	0.010	-10.869	-4.431	-7.715	109.901
15	10	0.785	0.021	0.886	0.018	0.874	0.022	0.956	0.010	-10.247	-4.218	-7.280	90.706
17	10	0.776	0.020	0.905	0.017	0.860	0.021	0.970	0.010	-9.733	-3.709	-6.763	76.855
19	10	0.760	0.019	0.919	0.017	0.846	0.019	0.982	0.010	-10.190	-2.442	-6.427	73.548
21	10	0.749	0.017	0.929	0.016	0.832	0.018	0.992	0.010	-10.048	-2.506	-6.347	66.581
23	10	0.742	0.016	0.940	0.015	0.819	0.017	1.000	0.010	-9.384	-2.584	-6.055	57.255
25	10	0.749	0.015	0.953	0.013	0.806	0.016	1.007	0.010	-7.086	-3.736	-5.421	39.400
30	10	0.723	0.014	0.969	0.013	0.776	0.014	1.021	0.010	-6.933	-3.140	-5.041	33.316
35	10	0.701	0.012	0.981	0.012	0.749	0.013	1.030	0.010	-6.330	-3.175	-4.757	26.872
40	10	0.695	0.011	0.992	0.011	0.723	0.012	1.038	0.010	-3.759	-4.972	-4.380	14.079
45	10	0.668	0.011	1.000	0.011	0.698	0.011	1.043	0.010	-4.272	-4.158	-4.202	14.794
50	10	0.675	0.010	1.008	0.010	0.676	0.010	1.048	0.010	-0.053	-7.531	-3.859	0.162

Table B.2 Comparison of results for Case 2 obtained by VSPAERO, using panel method, and by theoratical formulas.

A	Alpha [°]	VSPAERO: Panel Method				Theoretical				Error [%]			
		e	Cdi	Cl	f(λ)	e	Cdi	Cl	f(λ)	e	Cdi	Cl	f(λ)
5	10	0.827	0.035	0.674	0.042	0.991	0.035	0.740	0.002	-16.579	-0.383	-8.837	2149.961
7	10	0.836	0.032	0.767	0.028	0.987	0.031	0.824	0.002	-15.298	2.434	-6.855	1400.759
9	10	0.841	0.029	0.824	0.021	0.983	0.028	0.876	0.002	-14.496	3.593	-5.888	1026.437
10	10	0.843	0.027	0.845	0.019	0.982	0.026	0.895	0.002	-14.090	3.715	-5.612	895.355
11	10	0.842	0.026	0.864	0.017	0.980	0.025	0.911	0.002	-14.094	4.640	-5.183	815.711
13	10	0.842	0.023	0.893	0.014	0.976	0.022	0.936	0.002	-13.751	5.495	-4.602	673.204
15	10	0.841	0.021	0.916	0.013	0.973	0.020	0.956	0.002	-13.501	6.190	-4.151	573.236
17	10	0.841	0.019	0.936	0.011	0.969	0.018	0.970	0.002	-13.259	7.133	-3.596	497.151
19	10	0.841	0.018	0.952	0.010	0.966	0.017	0.982	0.002	-12.935	7.759	-3.141	433.894
21	10	0.837	0.017	0.962	0.009	0.962	0.016	0.992	0.002	-13.043	8.152	-3.025	397.773
23	10	0.836	0.016	0.971	0.009	0.959	0.014	1.000	0.002	-12.853	8.077	-2.952	358.387
25	10	0.832	0.015	0.980	0.008	0.955	0.014	1.007	0.002	-12.887	8.722	-2.695	331.918
30	10	0.830	0.013	0.993	0.007	0.947	0.012	1.021	0.002	-12.366	8.033	-2.708	266.191
35	10	0.826	0.011	1.003	0.006	0.939	0.010	1.030	0.002	-12.053	7.817	-2.627	223.555
40	10	0.824	0.010	1.009	0.005	0.931	0.009	1.038	0.002	-11.420	6.855	-2.720	185.611
45	10	0.821	0.009	1.017	0.005	0.923	0.008	1.043	0.002	-11.040	6.849	-2.533	160.196
50	10	0.818	0.008	1.022	0.004	0.915	0.008	1.048	0.002	-10.528	6.340	-2.468	137.879

Table B.3 Comparison of results for Case 3 obtained by VSPAERO, using panel method, and by theoratical formulas.

Λ	Alpha [°]	VSPAERO: Panel Method				Theoretical				Error [%]			
		e	Cdi	Cl	f(λ)	e	Cdi	Cl	f(λ)	e	Cdi	Cl	f(λ)
0.05	10	0.814	0.035	0.669	0.046	0.958	0.036	0.740	0.009	-15.078	-3.813	-9.617	422.832
0.1	10	0.826	0.036	0.679	0.042	0.969	0.036	0.740	0.006	-14.740	-1.159	-8.198	561.420
0.15	10	0.835	0.035	0.680	0.039	0.978	0.036	0.740	0.005	-14.579	-1.107	-8.095	765.107
0.2	10	0.840	0.035	0.682	0.038	0.984	0.035	0.740	0.003	-14.665	-0.492	-7.856	1058.755
0.3	10	0.840	0.035	0.676	0.038	0.990	0.035	0.740	0.002	-15.111	-1.711	-8.655	1775.522
0.357	10	0.842	0.035	0.677	0.037	0.991	0.035	0.740	0.002	-14.993	-1.548	-8.517	1908.234
0.4	10	0.844	0.035	0.678	0.037	0.990	0.035	0.740	0.002	-14.799	-1.303	-8.302	1803.065
0.5	10	0.845	0.034	0.677	0.037	0.987	0.035	0.740	0.003	-14.371	-2.301	-8.540	1307.784
0.6	10	0.848	0.034	0.676	0.036	0.982	0.035	0.740	0.004	-13.672	-3.427	-8.695	882.410
0.8	10	0.850	0.034	0.670	0.035	0.970	0.036	0.740	0.006	-12.329	-6.539	-9.480	463.404
1	10	0.849	0.033	0.665	0.036	0.954	0.037	0.740	0.010	-11.023	-9.261	-10.141	270.476

Table B.4 Comparison of results for Case 4 obtained by VSPAERO, using panel method, and by theoratical formulas.

Λ	Alpha [°]	VSPAERO: Panel Method				Theoretical				Error [%]			
		e	Cdi	Cl	f(λ)	e	Cdi	Cl	f(λ)	e	Cdi	Cl	f(λ)
0.05	10	0.772	0.028	0.825	0.030	0.919	0.028	0.895	0.009	-16.012	1.101	-7.847	236.536
0.1	10	0.796	0.028	0.833	0.026	0.940	0.027	0.895	0.006	-15.377	2.399	-6.905	304.143
0.15	10	0.810	0.028	0.842	0.024	0.956	0.027	0.895	0.005	-15.336	4.453	-5.970	415.098
0.2	10	0.819	0.028	0.845	0.022	0.968	0.026	0.895	0.003	-15.381	5.464	-5.539	569.010
0.3	10	0.830	0.028	0.847	0.020	0.980	0.026	0.895	0.002	-15.311	5.744	-5.364	910.660
0.357	10	0.833	0.027	0.847	0.020	0.982	0.026	0.895	0.002	-15.168	5.563	-5.361	976.176
0.4	10	0.834	0.027	0.847	0.020	0.981	0.026	0.895	0.002	-15.013	5.250	-5.419	925.702
0.5	10	0.833	0.027	0.844	0.020	0.975	0.026	0.895	0.003	-14.495	3.929	-5.730	668.972
0.6	10	0.831	0.027	0.839	0.020	0.965	0.026	0.895	0.004	-13.908	2.114	-6.230	458.152
0.8	10	0.821	0.027	0.828	0.022	0.941	0.027	0.895	0.006	-12.775	-1.902	-7.493	248.647
1	10	0.809	0.026	0.818	0.024	0.912	0.028	0.895	0.010	-11.315	-5.858	-8.635	145.661

Table B.5 Comparison of results for Case 5 obtained by VSPAERO, using panel method, and by theoratical formulas.

Λ	Alpha [°]	VSPAERO: Panel Method				Theoretical				Error [%]			
		e	Cdi	Cl	f(λ)	e	Cdi	Cl	f(λ)	e	Cdi	Cl	f(λ)
0.05	10	0.730	0.019	0.937	0.018	0.851	0.018	0.988	0.009	-14.188	4.981	-5.094	110.839
0.1	10	0.762	0.019	0.945	0.016	0.887	0.017	0.988	0.006	-14.138	6.559	-4.349	146.027
0.15	10	0.784	0.018	0.949	0.014	0.916	0.017	0.988	0.005	-14.410	7.990	-3.866	201.324
0.2	10	0.798	0.018	0.952	0.013	0.938	0.017	0.988	0.003	-14.887	9.220	-3.584	282.507
0.3	10	0.814	0.018	0.954	0.011	0.961	0.016	0.988	0.002	-15.348	10.224	-3.415	465.718
0.357	10	0.817	0.018	0.953	0.011	0.964	0.016	0.988	0.002	-15.282	10.004	-3.471	501.444
0.4	10	0.817	0.018	0.952	0.011	0.963	0.016	0.988	0.002	-15.099	9.463	-3.588	474.872
0.5	10	0.814	0.018	0.949	0.011	0.951	0.016	0.988	0.003	-14.395	7.856	-3.922	340.180
0.6	10	0.806	0.018	0.945	0.012	0.932	0.017	0.988	0.004	-13.545	5.915	-4.294	229.980
0.8	10	0.785	0.018	0.934	0.014	0.889	0.017	0.988	0.006	-11.694	1.414	-5.369	119.025
1	10	0.758	0.018	0.925	0.016	0.839	0.019	0.988	0.010	-9.609	-3.028	-6.374	66.001

Table B.6 Comparison of results for Case 6 obtained by VSPAERO, using panel method, and by theoratical formulas.

Λ	Alpha [°]	VSPAERO: Panel Method				Theoretical				Error [%]			
		e	Cdi	Cl	f(λ)	e	Cdi	Cl	f(λ)	e	Cdi	Cl	f(λ)
0.05	10	0.710	0.014	0.983	0.014	0.792	0.014	1.021	0.009	-10.364	3.578	-3.660	55.529
0.1	10	0.745	0.014	0.988	0.011	0.840	0.013	1.021	0.006	-11.282	5.694	-3.162	79.423
0.15	10	0.770	0.014	0.992	0.010	0.880	0.013	1.021	0.005	-12.499	7.904	-2.837	118.635
0.2	10	0.786	0.013	0.994	0.009	0.910	0.012	1.021	0.003	-13.583	9.732	-2.630	174.489
0.3	10	0.803	0.013	0.995	0.008	0.943	0.012	1.021	0.002	-14.853	11.469	-2.560	304.514
0.357	10	0.805	0.013	0.994	0.008	0.947	0.012	1.021	0.002	-15.024	11.546	-2.625	333.528
0.4	10	0.804	0.013	0.993	0.008	0.945	0.012	1.021	0.002	-14.883	11.124	-2.728	317.087
0.5	10	0.797	0.013	0.990	0.008	0.928	0.012	1.021	0.003	-14.094	9.519	-2.993	226.747
0.6	10	0.785	0.013	0.986	0.009	0.901	0.012	1.021	0.004	-12.906	7.210	-3.365	149.956
0.8	10	0.756	0.013	0.977	0.011	0.842	0.013	1.021	0.006	-10.240	2.216	-4.232	72.165
1	10	0.723	0.014	0.969	0.013	0.776	0.014	1.021	0.010	-6.824	-3.210	-5.051	32.751

Table B.7 Comparison of results for Case 7 obtained by VSPAERO, using panel method, and by theoratical formulas.

Λ	Alpha [°]	VSPAERO: Panel Method				Theoretical				Error [%]			
		e	Cdi	Cl	f(λ)	e	Cdi	Cl	f(λ)	e	Cdi	Cl	f(λ)
0.05	10	0.697	0.012	1.006	0.011	0.740	0.012	1.038	0.009	-5.854	-0.120	-3.013	23.951
0.1	10	0.734	0.011	1.011	0.009	0.797	0.011	1.038	0.006	-7.954	3.097	-2.593	42.640
0.15	10	0.760	0.011	1.013	0.008	0.846	0.010	1.038	0.005	-10.150	6.087	-2.350	73.186
0.2	10	0.777	0.011	1.015	0.007	0.883	0.010	1.038	0.003	-12.007	8.761	-2.189	117.022
0.3	10	0.794	0.010	1.016	0.006	0.925	0.009	1.038	0.002	-14.173	11.622	-2.113	220.332
0.357	10	0.796	0.010	1.015	0.006	0.931	0.009	1.038	0.002	-14.501	11.960	-2.170	244.211
0.4	10	0.794	0.010	1.014	0.006	0.928	0.009	1.038	0.002	-14.401	11.629	-2.238	233.015
0.5	10	0.784	0.010	1.012	0.007	0.906	0.009	1.038	0.003	-13.411	9.827	-2.466	164.413
0.6	10	0.769	0.011	1.008	0.008	0.872	0.010	1.038	0.004	-11.836	7.005	-2.881	105.255
0.8	10	0.733	0.011	1.000	0.009	0.800	0.011	1.038	0.006	-8.340	1.358	-3.593	45.440
1	10	0.696	0.011	0.993	0.011	0.723	0.012	1.038	0.010	-3.653	-5.056	-4.354	13.665

Table B.8 Comparison of results for Case 8 obtained by VSPAERO, using panel method, and by theoratical formulas.

Λ	Alpha [°]	VSPAERO: Panel Method				Theoretical				Error [%]			
		e	Cdi	Cl	f(λ)	e	Cdi	Cl	f(λ)	e	Cdi	Cl	f(λ)
0.05	10	0.791	0.031	0.765	0.035	0.938	0.032	0.839	0.009	-15.704	-1.427	-8.839	301.972
0.1	10	0.810	0.032	0.776	0.031	0.955	0.031	0.839	0.006	-15.100	0.691	-7.536	390.988
0.15	10	0.821	0.032	0.782	0.029	0.967	0.031	0.839	0.005	-15.048	2.290	-6.774	535.306
0.2	10	0.829	0.032	0.785	0.027	0.976	0.031	0.839	0.003	-15.029	3.138	-6.391	732.348
0.3	10	0.839	0.031	0.786	0.026	0.985	0.030	0.839	0.002	-14.825	2.988	-6.347	1163.232
0.357	10	0.842	0.031	0.786	0.025	0.986	0.030	0.839	0.002	-14.631	2.713	-6.360	1241.846
0.4	10	0.843	0.031	0.785	0.025	0.986	0.030	0.839	0.002	-14.506	2.257	-6.498	1179.795
0.5	10	0.843	0.031	0.782	0.025	0.981	0.030	0.839	0.003	-14.090	0.977	-6.860	857.457
0.6	10	0.842	0.030	0.775	0.025	0.973	0.031	0.839	0.004	-13.476	-1.299	-7.594	583.757
0.8	10	0.837	0.030	0.769	0.026	0.955	0.031	0.839	0.006	-12.406	-4.099	-8.352	315.886
1	10	0.829	0.029	0.759	0.028	0.933	0.032	0.839	0.010	-11.147	-8.027	-9.596	186.793

Table B.9   Comparison of results for Case 9 obtained by VSPAERO, using panel method, and by theoratical formulas.

Λ	Alpha [°]	VSPAERO: Panel Method				Theoretical				Error [%]			
		e	Cdi	Cl	f(λ)	e	Cdi	Cl	f(λ)	e	Cdi	Cl	f(λ)
0.05	10	0.801	0.034	0.713	0.041	0.950	0.035	0.787	0.009	-15.662	-2.697	-9.414	371.626
0.1	10	0.815	0.034	0.723	0.038	0.963	0.034	0.787	0.006	-15.362	-0.491	-8.232	494.203
0.15	10	0.825	0.034	0.726	0.035	0.973	0.034	0.787	0.005	-15.213	0.373	-7.753	673.280
0.2	10	0.832	0.034	0.730	0.034	0.981	0.034	0.787	0.003	-15.191	1.327	-7.305	922.637
0.3	10	0.842	0.034	0.731	0.031	0.988	0.033	0.787	0.002	-14.785	1.071	-7.197	1445.025
0.357	10	0.845	0.034	0.732	0.031	0.989	0.033	0.787	0.002	-14.551	1.257	-6.989	1538.134
0.4	10	0.845	0.034	0.731	0.031	0.988	0.033	0.787	0.002	-14.522	0.789	-7.185	1472.429
0.5	10	0.845	0.033	0.728	0.031	0.985	0.033	0.787	0.003	-14.176	-0.469	-7.582	1075.307
0.6	10	0.844	0.033	0.723	0.031	0.979	0.034	0.787	0.004	-13.766	-2.305	-8.209	743.916
0.8	10	0.839	0.032	0.714	0.032	0.964	0.034	0.787	0.006	-12.975	-5.447	-9.282	411.927
1	10	0.829	0.032	0.702	0.034	0.946	0.035	0.787	0.010	-12.339	-9.423	-10.892	258.441
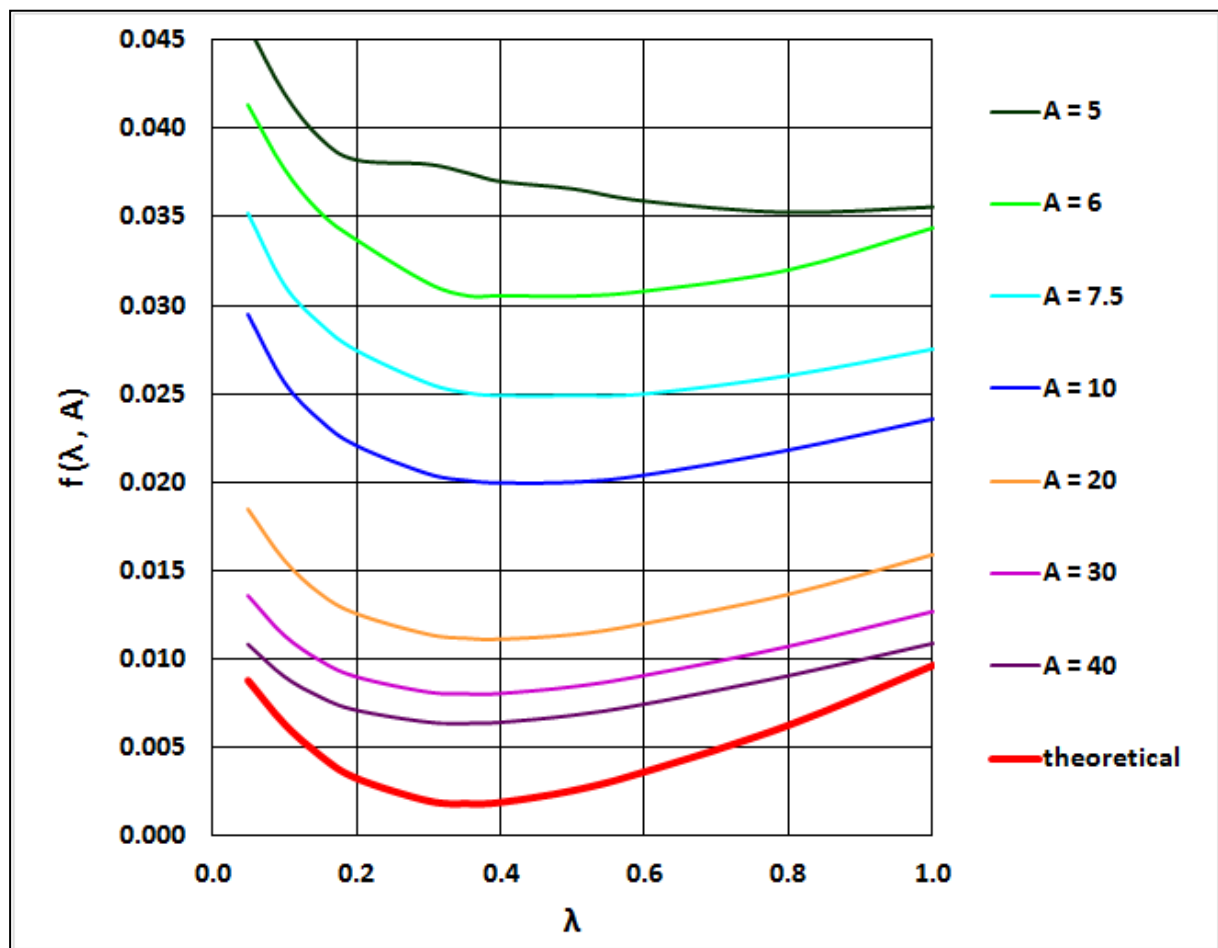
Figure B.1   f(λ,A) for aspect ratios, A from 5 to 40 from panel method compared with Hoerner's theoretical curve.
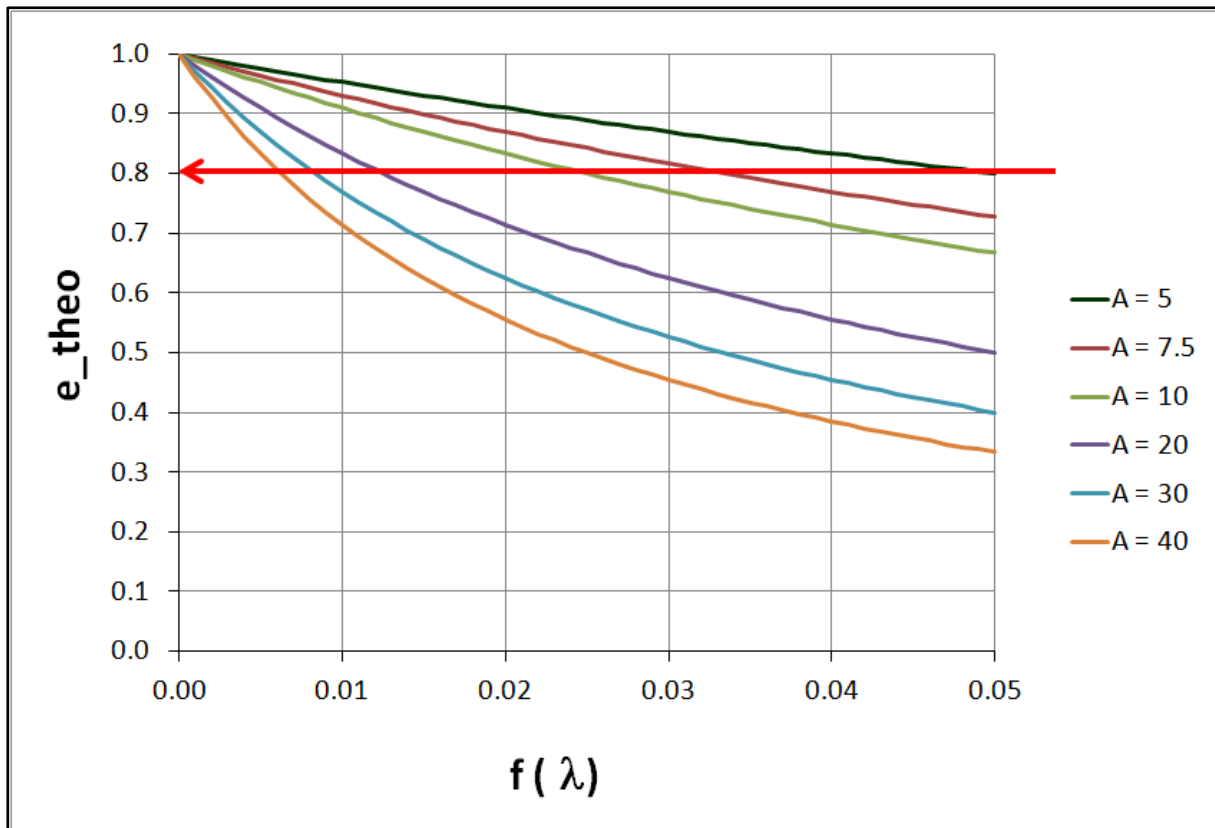
Figure B.2   Theoretical span efficiency, e_{theo} for aspect ratios, A from 5 to 40 and parameter and $f(\lambda)$. e_{theo} is calculated with basic equation (6.3). For e.g. e_{theo} = 0.8, a large aspect ratio, needs only a small $f(\lambda)$.